Coherent control of nonlinear optical processes in individual nanoparticles

By:
Nicolò Accanto

Supervisor:
Niek F. van Hulst

UNIVERSITAT POLITÈCNICA DE CATALUNYA

ICFO – The Insitute of Photonic Sciences

June 2016

Contents

Introduction **1**
Ultrafast nanophotonics 1
Nonlinear coherent control at the nanoscale 2
Coherent and incoherent nanoparticles 3
Thesis outline 4

1 Experimental setup and background concepts **7**
1.1 Laser and pulse shaper 8
1.2 Confocal microscope 10
1.3 Ultrafast pulses propagating through dispersive media 11
1.3.1 Phase distortions 12
1.3.2 Spatio-temporal coupling 15
1.4 Pulse compression 17
1.4.1 Second harmonic generation from broadband pulses . . 17
1.4.2 MIIPS 19

2 Pulse control at the nanoscale **23**
2.1 Second harmonic nanoparticles 24
2.2 Pulse compression on single NPs 27
2.3 Independence on the nanoparticle studied 31
2.4 Control of the SH emission from NPs 34
2.5 Spatial considerations 35
2.6 Conclusions 37

3 Resonant effects in plasmonic nanoantennas **41**
3.1 Plasmonic nanoantennas 42
3.2 The nanoantennas studied 44
3.3 The measurement of the plasmon resonance 46
3.3.1 Visualizing the resonant response 47
3.3.2 The fitting procedure 49

3.4 Nanoantennas for multicolor second harmonic imaging 54
3.4.1 Intensity contrast 55
3.4.2 Spectral contrast 57
3.4.3 Demonstration of multicolor imaging 58
3.5 Conclusions 61

4 Closed loop control of single emitters **63**
4.1 Control of single emitters, a great experimental challenge 64
4.2 Principles of two photon coherent control 67
4.3 The quantum dots studied 69
4.4 The optimization algorithm 70
4.5 Two photon absorption maximization in single quantum dots . 73
4.6 Characterization of the optimal solution 76
4.7 Conclusions 78

5 Controlling the two-photon absorption in nanoantennas **81**
5.1 The nanoantennas studied 83
5.2 The role of the intermediate state 84
5.2.1 Dependence of the TPA on the pulse duration 85
5.2.2 The very short pulse limit 87
5.2.3 Coherent control of a single nanoantenna 88
5.3 Closed loop coherent control of nanoantenna pairs 90
5.3.1 Experimental details 91
5.3.2 Control of the relative emission from two nanoantennas . 93
5.3.3 Coherent two photon microscopy 95
5.3.4 Interpretation of coherent control 98
5.4 Conclusions 101

Conclusion **103**

Publications **105**

Acknowledgments **107**

Bibliography **110**

Introduction

Light-matter interactions occur everywhere around us at any time. Photons emitted by the sun are continuously reaching our planet making objects visible, providing energy to the surface of the earth, stimulating photosynthesis in plants and bacteria, dictating biological rhythms in animals. The study of light-matter interactions directly leads to a better understanding of the world surrounding us. At the same time, we can also learn how to exploit these phenomena in our favor. Artificial light sources, solar cells, optical fibers are all widely used technologies that make direct use of light-matter interactions.

Ultrafast nanophotonics

Nanophotonics concerns itself with the manipulation of light-matter interactions on the nanometer scale. Boosted by the tremendous development of nanotechnology and nanofabrication, nanophotonics is today a thriving research field. Solid state nano-emitters made of semiconductors, metallic nanoparticles that function as antennas for light, nano-apertures that squeeze light into nanometric volumes, waveguides that propagate light between two different points are all commonly used elements in nanophotonics. Applications of this field include: optical communications and optical integrated circuits, high-quality biological sensors and biological imaging, super-resolution optical microscopy, photovoltaics and photodetectors, just to name a few.

The study of the fundamental interactions between light and nanometer-sized objects is an important stage for the design of better structures and the development of new applications. In a simple picture, when photons interact with a nanoparticle, they induce a time dependent polarization, or a charge separation in the material, after which the system quickly relaxes towards the equilibrium. The time resolution is therefore relevant for a correct description of the interaction. Moreover, the evolution of the system usually depends on

the specific properties of the nanoparticle considered, such as size, shape and material. A bottom-up experimental approach is thus necessary for a complete understanding of these phenomena. Only by observing nanoparticles one at a time with high temporal resolution can one access the fundamentals of light-matter interactions. This thesis is precisely about unveiling and controlling ultrafast processes occurring in individual nanoparticles.

In recent years, several research groups have developed different experimental techniques to observe light-matter interactions with high spatial and temporal resolution [1–14], with our group being very active in the the study of the ultrafast and coherent dynamics of individual molecules and molecular systems [15–19]. The practical realization of these experiments however, is very demanding as delivering the desired ultrashort laser pulses to nanometric volumes, which is an essential experimental requirement, is a complicated task. The first goal of the thesis is thus to provide a reliable solution to such a problem and develop a robust and easy to operate experimental scheme capable of addressing ultrafast and ultrasmall processes simultaneously. This scheme, which combines ultrashort phase-controlled laser pulses with high resolution microscopes, is at the basis of all the experiments described here.

Nonlinear coherent control at the nanoscale

The objective of this work is not only to observe but also to manipulate light-matter interactions on the nanoscale. There are two possible approaches to this problem: one can either act on the side of the excitation source, changing the properties of the laser field (like pulse duration, phase, polarization, intensity), or on the side of the investigated object, fabricating different structures (in size, shape, material) that interact differently with the electromagnetic field. Researchers have mainly focused on the latter, and a great variety of nanostructures are today easily available for many different applications. However, to fully exploit the potential of nanophotonics, we need to act on both sides and master interactions of light with nanoparticles by controlling the laser field. This, for instance, could allow researchers to switch light from one side to another of an asymmetric nanostructure, to address different nanoparticles at different times within the same sample, to combine super-resolution optical microscopy with femtosecond temporal resolution.

The ability of influencing the outcome of certain light-matter interactions by using precisely tailored laser fields is often referred to as coherent control [20–27]. A common implementation of such a concept, is based on the use of ultrashort laser pulses, whose spectral phase and amplitude are manipulated, to induce the desired effect in the system under study. Among the possible optical observables, nonlinear processes are intrinsically related to the phase of the excitation field and therefore are expected to be highly affected by coherent control [24, 26].

Coherent control concepts have been so far mainly applied to ensembles of systems (for instance atoms, molecules or quantum dots). Here, the main goal is to extend them to the manipulation of light-matter interactions at the nanoscale, which is a largely unexplored research area. The study of nonlinear optical processes in individual nanoparticles under ultrafast coherent control is at the heart of this thesis.

Coherent and incoherent nanoparticles

In a simple description, the nanoparticles (NPs) investigated throughout the thesis can be divided into two categories: coherent and incoherent NPs. Coherent NPs present an intrinsic response, i.e. an amplitude and/or phase response, which can be resolved by the laser field. They are in general NPs resonant with the excitation field, with a sufficiently narrow (narrower than the laser spectrum) resonance. Resonant plasmonic nanoantennas constitute the main example of coherent NPs studied in the thesis. Incoherent NPs can be either non-resonant NPs, or NPs characterized by a very broad (much broader than the laser spectrum) resonance. Dielectric nonlinear NPs and semiconductor quantum dots (QDs) with broad absorptions are the incoherent NPs addressed here.

Even if coherent NPs are the most interesting, incoherent NPs are of crucial importance as well. Because in this case the nonlinear interaction with the laser field mainly depends on the laser itself, these NPs provide a safe platform to test the predictions of coherent control as well as our abilities to extend it to the nanoscale. Throughout the thesis, incoherent NPs are used to design, build, and perform proof of principle coherent control experiments.

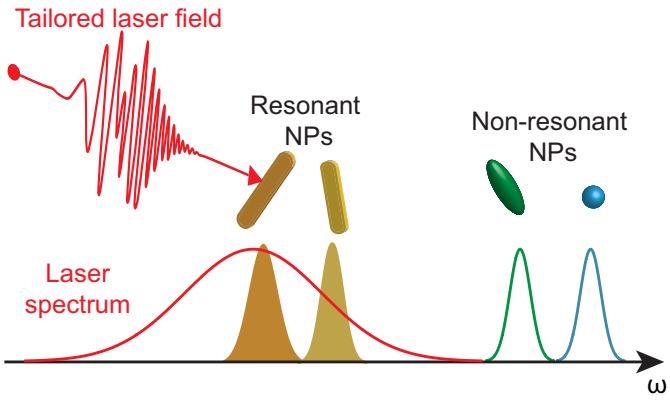

Fig. 1: An ultrashort laser pulse interacts with NPs. By fabricating suitable nanostructures, the resonances can be tuned to overlap with the laser spectrum. Precisely tailored laser fields can actively control light-matter interactions in resonant NPs.

Nonlinear interactions in coherent NPs instead, depend both on the laser field (in amplitude and phase) and on their resonant response. Interesting effects arise from the interaction between coherent NPs and specifically tailored laser fields, and ultrafast coherent control schemes can be used to manipulate them. By combining this ability with the precise fabrication of suitable nanostructures, with resonances precisely tuned to overlap with the laser spectrum, novel applications in nanophotonics, especially in the field of multiphoton imaging can be developed.

Thesis outline

This thesis is organized as follows:

- In Chap. 1 I describe the experimental setup used as well as the theoretical background that is needed for a correct understanding of all the experiments presented in the thesis.
- In Chap. 2 I introduce the use of incoherent dielectric NPs capable of generating second harmonic (SH) to obtain control over ultrafast pulses on very small spatial scales. This experiment provides the basis for real

coherent control at the nanoscale.

- In Chap. 3 I address the second harmonic generation (SHG) from truly coherent plasmonic nanoantennas. In the first part of the chapter I present the measurement of their intrinsic resonant response (both in phase and amplitude). I then discuss the possibility of using plasmonic nanoantennas to create customized SH spectra in nanometric volumes. This can be exploited for an improved imaging technique based on multicolor SH labels.

- In Chap. 4 I present the study of the nonlinear absorption process in semiconductor QDs, which are real quantum emitters (single photon sources) in the solid state. I describe the realization of one of the first closed loop phase control experiments that demonstrates, by using individual QDs and a novel optimization algorithm, coherent control at the level of single molecules and quantum emitters.

- In Chap. 5 I switch again to the investigation of plasmonic nanoantennas, this time considering their nonlinear absorption and emission of photons. I first present an experimental study of the two-photon absorption process in nanoantennas, from which the presence of a coherent regime accessible by ultrashort laser pulses is deduced. I then discuss the design and realization of a real closed loop coherent control experiment on single nanoantennas.

CHAPTER 1

Experimental setup and background concepts

In this chapter I introduce the experimental setup used in all the experiments described in the thesis that enables the study of ultrafast and ultrasmall properties of matter, at the same time providing an active element to exercise control over nonlinear processes. I then review the main difficulties associated with such experimental setup, which are related to the propagation of ultrashort pulses through dispersive materials. I give a short theoretical description of this phenomenon and introduce the basic mathematical formalism used throughout the thesis. Finally, I present the basics of the pulse compression method that will be extensively used in the next chapters.

All the experiments described throughout the thesis were based on the same experimental setup, which consisted of three main components:

- an ultrafast laser source that produced 15 fs pulses;
- a pulse shaper that controlled the spectral phase of the laser field;
- a confocal microscope that allowed the investigation of nonlinear effects in individual nanoparticles.

Combining an ultrashort phase-controlled laser pulse with a confocal microscope therefore constituted our experimental approach to the study and control of light-matter interactions with femtosecond and nanometer resolution. However, this combination has inherent challenges that need to be addressed before performing any experiment. Propagating an ultrafast pulse through optical components such as microscope objectives, greatly distorts the spectral phase and therefore the temporal profile of the pulse. Any experiment that is designed to use ultrashort pulses with dielectric optics has to face this challenge and provide a solution to it. A great advantage of the use of a pulse shaper is that, as well as making it possible to control light-matter interactions, it enables the compensation of phase distortions in the focus of the microscope.

1.1 Laser and pulse shaper

The laser source was a commercial (MenloSystems) Titanium Sapphire laser designed to produce 15 fs laser pulses at a repetition rate of 85 MHz and with average power of ~ 350 mW. In the spectral domain, the laser field was centered around 800 nm, with a bandwidth of ~ 100 nm. In order to control the spectral phase and thus the temporal shape of the laser pulse we used a pulse shaper (adapted from MIIPS-box; Biophotonics Solutions) arranged in a 4-f configuration, with a liquid crystal spatial light modulator (SLM) as the active control element. This approach has proven to be successful in the synthesis and control of customized ultrafast pulses [28–37]. The schematic of a general 4-f pulse shaper arranged in transmission geometry is illustrated in Fig. 1.1. The laser beam comes from the left side of the figure and is dispersed

by a diffraction grating. The diffraction grating is placed exactly at one focal distance f away from a spherical mirror that focuses every frequency component at another focal distance f in its Fourier plane. An active element, in this case an SLM, is placed at this precise position. After the SLM another set of a spherical mirror and a grating recombines all the frequencies into a single collimated beam. In the absence of any modulating element, the pulse shaper is dispersion free, and the output pulse is identical to the input one. Placing a spatial mask like an SLM in the Fourier plane gives the possibility of changing the phase and/or the amplitude of each frequency component, therefore enabling active pulse shaping. As a result, the output pulse is in general different form the input one. Pulse shaping can be used to create the shortest possible pulses (Fourier limited pulses), or a train of identical pulses, or even more complicated pulse structures.

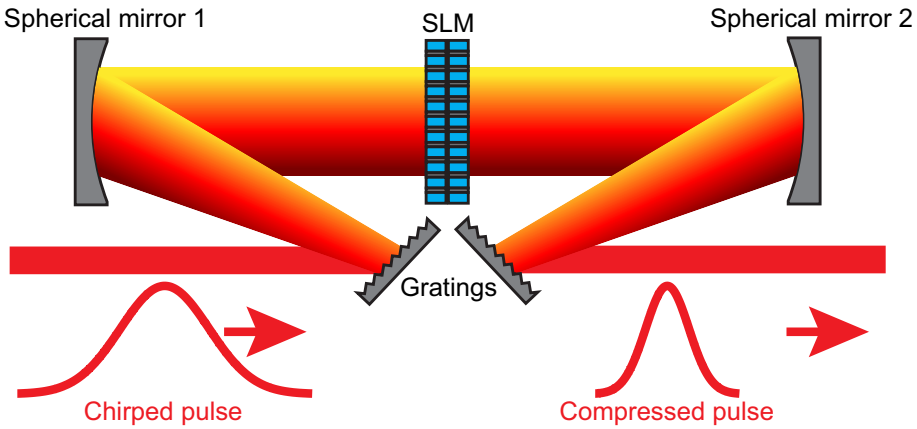

Fig. 1.1: Schematic of a 4-f pulse shaper. In this case the pulse shaper is used to compress in time a chirped pulse.

The SLM used in the experiments was composed by two liquid crystal masks, each of which divided into 640 pixels, whose voltage could be individually manipulated. We used the pulse shaper in a folded geometry [34, 36], in which a mirror placed behind the SLM reflected the beam back to the spherical mirror and the grating. This configuration is easier to align and the working principles are the same as for the transmission geometry of Fig. 1.1. In order to address coherent light-matter interactions, we performed only phase shaping and did not modulate the amplitude of the laser field.

1.2 Confocal microscope

Confocal microscopy was first patented by Marvin Minsky [38] and is a widely used optical technique to achieve high spatial resolution and contrast in microscopy. Confocal microscopy uses point illumination to excite a sample through a microscope objective and raster scans the illumination with respect to the sample to produce two dimensional optical images. The signal emitted by the sample is collected through a microscope objective, which can be the same as the one used for excitation, and projected onto a pinhole that has the function of rejecting the out-of-focus signal that does not come from the sample plane.

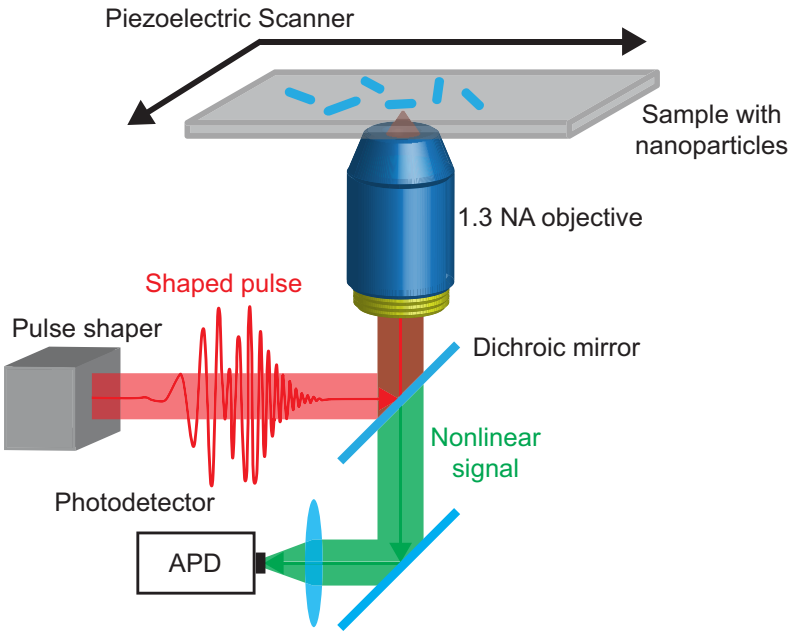

Fig. 1.2: Basic sketch of the confocal microscope used in the experiments. The phase-shaped laser beam is reflected by a dichroic mirror and enters an oil immersion objective. The light emitted by the sample is collected through the same objective, transmitted by the dichroic and focused on an APD.

The actual arrangement used in the experiments is sketched in Fig. 1.2. The ultrafast laser pulse, after phase manipulation by the pulse shaper, was sent to a 1.3 numerical aperture (NA) oil immersion objective, that focused

light to a diffraction limited spot (≥ 310 nm diameter) on a sample containing the investigated NPs. In order to study one NP at a time, their concentration in the sample was sufficiently low to avoid more than one NP at the same time inside the diffraction limited focus of the objective. In the configuration used, the sample was raster scanned with respect to the objective, using piezoelectric scanners. The nonlinear signal from the NPs (second harmonic generation or two-photon induced photoluminescence) was collected by the same objective in a reflection geometry and sent to the photodetectors. The excitation and emission beams were separated by a dichroic mirror and additional spectral filters. The emitted signal was focused with a system of lenses on the detector, an avalanche photodiode (APD) for single photon detection. The active area of the APD together with the system of lenses was chosen such that the image of the APD on the sample plane was a diffraction limited spot. Thus, effectively, the APD itself worked as a pinhole, rejecting all the light that did not come from the desired sample plane and providing the highest spatial resolution. The signal from the sample could also be directed to a spectrometer equipped with an electron-multiplying charge-coupled device (CCD) camera for spectral measurements of very weak signals.

As already mentioned, the combination of an ultrafast pulse and a high NA objective is challenging in itself as the laser pulse has to travel through a big amount of glass before reaching the sample, which results in a dispersed laser pulse. The rest of this chapter describes how a pulse changes upon interaction with dispersive elements and how to practically solve this problem.

1.3 Ultrafast pulses propagating through dispersive media

Ultrafast laser pulses are characterized by a broad spectral content, i.e. many frequency components coexist at the same time. Materials like glass have a frequency dependent refractive index, which implies that every frequency component travels through the material with a different speed, resulting in a distortion of the original pulse [39–42]. Related to a frequency dependent refractive index are also certain spatial distortions that an ultrafast laser beam might undergo after interacting with a medium. All these effects are briefly discussed here.

1.3.1 Phase distortions

I assume a linearly polarized electric field, so that only one field component has to be considered. The time dependent electric filed can be written as

$$E(t) = \frac{1}{2}\sqrt{I(t)}e^{i[\omega_0 t - \phi(t)]} + c.c. \tag{1.1}$$

$I(t)$ and $\phi(t)$ are the temporal intensity and phase of the pulse; ω_0 is the carrier frequency and $c.c.$ means complex conjugate and it is required to make the field real. However, it is easier to describe the propagation of an electric field in the frequency rather than time domain. Fourier transforming Eq. (1.1) yields the frequency dependent electric field

$$E(\omega) = \int E(t)e^{-i\omega t}dt = \sqrt{S(\omega)}e^{-i\varphi(\omega)} \tag{1.2}$$

Here I have introduced the laser spectrum $S(\omega)$ and the spectral phase $\varphi(\omega)$, which are the quantities used in the rest of the thesis, often in the wavelength domain instead of versus frequency. Suppose that the pulse propagates in the z direction and that at $z = 0$, the initial phase of the pulse is zero. At every position z after the origin every frequency component acquires an additional phase $\varphi(\omega) = k(\omega)z$. The pulse at ω and z can be written as:

$$E(\omega, z) = E(\omega, z = 0)e^{-ik(\omega)z} \tag{1.3}$$

The quantity $k(\omega)$ describes the frequency dependent response of the material the laser pulse propagates through. $k(\omega)$ is in general a complex function that can be written in the form $k(\omega) = \beta(\omega) - i\alpha(\omega)$. The term $\alpha(\omega)$ describes the absorption in the material whereas $\beta(\omega)$ gives the dispersion and it is related to the refractive index $n(\omega)$ of the material through $\beta(\omega) = n(\omega)\frac{\omega}{c}$, where c is the speed of light in vacuum. Let me now only focus on the dispersion term and make the approximation that the laser bandwidth $\Delta\omega$ associated with the spectrum $S(\omega)$ is narrow enough so that for every ω in the laser spectral band the condition $|\omega - \omega_0| \ll \omega_0$ is met. For the pulses considered in this thesis this condition holds reasonably well. In this approximation the $\beta(\omega)$ coefficient (and hence the spectral phase $\varphi(\omega)$) can be expanded in a Taylor series around the carrier frequency ω_0, keeping only the leading terms [39–41].

$$\beta(\omega) = \beta(\omega_0) + \left.\frac{d\beta}{d\omega}\right|_{\omega_0} (\omega - \omega_0) + \frac{1}{2} \left.\frac{d^2\beta}{d\omega^2}\right|_{\omega_0} (\omega - \omega_0)^2 + ... \tag{1.4}$$

The zeroth order term $\beta_0 = \beta(\omega_0)$, when multiplied by the coordinate z gives the relative phase of the carrier wave with respect to the pulse envelope. A change in β_0 in the case of many cycle pulses, only slightly shifts the carrier wave from the peak of the envelope and hence changes the electric field very little. In the rest of the thesis, the zeroth order phase will always be set to zero, if not explicitly stated.

The linear term $\beta_0' = \left.\frac{d\beta}{d\omega}\right|_{\omega_0} = \frac{1}{v_g}$ represents the inverse of the group velocity v_g which can be thought to as the velocity at which the envelope of the laser pulse moves. The group velocity differs from the phase velocity, which represents the velocity associated to every frequency component in the laser pulse and is given by $v_p(\omega) = \frac{\omega}{\beta(\omega)} = \frac{c}{n(\omega)}$.

The terms $\beta(\omega_0)$ and β_0' are the only non-zero terms for a non-dispersive medium, i.e. a medium with a constant refractive index. For a frequency dependent refractive index more terms needs to be considered. The second order term $\beta_0'' = \left.\frac{d^2\beta}{d\omega^2}\right|_{\omega_0}$ determines the group velocity dispersion, responsible for pulse spreading and chirping when propagating through materials.

Linear dispersion

The next step is to show how the propagation through a medium affects a laser pulse. Let me start here by considering materials with linear dispersion, for which only the zeroth order and first order term in Eq. (1.4) have to be considered. For simplicity I assume an originally gaussian pulse propagating through a medium for a length L. At $z = 0$, before interacting with the medium, the pulse can be written as

$$E(t, z = 0) = F(t, z = 0) e^{i\omega_0 t} = \exp\left[-\frac{t^2}{2{\tau_0}^2}\right] e^{i\omega_0 t} \tag{1.5}$$

$F(t,0) = \exp\left[-\frac{t^2}{2{\tau_0}^2}\right]$ is the gaussian envelope function and the complex conjugate has been omitted for simplicity. In order to calculate the propagation through a medium one has to Fourier transform Eq. (1.5) and apply the propagator $e^{-ik(\omega)z}$. Inverse Fourier transforming leads to the time dependent pulse at a generic position z. Detailed calculations can be found in [41]. The pulse envelope after a length L for linear dispersion, can be written as:

$$F(t,L) = F(0, L - z/v_g) \tag{1.6}$$

This expression shows that the initial envelope $F(0,t)$ moves as a whole with the group velocity $v_g = c/n$, where $n(\omega) \equiv n$ is the constant refractive index of the non-dispersive material. The temporal shape of the pulse is unchanged and therefore the pulse does not get distorted when propagating in a material with constant refractive index. Eq. (1.6) also provides additional important information. Suppose that two identical pulses propagate through two different materials of refractive indexes n_1 and n_2 but of the same thickness. The pulses propagate with no change to their envelope, remaining identical after the interaction with the two materials, but they experience two different group velocities $v_{g1} = c/n_1$ and $v_{g2} = c/n_2$. As a consequence the two pulses are delayed one with respect to the other. By adding a linear phase term as a function of ω, an ultrashort laser pulse can be delayed in time, without affecting its temporal shape, a result that will be used in the rest of the thesis. In the case of a single pulse, in general, the absolute time the pulse arrives at the sample position is irrelevant. This is why, when measuring the spectral phase of an ultrafast laser pulse, also the linear term (and not only the zeroth order one) in ω is normally not addressed.

Quadratic dispersion

If the second order term in the Taylor expansion Eq. (1.4) is considered, the pulse shape is no longer preserved as the pulse travels through the medium. Instead the pulse spreads and its carrier frequency changes with time, an effect that is called chirp [39–41]. It can be shown that the new pulse width τ_1 and the new instantaneous frequency ω_1 after propagating for a distance L in a dispersive medium becomes:

$$\tau_1 = \left[\tau_0^2 + \left(\frac{\beta_0'' L}{\tau_0}\right)^2\right]^{1/2} \tag{1.7}$$

$$\omega_1(t) = \omega_0 + \frac{\beta_0'' L}{\tau_0^4 + (\beta_0'' L)^2}\, t \tag{1.8}$$

The pulse duration is therefore longer after interacting with the medium and increases with the length L. Also it is possible to see from Eq. (1.7) that for the same amount of dispersion, a shorter pulse gets more distorted after the interaction. In the limit of long initial pulses, i.e. large τ_0, the correction given by the term $\left(\frac{\beta_0'' L}{\tau_0}\right)^2$ is small, whereas it grows bigger the smaller the initial pulse duration. As already mentioned, Eq. (1.8) accounts for the chirp of the pulse after interaction with a dispersive element. The instantaneous carrier frequency of the pulse changes linearly with time, growing bigger or getting smaller depending on the sign of β_0''. In the usual case, for dielectric media and normal dispersion, β_0'' is positive, which means that the ω_1 increases for longer times within the laser pulse.

Complex optical systems can introduce more complicated, i.e. higher order phase distortions, which might heavily change the temporal shape of the laser pulse. High NA microscope objective do in general introduce high order phase contributions [43] and are responsible for distortions in the focal region [44–47]. Compensating for these distortions is therefore crucial for obtaining Fourier limited (FL) pulses.

1.3.2 Spatio-temporal coupling

Related to the dispersion of materials and pulse shaping is also the problem of spatio-temporal coupling [26, 29, 34, 48–53]. A simple example of spatio-temporal coupling is the so-called spatial chirp, which refers to the spatial separation of the different frequency components in a laser beam, normally due to propagation through dispersive optics and/or to poor alignment of the pulse shaper. For example, a beam propagating through a tilted substrate undergoes spatial chirp as its frequency components get refracted differently as

they hit the substrate. Propagation through tilted surfaces must therefore be avoided.

More complex and severe spatio-temporal coupling might result from the 4-f pulse shaper previously described (Sec. 1.1). The origin of this spatio-temporal coupling is a combination of the physical size of the SLM pixels (100 μm in our case) and the optical resolution of the experiment [26, 29, 34, 48, 53]. After the interaction with the first grating and spherical mirror, at the position of the SLM the laser beam has its frequency components separated in space. In this way the SLM can operate in the frequency domain, which is the right domain to manipulate the spectral phase of a beam. To each frequency component reflected by the grating and focused by the spherical mirror, can be associated a finite spatial extent at the SLM plane, which defines the optical resolution. If the spatial extent is too large (poor optical resolution), larger than the physical size of the SLM pixels, then one frequency component will simultaneously interact with different pixels and will be diffracted by the SLM. When applying a phase mask on the SLM, different frequency components will in general be diffracted at different angles thus preventing perfect recombination of all the colors at the output of the shaper. If this type of spatio-temporal coupling is present, the spatial profile of the beam coming out of the shaper will depend on the spectral phase applied by the SLM, which can seriously alter the results of a pulse shaping experiment. In order to minimize this effect, careful design and alignment of the pulse shaper is necessary in order to obtain high optical resolution, where the spatial extent of every frequency component matches the physical size of the SLM pixels. The optical resolution is a function of the incoming beam size, the geometrical factors of the grating and the focal length of the spherical mirror [26, 29, 34, 48, 53]. A different strategy to reduce spatio-temporal coupling in certain conditions is to operate the pulse shaper in a different configuration than the one shown in Fig. 1.1, namely a double-pass configuration. Placing a mirror at the end of the beam path and sending the laser beam back through the 4-f shaper, gives the pulse double the stretching in the temporal domain and cancels certain spatial effects [29, 48, 50]. On the other hand, this configuration is more difficult to align, reduces the output power as a consequence of the double pass through the grating and SLM and does not in general cancels arbitrary spatio-temporal coupling [29, 48].

In any case, to keep spatio-temporal artifacts under control a method to

test (i) the spatial homogeneity of the laser pulse and (ii) if and how the spatial profile of the laser beam changes as a consequence of the application of a phase mask by the pulse shaper is needed.

1.4 Pulse compression

Many techniques are available for pulse diagnostics. The most common ones are frequency resolved optical gating (FROG) [47, 54]; spectral phase interferometry for direct electric-field reconstruction of ultrashort optical pulses (SPIDER) [55]; phase-resolved interferometric spectral modulation (PRISM) [56]; multiphoton intrapulse interference phase scan (MIIPS) [35, 43, 57–59].

MIIPS is the method traditionally used in our group and the one we used in all the experiments described in this thesis. MIIPS relies on the detection of SHG from a nonlinear crystal and its dependence on the spectral phase of the laser field.

1.4.1 Second harmonic generation from broadband pulses

In a broadband laser $E(\omega) = E_0(\omega)e^{-i\varphi(\omega)}$ each frequency component ω can be doubled in order to produce SHG at frequency 2ω. Sum frequency generation (SFG) can equally occur between different fundamental frequencies. For example the frequency components $\omega+\delta\omega$ and $\omega-\delta\omega$ may sum up to generate a sum frequency field also at the frequency 2ω. The definition of the SHG can then be generalized to comprise all the possible fields that can be generated by a sum frequency process between any two fundamental frequencies of the pulse. Mathematically, the SH field is therefore defined as the laser field autocorrelation and the SH spectrum as the squared modulus of it.

$$SH(2\omega) = \left| \int |E_0(\omega+\Omega)|\,|E_0(\omega-\Omega)|\, e^{i[\varphi(\omega+\Omega)+\varphi(\omega-\Omega)]}\, d\Omega \right|^2 \tag{1.9}$$

For a broadband pulse, there are many different paths to create the same field at the frequency 2ω. Because they are all phase related, these fields can interfere with each other, and the way they do it (constructively or destructively) depends on their relative phase. From Eq. (1.9) one can deduce that the

field component at the frequency 2ω generated by the pure frequency doubling process of two photons at frequency ω picks up the total phase $\varphi_{SH} = 2\varphi(\omega)$, whereas the field at the same frequency 2ω generated by the sum frequency generation of the photons at the frequencies $\omega+\delta\omega$ and $\omega-\delta\omega$ picks up the phase $\varphi_{SFG} = \varphi(\omega+\delta\omega)+\varphi(\omega-\delta\omega)$. Depending on the phase difference between φ_{SH} and φ_{SFG}, the two fields add up in phase or not and generate more or less total amplitude at the frequency 2ω. The highest SH intensity at all the possible frequencies 2ω is obtained for a FL pulse, namely when all the nonlinear terms in the Taylor expansion Eq. (1.4) are zero. MIIPS precisely tries to maximize all the frequency components in the SH spectrum, which should lead to the shortest possible pulse. Manipulating the interference among all the different paths that can create the same frequency component in the SH range, can be viewed as a simple example of coherent control experiment [24, 25, 57, 58].

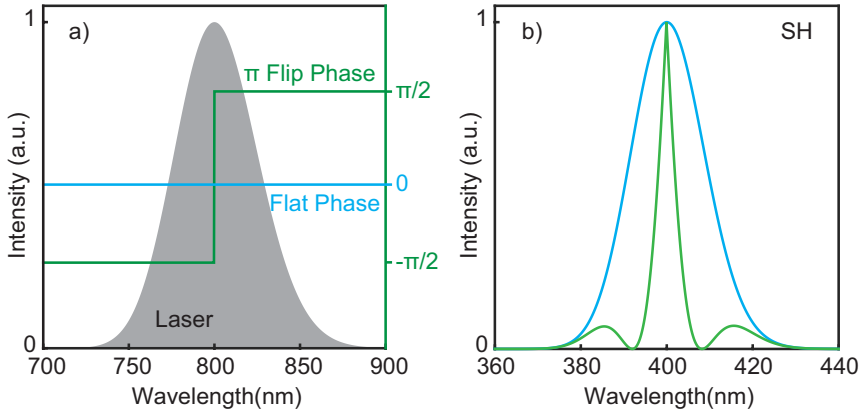

Fig. 1.3: a) Example of a gaussian laser spectrum and two different spectral phases. b) SH spectra for the two different phases.

To show the strong dependence of the SH spectrum of a broadband laser pulse on the spectral phase, in the graphs of Fig. 1.3 examples a gaussian laser spectrum with two different spectral phases (a) and the corresponding SH spectra (b) are reported. The SH spectra are calculated using Eq. (1.9). The cyan curve in Fig. 1.3 b corresponds to a flat spectral phase, i.e. to a FL pulse whereas the green curve is obtained for the green spectral phase of Fig. 1.3 a, namely a step function of amplitude π. As one can see, the SH spectrum of a FL pulse has a higher intensity than the other for all wavelengths. The green

spectrum alternates regions in which the SH intensity is as high as in the FL case and regions where the destructive interference of the paths produces zero total amplitude. In general, in the case of a continuous laser spectrum, multiple peaks in the SH spectrum are a symptom of a distorted spectral phase.

1.4.2 MIIPS

As some of the results presented in the next chapters are based on this technique, this section briefly introduces the principles of MIIPS. A more thorough description can be found [35, 43, 57–60].

The objective of MIIPS is to produce FL pulses at the position where the experiment is carried out. MIIPS accurately measures the phase distortions of the laser pulse at the sample position and corrects for them. The tools that MIIPS uses to accomplish this are: (i) a pulse shaper based on an SLM; (ii) a second harmonic crystal to generate SH at the sample position; (iii) a spectrometer to measure the full SH spectrum.

During a MIIPS iteration a series of reference phase functions is applied by the SLM. For every applied reference phase the full SH spectrum is measured. After one iteration, the spectral phase of the laser pulse, or to be more precise, the nonlinear terms in the spectral phase are measured. The inverse of the measured spectral phase is then applied as a phase mask by the SLM, which should correct for phase distortions. Several iterations are performed in order to refine the applied phase and hence the pulse compression.

A popular set of reference phase functions (although not the only possibility) used in MIIPS are cosine phases as a function of the frequency ω and of the parameter δ [35, 43, 57–59].

$$\varphi_{\mathrm{MIIPS}}(\omega,\delta) = \alpha \sin(\gamma\omega - \delta) \tag{1.10}$$

The parameter δ (also called phase offset) is normally varied between 0 and 2π in 128 steps and for every value of δ the complete SH spectrum is measured. This way one can construct a two-dimensional spectrogram, from which the initial phase of the laser pulse can be extracted. The SH spectrum as a function of ω and the parameter δ can be written as:

$$SH(2\omega,\delta) = \left| \int |E_0(\omega+\Omega)|\,|E_0(\omega-\Omega)| \right.$$
$$\left. e^{i[\varphi(\omega+\Omega)+\varphi(\omega-\Omega)+\varphi_{\mathrm{MIIPS}}(\omega+\Omega,\delta)+\varphi_{\mathrm{MIIPS}}(\omega-\Omega,\delta)]}\, d\Omega \right|^2 \tag{1.11}$$

Using this equation one can calculate MIIPS spectrograms (or traces) for a given laser spectrum $S(\omega) = |E_0(\omega)|^2$ and a given spectral phase $\varphi(\omega)$.

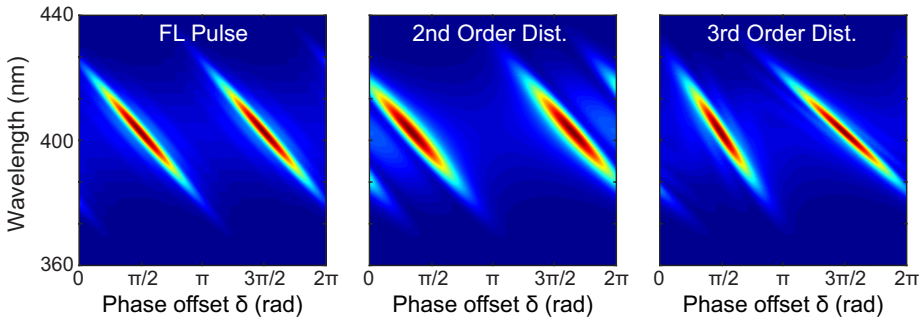

Fig. 1.4: Simulated MIIPS traces for the parameters $\alpha = 1.5$, $\gamma = 16$ fs in the case of a Fourier limited pulse, a pulse with second and third order phase distortions respectively.

Fig. 1.4 shows three different calculated MIIPS traces, based on the laser spectrum shown in Fig. 1.3. From left to right the traces correspond to a FL pulse, a pulse that is subject to second and third order phase distortions respectively. The y-axis of the traces corresponds to the SH wavelength whereas the x-axis represents the variation of the parameter δ between 0 and 2π. It is useful to think of a MIIPS trace as been formed by two different periods: the 0 to π and the π to 2π period. In the case of a FL pulse, these periods are completely equivalent and they become different as phase distortions are added to the pulse, as shown in Fig. 1.4. In the case of FL pulses the points of maximum SH intensity lie on two parallel straight line separated by π radians. The effect of second order phase distortions is to shift these lines horizontally, bringing them close together or moving them apart depending on the sign of the second order phase. Third order phase distortions tilt the two lines with respect to each other such that they are no longer parallel. Higher order phase effects can considerably change the MIIPS traces with respect to the FL case.

The MIIPS method was developed in the early 2000s [43, 57, 58] and pulse compression in the focus of high NA objectives using MIIPS was demonstrated almost 10 years ago [43, 59] for ultrafast microscopy applications. However, even higher spatial resolution is needed for performing pulse shaping experiments in individual NPs. In the next chapter I introduce a nanometer version of MIIPS that provides a good solution to this problem.

CHAPTER 2

Pulse control at the nanoscale

In this chapter I describe the method we developed to obtain full control over ultrashort pulses on a sub-diffraction-limited area in a confocal microscope. Such method extends the MIIPS technique to the use of second harmonic nanoparticles of deep subwavelength dimensions, which allows the diffraction limit to be beaten. I show that small non-resonant nanoparticles are ideal systems to prove pulse compression, phase measurement and precise phase delivery to the nanoscale, as well as to check for possible spatial artifacts in the focus of the microscope, which are all necessary prerequisites for real pulse shaping and coherent control experiments that will be discussed in the rest of the thesis.

This chapter is based on:

- **Accanto N**, Nieder JB, Piatkowski L, Castro-Lopez M, Pastorelli F, Brinks D, & van Hulst NF. *Phase control of femtosecond pulses on the nanoscale using second harmonic nanoparticles.* Light Sci. Appl. 3, e143 (2014)
- Piatkowski L, **Accanto N** & van Hulst NF. *Ultrafast meets ultrasmall: controlling nanoantennas and molecules.* ACS Photon. Review (2016)

In experimental science it is crucial to verify that the outcome of any experiment is trustworthy or, in other words, that it is a manifestation of the natural phenomena under investigation, and is not due to the particular experimental arrangement. The more complicated the experiment, the harder and the more important it becomes to keep all the apparatus under control and prevent spurious results.

The objective of this thesis is to address coherent light-matter interactions and demonstrate phase shaping experiments at the level of single NPs using the apparatus detailed in Chap. 1. Experimentally, this was achieved by exciting individual NPs in the focus of a high NA objective using ultrafast pulses and changing the phase of the pulse to extract information about the coherence of the NPs. In order to perform similar experiments one needs (i) to have precise knowledge of the exact pulse shape at the NPs and (ii) to properly deliver the desired spectral phases to the subwavelength region where the NPs sit. A method to probe the spectral phase of the laser pulse in the focus of the microscope objective with higher than diffraction-limited spatial resolution is therefore necessary. The MIIPS method introduced in the previous chapter, like other pulse characterization techniques, in its standard implementation makes use of a bulk SH crystal to obtain the spectral phase information, and hence does not provide sufficiently high spatial resolution.

In this chapter I describe a nanometer version of MIIPS that we developed, which relies on the use of SH NPs of typical sizes of ~ 100 nm as local probes for ultrafast laser pulses. The goal of this chapter is to demonstrate that phase characterization and pulse compression can be performed based on signals originating from individual NPs.

2.1 Second harmonic nanoparticles

For this study we used SH NPs of different materials: barium titanate ($BaTiO_3$), purchased from Sigma-Aldrich, iron iodate ($Fe(IO_3)_3$), purchased from PlasmaChem, and gold (Au), purchased from BB International, as illustrated by the scanning electron microscope (SEM) images of Fig. 2.1.

$BaTiO_3$ and $Fe(IO_3)_3$ were dispersed in ethanol, sonicated, deposited onto a glass microscope coverslip and dried. The $Fe(IO_3)_3$ NPs had mean size of

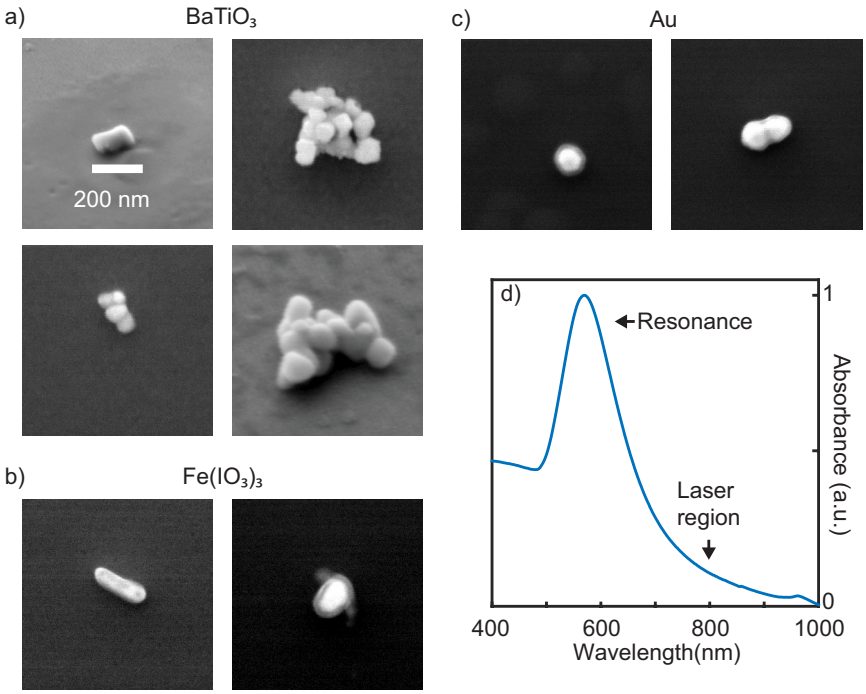

Fig. 2.1: a-c) SEM images of the investigated nanoparticles. d) Absorbance of the gold NPs showing a plasmonic resonance at 580 nm

150 nm and were homogeneously distributed in the sample, whereas in the case of $BaTiO_3$ an inhomogeneous distribution of single NPs and small aggregates with sizes ranging from one hundred to a few hundred nanometers was found. The $BaTiO_3$ NPs were thus used for size and shape dependent experiments.

Both $BaTiO_3$ and $Fe(IO_3)_3$ belong to the category of non-centrosymmetric metal oxides [61–70] and have recently been proposed as a promising alternative to fluorescent probes in multiphoton biological imaging [63, 67, 69]. With respect to commonly used fluorescent markers, SH NPs present a much higher photo-stability, which allows long observation times, emit in a relatively narrow spectral range, so they can be easily spectrally separated from unwanted sample auto fluorescence, and can be excited with near infrared light, which limits photo-damage of the sample and increases the penetration depth for deep tissue imaging [67, 69, 71]. A disadvantage of using these NPs for bi-

ological labeling is that they are in general bigger than standard fluorescent markers, which makes the perturbation of the targeted system larger.

The Au NPs were synthesized in the shape of nano-spheres with diameter of 100 nm, suspended in water solution and drop casted on the glass coverslip. Gold is a centrosymmetric material, which implies that SHG can only occur at the surface of the NPs or in the presence of a high field gradient [72–74]. SHG from gold NPs has been studied in many different experimental and theoretical works, mainly in the context of plasmonic enhanced nonlinearities [75–80]. Gold NPs are biocompatible and also have the potential to be used as markers for multiphoton imaging [81].

Because ~ 100 nm NPs are smaller than the excitation wavelength, phase matching conditions for the SHG do not apply [70]. As a consequence, efficient SHG can be achieved from a very broad wavelength range without the need to specifically tune the NPs size or to change their orientation with respect to the incident light. These advantages make NPs more cost effective and easier to handle than their bulk crystal counterpart. The great potential of SH NPs for the field of ultrafast pulse diagnostics was already recognized by Extremann [68], Wnuk [61], Li [82] and their collaborators. However, for NPs to be suitable local probes of the laser pulse, one must be sure that they do not contribute any additional phase or amplitude information, or in other words, they must have a spectrally flat response in the region of the laser spectrum. This is surely true for dielectric materials as $BaTiO_3$ and $Fe(IO_3)_3$, which have no resonances in all the visible and infrared region of the spectrum [70], but might not be the case for Au NPs. It is well known that metallic NPs can present surface plasmon resonances that may overlap with the laser spectrum [83, 84] and therefore distort the precise measurement of the laser spectral phase. In fact, the study of resonant metallic NPs and their interaction with ultrashort laser pulses is the main focus of this thesis (see Chap. 3 and Chap. 5). Here instead, such resonances need to be avoided and hence gold NPs were deliberately chosen to have plasmon resonances outside the laser spectrum, as confirmed by absorption measurements on a highly concentrated solution of the Au NPs (Fig. 2.1 d). The graph shows a pronounced surface plasmon resonance with a peak around 580 nm, whereas almost flat response is visible in the region of the laser spectrum (between 750 and 850 nm). This ensures that all the three species of NPs were suitable nanometer probes of the laser pulse and could be used for nanoscale ultrafast pulse compression and control.

2.2 Pulse compression on single NPs

This section describes the pulse compression experiment carried out on single $BaTiO_3$ NPs (which constitute our reference NPs) in the focus of a high NA objective.

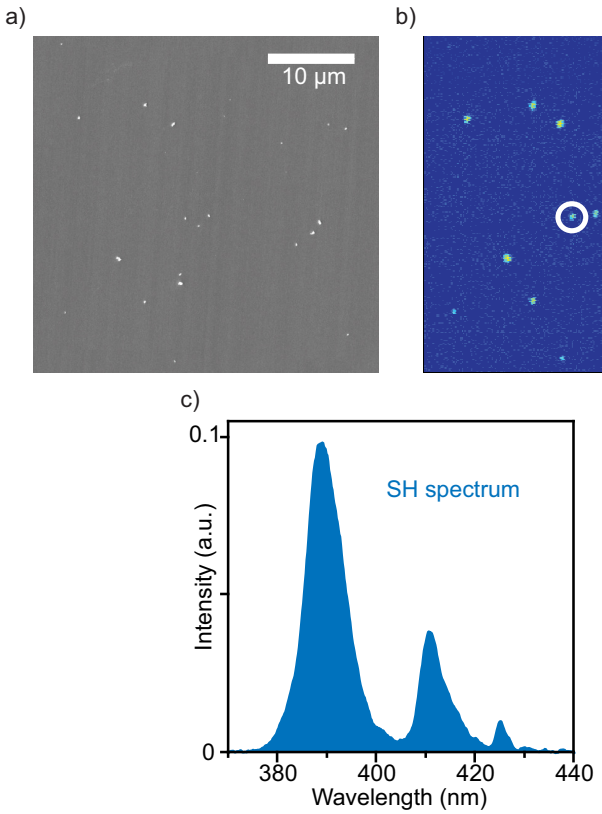

Fig. 2.2: a) SEM image of the investigated area of the $BaTiO_3$ sample. b) SH image of the same area of the sample. Pulse compression was carried out on the circled NP. c) SH spectrum of the chosen NP before pulse compression

Fig. 2.2 a and b show side by side a SEM image and a SH image of the same area of the sample. In the SH image, every bright spot corresponds to the SH generated by a single $BaTiO_3$ NP (or a small aggregate of NPs). The use of reference markers in the sample allowed us to identify the right sample area and measure SEM images after the optical experiments. The SH image was taken

exciting through the high NA microscope objective with an uncorrected pulse, i.e. with zero phase applied by the SLM. The average laser power used in this experiment was 6 mW, and the $BaTiO_3$ NPs were found to be very stable under this excitation power. The laser polarization in all the experiments described in this chapter was kept linear before entering the microscope objective.

The circled NP in Fig. 2.2 b, which after SEM inspection was found to have a mean dimension of 180 nm, was chosen to perform the nanoscale pulse characterization and compression experiment. The graph of Fig. 2.2 c shows the SH spectrum measured on this NP before pulse compression. The integration time was set to 0.8 s for this acquisition. The spectrum is made up of three different peaks, a sign of spectral phase distortions (as discussed in Sec. 1.4), mainly due to the microscope objective and other dielectric optics such as the dichroic mirror at the microscope. Importantly, Fig. 2.2 c demonstrates that the complete SH spectrum, even from a single 180 nm NP, could be measured with a good signal to noise ratio with a relative short integration time.

We then proceeded to compress the pulse by performing MIIPS on the single NP chosen. The results of this experiment are shown in Fig. 2.3. The first MIIPS iterations (Fig. 2.3 a), performed starting from zero phase applied by the SLM corresponds to a very distorted laser pulse, where high order phase distortions (higher than third order) are present. Few MIIPS iterations were needed to compensate for these distortions. The trace in Fig. 2.3 b corresponds to the last MIIPS iteration, showing a very clean spectrogram, suggesting a nearly FL pulse. Typically, fewer than 10 MIIPS iterations were needed to compensate for the phase distortions and full pulse compression at the nanoscale could be achieved in less than 15 min, where standard MIIPS using bulk SH crystals usually takes about 1 min.

Fig. 2.3 c shows the laser spectrum and the spectral phases measured by MIIPS after the first and last iteration, namely the phases corresponding to totally uncorrected and FL pulses respectively. The curve corresponding to the initial phase is very distorted, spanning over ~ 50 rad across the laser spectrum. Our nanometer MIIPS method successfully compensated for such a big amount of phase distortions eventually producing a very flat (undistorted) spectral phase. Finally, Fig. 2.3 d shows the evolution of the SH spectrum from the same NP measured after different MIIPS iterations. This graph demonstrates that, as MIIPS proceeded in the experiment, and the pulse was com-

pressed in time, the SH intensity grew bigger and the SH spectrum became more similar to theoretical predictions for FL pulses. After pulse compression, the integrated SH intensity collected from the NP increased by a factor of ~ 15.

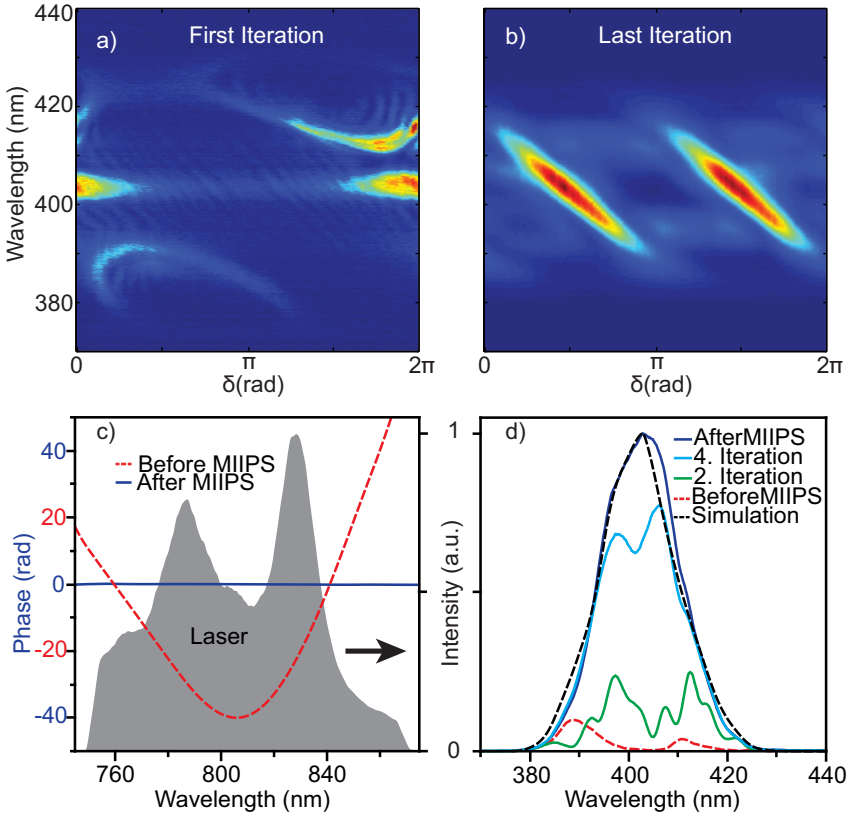

Fig. 2.3: a) First MIIPS iteration on the selected NP showing a very distorted laser pulse. b) Last MIIPS iteration on the selected NP corresponding to a FL laser pulse. c) Laser spectrum (shaded region) and spectral phase retrieved by MIIPS after the first (red dashed curve) and last (blue solid curve) iteration. d) SH spectra measured on the selected NP after different MIIPS iterations. The black dashed curve is a simulated SH spectrum for FL pulses.

The increase in the SH signal is of crucial importance in multiphoton microscopy, as it improves the signal to noise ratio and it allows smaller signals to be detected, as can be noticed from a comparison between Fig. 2.4 a and b. The red arrows in Fig. 2.4 b point to two NPs that were not detectable using uncompressed pulses, but became visible after pulse compression, with the

same integration time. From SEM images these NPs had a size of ~ 120 nm.

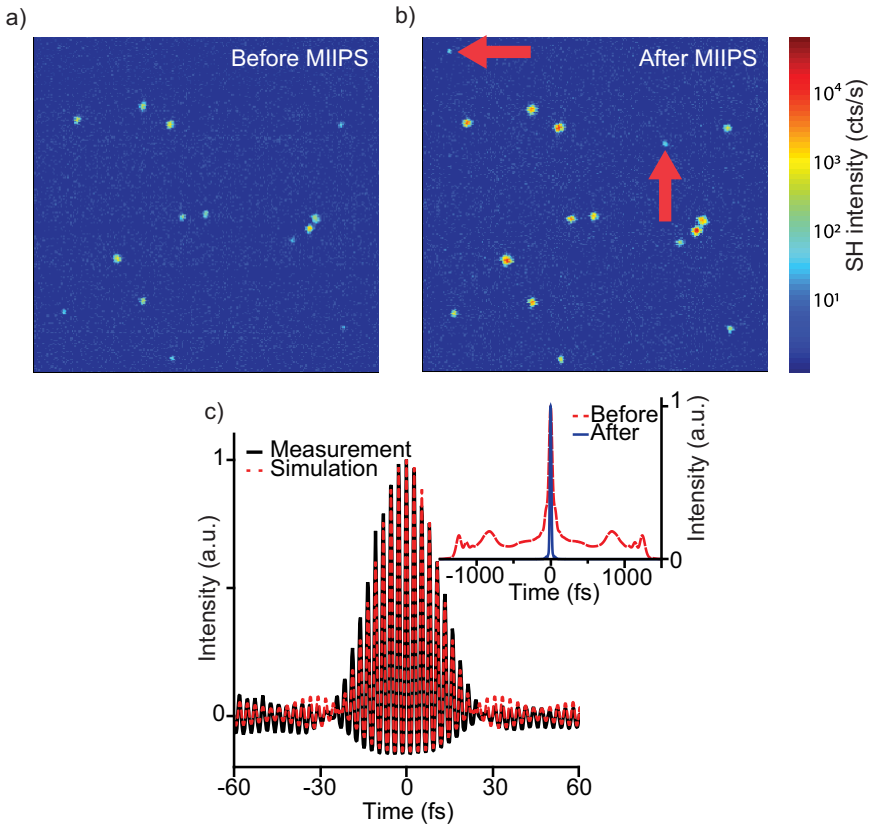

Fig. 2.4: a) SH image of the sample before pulse compression. b) SH image of the sample after pulse compression. c) Simulated (red dashed line) and measured interferometric autocorrelation (black line) of the compressed 17-fs pulse. Inset: Calculated time profile of the uncompressed (dashed red line) and compressed pulse (blue curve).

Finally, as an independent verification of the FL character of the compressed pulse, we acquired an interferometric autocorrelation trace of the final laser pulse using the SH emitted by the same NP. Such a trace was measured by scanning the relative time delay of two replicas of the original pulse generated by the pulse shaper, as described in [85]. The graph in Fig. 2.4 c shows the integrated SH intensity as a function of the time delay between the pulse replicas and compares it to theoretical calculations. The interfer-

ometric autocorrelation function has a full-width at half-maximum (FWHM) of 23.6 fs, which, for a Gaussian pulse, corresponds to a pulse duration of 16.7 fs (FWHM), and is in good agreement with the calculations. To illustrate the dramatic effect of the compression on the time profile of the laser pulse, the inset of Fig. 2.4 c shows the calculated intensity autocorrelation for the pulse before and after compression. For the compressed pulse, a single narrow peak with a FWHM of 23.6 fs is observed, whereas in the case of the uncompressed pulse, a much broader central peak (56 fs FWHM) can be seen, superimposed on a very broad pedestal containing 85% of the total integrated intensity and extending up to ± 1 ps from the central peak.

The results shown so far demonstrate our capability of (i) measuring spectral phases with sub-diffraction-limited spatial resolution; (ii) compressing laser pulses using the SH from a nanometric volume; (iii) delivering the shortest femtosecond pulses to the nanoscale. What still needs to be proven is that these conclusions are independent (as they must be) on the specific NP selected and that arbitrary phases, i.e. arbitrary pulses, and not only FL pulses can be delivered to nanometric regions.

2.3 Independence on the nanoparticle studied

This section describes a series of experiments we performed in order to test the independence of the results on the specific NP used, in terms of orientation, shape, size and material.

In a first experiment, the accuracy of the nanometer phase measurement was tested on 15 different $BaTiO_3$ NPs, which provided a large distribution of sizes, shapes and orientations, as demonstrated by the representative images of Fig. 2.1 a. The experiment was performed as follows: first the pulse was compressed in time using the SH emitted by a single NP. Next, phase measurements of the compressed pulse were carried out on the 15 different $BaTiO_3$ NPs labeled in the SEM image of Fig. 2.5 a. The NP labels reflect the order at which the specific NP was addressed. For instance, NP10 was measured after NP9 and before NP11. The results of these phase measurements are reported in Fig. 2.5 b. Very good agreement among the spectral phases measured on different NPs can be seen. However, one can notice the tendency of the spectral phase to decrease at the edges of the laser spectrum on NPs measured

at later times (green curves). This can be explained with some instability of the experimental setup (the laser itself or the phase on the SLM for example) that caused the laser pulse to acquire some minor phase distortion (less than 0.5 rad) as the measurement time elapsed (45 min between the first and the last phase measurement). Apart from this minor instability, the phase measurement was independent on the particular $BaTiO_3$ NP chosen. Moreover, if one considers only the area of the fundamental spectrum in which the intensity is above 30% of the maximum, i.e. where the phase measurement is the most reliable, then the mean phase varied by less than 0.3 rad and the standard deviation was below 0.15 rad (Fig. 2.5 c), whereas the initial phase distortions, before MIIPS compensation, were greater than 50 rad. This strongly confirms the good level of compensation obtained and the independence of our method on the size, shape and orientation of the NP. The independence on the orientation in turn immediately proves that the polarization of the incoming beam was not an issue, and that the correct phase measurement was obtained regardless the specific polarization used with respect to the orientation of the NPs.

In order to demonstrate the independence on the material of the NPs we proceeded as follows: first, the laser pulse was compressed on a single $BaTiO_3$ NP, retrieving a phase with variations of less than 0.3 rad over the laser spectrum, as described above. Then, several phase measurements were performed on different $BaTiO_3$ NPs to obtain the mean phase and standard deviation. Next, we switched to either the $Fe(IO_3)_3$ or the Au sample and performed a new phase measurement on a single NP starting from the previously compressed laser pulse. The resulting phase was then compared to the mean phase and standard deviation obtained on $BaTiO_3$ NPs. The laser power for the $Fe(IO_3)_3$ and Au samples was reduced to 0.5 mW (for $Fe(IO_3)_3$) or lower (for Au) to avoid damage of the NPs. Even with this smaller power the full SH spectra could still be measured with a relatively small integration time (1 to 5 s). As illustrated in Fig. 2.5 d, for the $Fe(IO_3)_3$ NPs, the measured phase was well within the standard deviation obtained previously for the $BaTiO_3$ NPs. In the case of Au NPs, the measured spectral phases only differed by 0.2 rad from the standard deviations measured for $BaTiO_3$ NPs, with the Au dimer (red line), namely an aggregate of two attached gold spheres (see Fig. 2.1 c), being closer to the standard deviation than the single Au NP (blue curve). As explained in the next section and shown in Fig. 2.6, this can be attributed to the lower

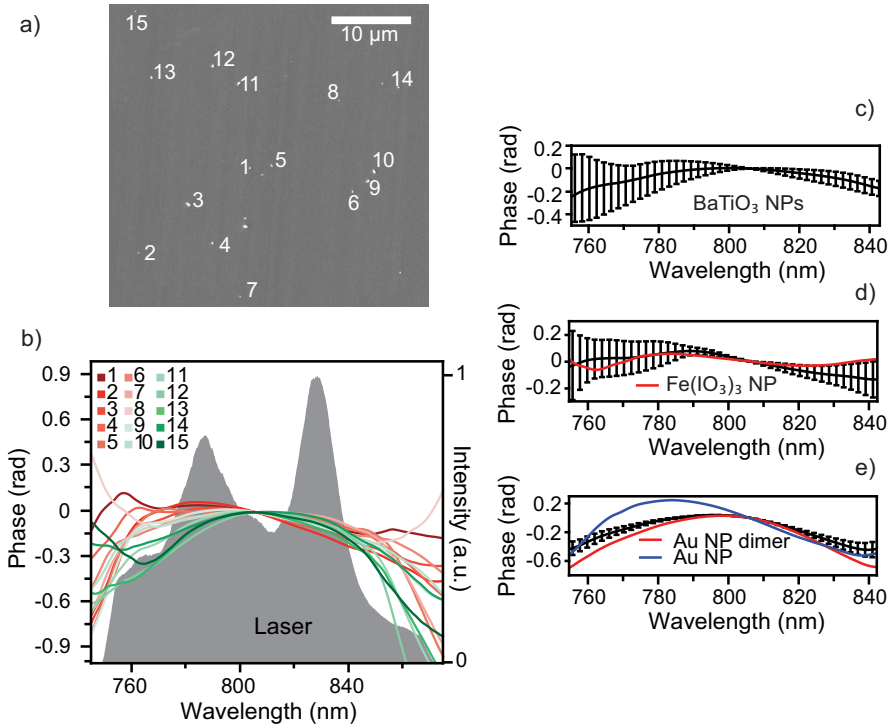

Fig. 2.5: a) SEM image of the sample area showing the 15 $BaTiO_3$ NPs used to perform the phase measurement. The NP labels reflect the order at which the specific NP was addressed. b) Laser spectrum (shaded region) and spectral phases measured on the 15 NPs indicated after MIIPS. c) Mean spectral phase over the 15 measurements.The error bars represents the standard deviation. Spectral phase measured for one (d) $Fe(IO_3)_3$NP (red line) and (e) Au dimer (red line) and Au monomer (blue line). The error bars are the standard deviations obtained from repeated measurements of $BaTiO_3$.

signal to noise ratio available for these NPs and to the presence of additional nonlinear contributions (two-photon absorption) that hampered an accurate phase measurement. Indeed for the the single Au NP, as a consequence of the lower SH signal, the integration time for every spectral acquisition had to be increased up to 5 s. Despite these difficulties, the phase measurements obtained on Au NPs to a good approximation reproduced the phase measured on $BaTiO_3$ NPs.

The results of this section confirm that the NPs investigated were all good

nanometer-sized probe for ultrafast laser pulses. They all produced reliable spectral phase measurements with high spatial resolution without affecting the laser pulse. This in turn implies that, in a sample of $BaTiO_3$, $Fe(IO_3)_3$, or non-resonant Au NPs, one can arbitrarily select any NP to perform pulse characterization and compression.

2.4 Control of the SH emission from NPs

For the purpose of this thesis, it needs to be proven that arbitrary pulses, and not only FL ones, can be delivered to the nanoscale. In order to do so we measured the SH spectra of individual NPs for different test phases applied by the SLM and compared them to simulated SH spectra. The test phases included the phase after compression, corresponding to a FL pulse, the phase before pulse compression (corresponding to distorted pulses) and a phase mask with a π phase step between the short and long wavelength parts of the laser spectrum (see inset of Fig. 2.6). The latter phase mask was used in several experiments by other groups to demonstrate coherent control over different nonlinear processes [86–88]..

The results of Fig. 2.6 a-d demonstrate the good agreement between experimental SH spectra and theory for all the NPs investigated. The SH for the Au NPs, and in particular in the case of the single Au sphere, presented additional spectral contributions at the long wavelength side, as shown in Fig. 2.6 c,d. This contribution can be attributed to two-photon absorption (TPA) in gold followed by two photon induced photo-luminescence (TPPL) that has extensively been studied in literature [89–93]. In the experiment described here, especially for the single Au NP, the TPPL was a source of noise for the SH signal that could explain the less precise phase measurement obtained on these NPs (Fig. 2.5 e). Chap. 5 will describe a detailed study of the TPA and TPPL in resonant nanoantennas.

The results of this section confirm our ability to accurately deliver designed spectral phases to the nanoscale, which is essential for coherent control experiments. Additionally, they also show that the investigated NPs can be considered as nanometer sources of easily tunable, coherent blue light, with wavelengths precisely controlled by the application of the proper spectral phase. This ability, combined with the intrinsic response of resonant metallic

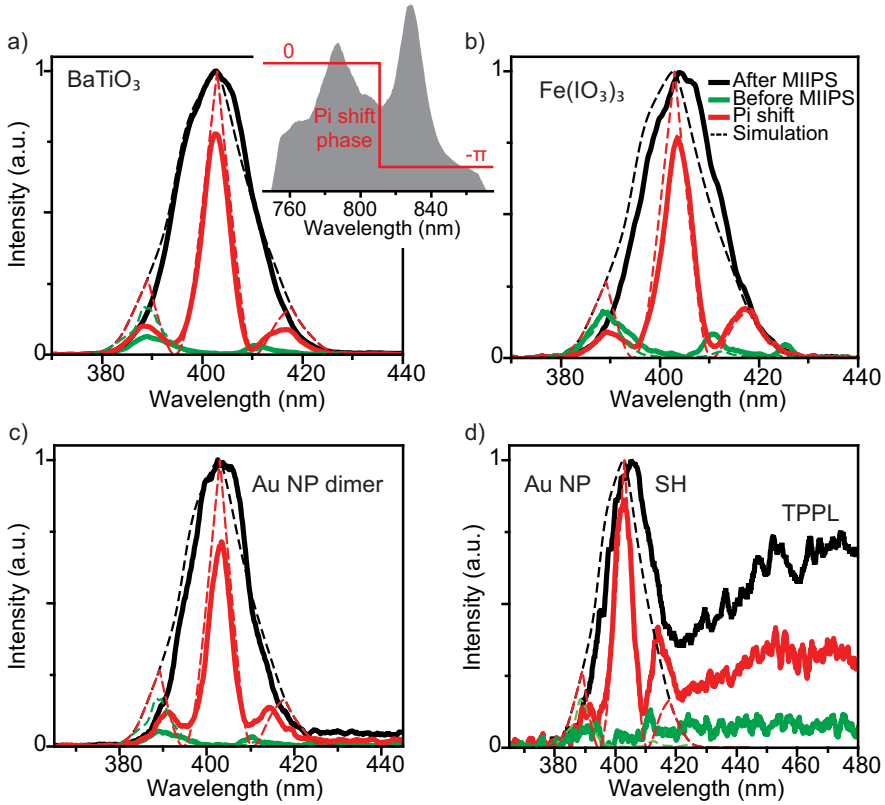

Fig. 2.6: Inset: Laser spectrum with the spectral phase corresponding to a π phase difference between the short and long wavelength parts of the laser spectrum. a-d) Measured and simulated SH spectra for the different applied phases (phase after compression, before pulse compression and π step) corresponding to the indicated species of NPs. In the case of the Au NPs, the wavelength axis extends to higher wavelengths to highlight the contribution from TPPL.

NPs, will be exploited in Chap. 3 to demonstrate a novel imaging technique based on SH labels.

2.5 Spatial considerations

This section addresses the issue of possible spatio-temporal coupling at the focus of the laser beam. As described in the previous chapter, spatial chirp is

the condition in which the spatial profile of an ultrafast laser beam is not homogeneous. The NPs described here, can function as sub-wavelength probes for the laser beam. Each NP in the experiment, depending on its relative position with respect to the focus and its specific size, shape and orientation, probed a different sub-volume of the excitation spot. Therefore, the independence of the phase response as well as the SH spectra on the specific NP (see Fig. 2.5 and Chap. 2) is a proof that different sub-volumes in the excitation spot had the same spectral properties (phase and amplitude). In other words, there was no measurable spatial chirp inside the focal volume.

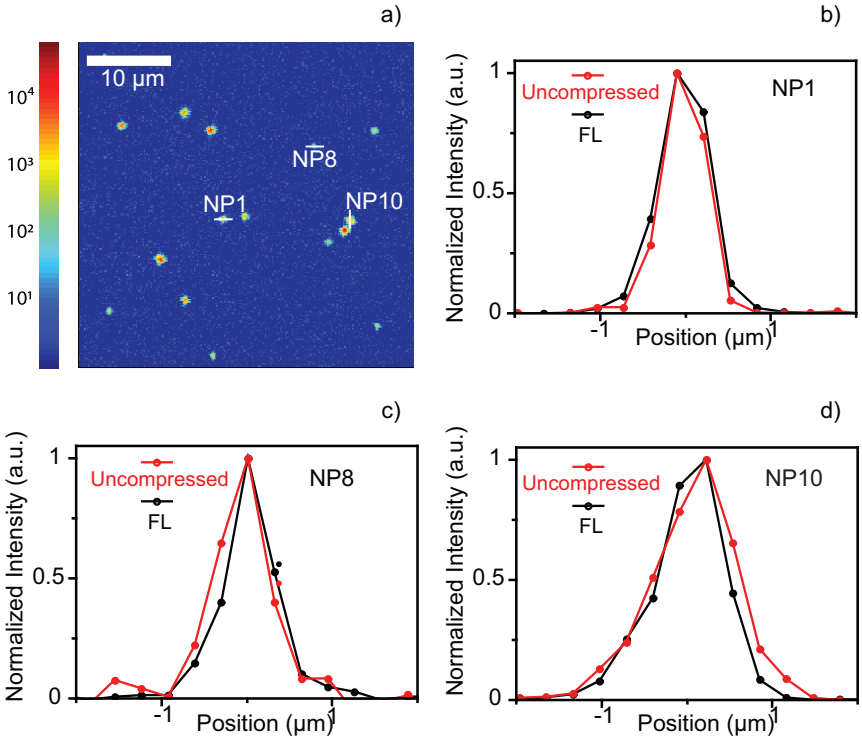

Fig. 2.7: a) SH image of a sample containing $BaTiO_3$ NPs. The indicated NPs are the ones considered for the analysis of spatio-temporal coupling. The white horizontal and vertical lines generate the lateral sections plotted in b-d) that are shown for the FL as well as the uncompressed pulse case.

A second important check of possible spatio-temporal coupling can be performed by measuring the spatial profile of the laser spot with different applied masks on the SLM. In the case of poor shaper alignment or exces-

sively large phases, the application of a phase mask on the SLM might cause a change in the spatial profile of the laser beam. The SH image of Fig. 2.7 a shows different $BaTiO_3$ NPs and was acquired using FL pulses (is the same as the one in Fig. 2.4 b). In this image three different NPs are indicated, which correspond to NP1, NP8 and NP10 of Fig. 2.5 a. Taking cuts through the SH spots corresponding to the different NPs, the lateral sections shown in Fig. 2.7 b-d were obtained. These graphs compare the lateral section for the indicated NPs, in the case of extreme phase masks used in the experiment, namely zero applied phase (red curves) and FL pulses (black curves). The solid points superimposed on the curves correspond to the pixilation used in the image (as explained in Chap. 1, the two-dimensional images were obtained by raster scanning the sample). The spatial resolution of the scan was 150 nm. From SEM images NP1 had mean size of 180 nm, NP8 of 150 nm, NP10 was an oblate spheroid, with long axis of 500 nm and short axis of 200 nm. NP1 and 8 produced nearly diffraction limited spots for SH (the lateral images for these particles have FWHM $\sim$ 290 nm), while NP10 has FWHM $\sim$ 400 nm. The results of Fig. 2.7 show that, within the spatial resolution of the experiment there was no difference between the lateral sections of the SH spots for compressed and completely uncompressed pulses, ruling out also this type of spatio-temporal coupling.

The ability to test for spatio-temporal inhomogeneities inside the excitation spot is a unique advantage of using NPs as opposed to SH bulk crystals and provides a tool for correctly designing pulse shaping experiments on the nanoscale.

2.6 Conclusions

In this chapter I have shown that our experimental approach, which makes use of ultrashort phase-controlled pulses to excite single NPs in the focus of a high numerical aperture objective, is suitable for precise phase and time investigation on the nanoscale. Using SH NPs I have demonstrated ultrashort pulse compression, precise and reproducible phase measurement, accurate phase delivery and pulse control with high spatial resolution. SH NPs can also be used as sub-diffraction probes of the laser focal volume, and to rule out possible spatio-temporal coupling coming from a bad operation of the exper-

imental setup. All together, these achievements constitute a complete toolbox for correctly setting up pulse shaping experiments in single NPs. With this at hand, the other experiments described in this thesis become possible.

All the NPs studied in this chapter, have been used as nano-probes for biological imaging [67, 69, 81]. The pulse compression and control described here, could therefore lead to improvements in multiphoton microscopy. Pulse compression directly inside a biological tissue might be possible, which could help the detection of small nonlinear signals. Moreover, the precise phase shaping ability makes SH NPs real nanometer-sized sources of easily tunable blue light.

In the next chapter I extend the approach used here to the study of NPs that carry a resonant response: plasmonic nanoantennas.

CHAPTER 3

Resonant effects in plasmonic nanoantennas

In this chapter I introduce the main concepts associated with plasmonic nanoantennas and their localized surface plasmon resonances. The very short, but still accessible, plasmon dephasing time makes nanoantennas very promising systems for ultrafast phase investigation. I describe here the realization of two different experiments both based on the detection of second harmonic signal. In the first part of the chapter I show that the interaction of a resonant nanoantenna with a broadband laser field is influenced by the plasmonic resonance. The second harmonic generated from a nanoantenna can then be used to extract the complete resonant response. In the second part I propose and demonstrate the feasibility of a multicolor imaging technique that uses plasmonic nanoantennas as second harmonic labels.

This chapter is based on:

- **Accanto N**, Piatkowski L, Renger J, & van Hulst NF. *Capturing the optical phase response of nanoantennas by coherent second-harmonic microscopy*. Nano Lett. 14, 4078 (2014)
- **Accanto N**, Piatkowski L, Hancu IM, Renger J, & van Hulst NF. *Resonant plasmonic nanoparticles for multicolor second harmonic imaging*. Appl. Phys. Lett. 108, 083115 (2016)
- Piatkowski L, **Accanto N**, & van Hulst NF. *Ultrafast meets Ultrasmall: Controlling Nanoantennas and Molecules*. ACS Photon. Review (2016)

In the previous chapter, I showed that the use of non-resonant NPs of dimensions smaller than the diffraction limit enables full control of ultrashort laser pulses with high spatial resolution. The logical successive step is to apply the same nanoscale pulse-shaping scheme to NPs that do posses a resonant response at the laser wavelength. Plasmonic nanoantennas are the NPs of choice. Here I show that the SH from plasmonic nanoantennas, for sufficiently broad pulses in the frequency domain, is influenced by their resonant response. Performing MIIPS experiments on plasmonic nanoantennas therefore yields different results from those obtained on non-resonant NPs. This makes it possible to retrieve information on the plasmon resonance and to actively exploit the nanoantennas to create customized SH spectra in nanometric volumes.

3.1 Plasmonic nanoantennas

Plasmonic nanoantennas can be defined as metallic nanoparticles that efficiently convert propagating optical radiation into spatially confined fields and vice versa [83, 94–99]. Noble metals, like gold and silver, support surface plasmon polaritons at optical frequencies, which are electromagnetic excitations existing at the interface between a dielectric and a metal, arising from the coupling of the electromagnetic field to the free electrons in the metal [84]. Most plasmonic nanoantennas are based on metallic nanoparticles exhibiting localized surface plasmon resonances at visible and near infrared frequencies [83, 95].

A simple way of understanding the behavior of metallic nano-rods, which constitute the basic nanoantenna geometry used in this thesis, is to consider them as finite pieces of thin metallic nano-wires. Such structures support plasmonic modes that propagate along the wire axis [95, 96]. Due to the finite skin depth of metals in the visible regime, these guided modes have a shorter effective wavelength than the free space wavelength [95]. In a metallic nano-rod of dimensions close to a multiple of half the wavelength of the guided plasmonic mode, a resonant cavity mode builds up giving rise to a localized surface plasmon resonance (LSPR) [95, 100]. A metallic NP supporting LSPRs for wavelengths of the incoming light in the visible or near infrared spectral region is what I refer to as a plasmonic nanoantenna.

A key feature of plasmonic nanoantennas that makes them very attractive for applications is their capability of confining the resonant electromagnetic field in nanometer-sized spatial regions of high field intensity. This, for instance, allows nanoantennas to influence the light-matter interactions in a quantum emitter placed in their near field. Based on this concept, imaging of fluorescent molecules with sub-wavelength spatial resolution was demonstrated [97, 101–103] and nanoantennas were used to direct the fluorescence [104, 105] and to change the absorption and emission rate [106–108] of quantum emitters. The presence of LSPRs and the associated field enhancement at the nanoantenna position have been suggested for increasing the efficiency of solar cells [109]; to make accurate bio-sensors [80, 110–113] and to enhance nonlinear light matter interactions [72, 92, 114]. All these applications need tuning of the LSPRs in the nanoantenna to match the specific experimental requirements. Considering a plasmonic nanoantenna as a cavity for surface plasmons, one can intuitively understand that the dimensions of the cavity determine the wavelength at which the plasmon resonance occurs. A second relevant characteristic of plasmonic nanoantennas is their high wavelength tunability, obtainable by changing their size, shape or the material they are made of [84, 95]. Thanks to modern fabrication techniques, such as electron beam lithography and focused ion beam milling, nanostructures of the required design can be made with ~ 10 nm precision, which makes plasmonic nanoantennas a very versatile technology.

This chapter and Chap. 5 are dedicated to the investigation of a relevant yet largely unexplored property of plasmonic nanoantennas: the coherence of surface plasmons associated to LSPRs. In order to shed light onto this phenomenon, we experimentally studied nonlinear optical interactions, SHG in this chapter and TPA in Chap. 5, between resonant plasmonic nanoantennas and ultrashort phase-controlled laser pulses. Plasmon dephasing (or coherence) times in nanoantennas are extremely fast, in the range of few femtoseconds, which corresponds to broadband LSPRs in the frequency domain. Modern laser systems have recently demonstrated to posses the time resolution, and bandwidth, necessary to access this coherent regime [7, 8, 13, 37, 115–121]. Importantly, these works suggested that different nanoantennas characterized by different LSPRs, might be distinguished based on their coherent responses.

Here, I show that the SHG from plasmonic nanoantennas subject to broad-

band laser pulses can be used to determine their complete resonant response, both in phase and in amplitude. This is possible because the bandwidth of the laser pulse used in the experiment is larger than the spectral width of the LSPR in these systems. Due to the interaction of the laser with the LSPRs, the local field experienced by the nanoantennas is different from the field in free space. The SH from the nanoantennas directly carries the information about the local field, which can be determined from a phase shaping experiment (MIIPS) on the nanoantennas. As a consequence, by using broadband laser pulses, different nanoantennas can be distinguished based on their SH spectra. This unique effect can be exploited for multicolor SH imaging, which is difficult to achieve with standard (non-resonant) SH nanoparticles or with narrowband laser pulses.

3.2 The nanoantennas studied

The nanoantennas studied in this chapter were silver nano-rods fabricated using electron beam lithography on a glass coverslip coated with a 10 nm thin layer of indium tin oxide (ITO). Fig. 3.1 a,b show SEM images of the nanoantennas of two different design lengths. They had the shape of two attached nano-rods with silver disks at their ends. Because the two nano-rods were connected, the resonant mode that developed was that of a single nano-rod with length equal to the sum of the lengths of the two nano-rods that composed it. As mentioned above, given an electromagnetic field incident on a nano-rod at a certain free space wavelength, the guided plasmonic mode that originates has an effective wavelength λ_{eff} that is much shorter than the free space wavelength [96, 122]. With an incident field centered around 800 nm, the effective wavelength for the silver nano-rods studied here (Fig. 3.1) was around 300 nm, and they were hence resonant with the $3\lambda_{\text{eff}}/2$ mode.

The particular design of the silver nanoantennas was chosen to produce narrow LSPRs in the frequency domain, and high SH efficiency. This can be understood as follows: higher order modes, as the $3\lambda_{\text{eff}}/2$ one, in general couple less strongly to the electric field, and therefore produce lower nonlinear signals, than the fundamental $\lambda_{\text{eff}}/2$ mode, but have the great advantage of presenting narrower resonances, especially in the case of silver, which posses lower ohmic damping compared to gold [123]. To compensate for the lower

nonlinear signals, the silver disks at the end of the nano-rods produced a high field gradient that enhanced the bulk contribution to the SHG [74]. A detailed description of these structures and their nonlinear interaction with ultrafast lasers may be found in [124].

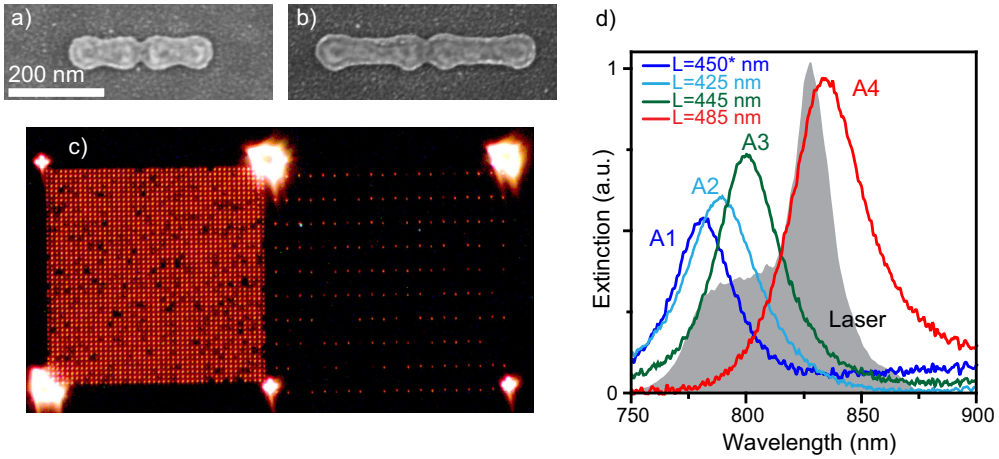

Fig. 3.1: a,b) Typical SEM images of the silver nanoantennas used. c) Dark field image showing a denser array (left side) next to a sparser array (right side) of nanoantennas. d) Extinction images of four dense arrays of nanoantennas (labeled A1-A4) together with the laser spectrum used in the experiment.

The nanoantennas were arranged in arrays. One array contained many nanoantennas of the same design length. The nanoantenna length (and hence the associated LSPR) was changed for different arrays. Fig. 3.1 c shows a dark field image of an array of nanoantennas of the same design length, composed by densely and sparsely packed nanoantennas. The denser area was used to measure the extinction spectra showed in Fig. 3.1 d that were taken on ensembles of nanoantennas. The SH measurements shown throughout this chapter were instead recorded on single nanoantennas, acquired in the sparser area to ensure that only one nanoantenna was present in the focus of the objective. The total length of the nanoantennas was changed from 425 nm to 485 nm. Fig. 3.1 d illustrates that, changing the length of the nanoantennas, we were able to tune their LSPRs across the 100 nm wide laser spectrum. In the case of the 450 nm nanoantennas, labeled A1 in Fig. 3.1d, a different design was used (these nanoantennas were slightly wider than the others). This explains why the resonance position corresponding to the A1 nanoantennas peaks at

shorter wavelengths with respect to the A2 ones. Importantly, the spectral width of the LSPRs shown in Fig. 3.1 d are narrower or comparable to that of the laser spectrum used in the experiment. This is equivalent of saying that the dephasing time of the surface plasmons is comparable or longer than the laser pulse at its Fourier limit. Under these conditions, it is possible to study and actively exploit the full LSPR response, as described in this chapter.

3.3 The measurement of the plasmon resonance

In order to precisely measure their LSPRs, we studied the SH generated by the plasmonic nanoantennas. Chap. 2 showed that even metallic nanoparticles, despite their centrosymmetric nature, can produce SH. In that experiment, in order to avoid intrinsic responses from the NPs, we used non-resonant gold NPs to test the ultrafast laser pulse on a nanometer spatial scale. Here instead the complementary experiment is described: SH from resonant silver nanoantennas was detected and compared to that originating from non-resonant materials in order to extract information about the LSPRs.

Following the formalism of Chap. 1, I consider the laser field in the frequency domain $E(\omega) = E_0(\omega)e^{-i\varphi(\omega)}$. In a very simple model, the interaction with a resonant nanoantenna results in a change of the amplitude and phase of the local electromagnetic field. I call the amplitude and phase contribution from the nanoantenna $A(\omega)$ and $\varphi_A(\omega)$ respectively. The new local field that is present in the proximity of the nanoantenna is:

$$\begin{aligned} E_A(\omega) &= E_0(\omega)\,A(\omega)\,e^{-i[\varphi(\omega)+\varphi_A(\omega)]} \\ &= E_{\text{tot}}(\omega)\,e^{-i\varphi_{\text{tot}}(\omega)} \end{aligned} \tag{3.1}$$

Using Eq. (1.9), the SH at the frequency 2ω can be written in the form:

$$SH(2\omega) = \left| \int |E_{\text{tot}}(\omega+\Omega)|\,|E_{\text{tot}}(\omega-\Omega)|\,e^{i[\varphi_{\text{tot}}(\omega+\Omega)+\varphi_{\text{tot}}(\omega-\Omega)]}\,d\Omega \right|^2 \tag{3.2}$$

The SH from resonant nanoantennas therefore contains information on the amplitude $A(\omega)$ and the phase $\varphi_A(\omega)$ of the LSPR.

3.3.1 Visualizing the resonant response

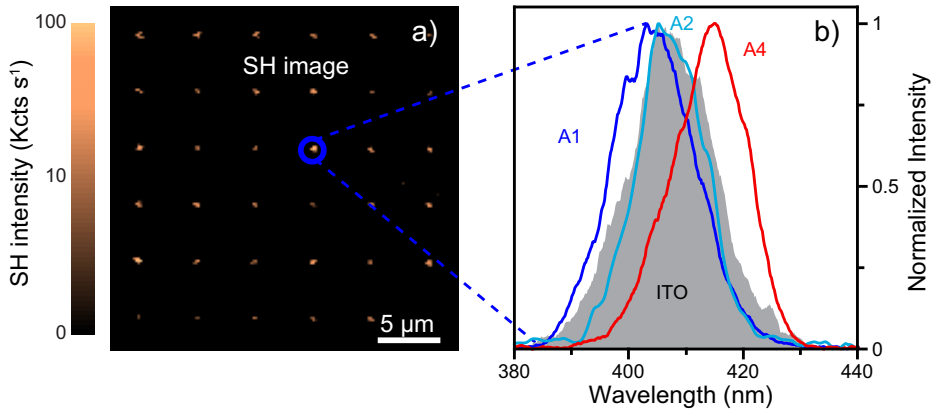

Fig. 3.2: a) SH image of an array of nanoantennas. b) SH spectra corresponding to single nanoantennas of different arrays. The grey shaded curve corresponds to SH spectrum from the reference ITO.

At the beginning of each experiment, SH images of a nanoantenna array were acquired, as shown in Fig. 3.2 a. Every bright spot in this image is due to the SH of an individual nanoantenna. The power used to excite SH from single nanoantennas was $\sim 50\,\mu$W in a diffraction limited spot. At this power there was no background SH from the rest of the sample. However, increasing the incident power to 10 mW, allowed the detection of SH from the thin ITO layer on which the nanoantennas were deposited. ITO is a good reference material as it does not present resonances either at the fundamental or SH frequency [125]. We therefore compared the SH from resonant nanoantennas to that measured on ITO in order to retrieve their LSPRs.

Fig. 3.2 b shows the normalized SH spectra for three different nanoantennas, having different LSPRs (from arrays A1, A2 and A4 of Fig. 3.1 b), and compares them to the SH spectrum measured on the reference ITO. These spectra were acquired using a FL laser pulse. The SH spectra from the single nanoantennas exhibited spectral shifts from shorter (blue) to longer wavelengths (red) going from the A1 to the A4 array, closely following the trend observed in the ensemble extinction spectra. From this plot one can already deduce that the LSPRs changed the SH spectrum and that with our setup we were able to resolve this change.

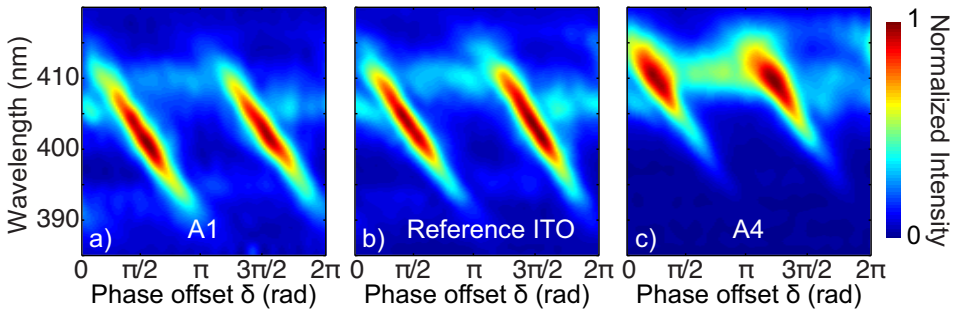

Fig. 3.3: MIPS traces taken on: a) a single nanoantenna from the A1 array; b) the reference ITO; c) a single nanoantenna from the A4 array.

We next performed MIIPS experiments on individual nanoantennas and compared them to ITO. Fig. 3.3 shows three normalized MIIPS traces acquired on a single nanoantenna from the A1 array (a), on the reference ITO (b) and on a single nanoantenna from the A4 array (c). In what follows, I will simply call the two single nanoantennas A1 and A4, as indicated in Fig. 3.3. The main difference between the three traces is a wavelength shift, corresponding to a shift of the SH spectrum. Compared to the MIIPS trace on ITO, the one on A1 is slightly shifted towards lower wavelengths, whereas the one corresponding to A4 shows a large spectral shift towards higher wavelengths. This is the same effect already noticed in the SH spectra of Fig. 3.2 b and can be assigned to the amplitude component $A(\omega)$ of the LSPR response, which enhanced the portion of the laser spectrum that overlapped with the resonance. However, a resonance introduces a phase response as well [95]. In a simple Lorentzian response model, the phase of the resonator undergoes a smooth change of π radians as a function of frequency. In this model, the phase $\varphi_A(\omega)$ should therefore vary by π across the full LSPR, which has a width comparable to that of the laser field. In other words a very small change of phase is expected to occur in the spectral region of the laser pulse, which requires a very sensitive phase measurement.

To visualize this phase effect, Fig. 3.4 shows the difference between the MIIPS traces acquired on nanoantennas and ITO, for the A1-ITO and A4-ITO case respectively. The color scale is chosen such that the red features correspond to areas in which the normalized intensity from the nanoantennas was greater than the ITO, and the opposite is true for the blue features. These

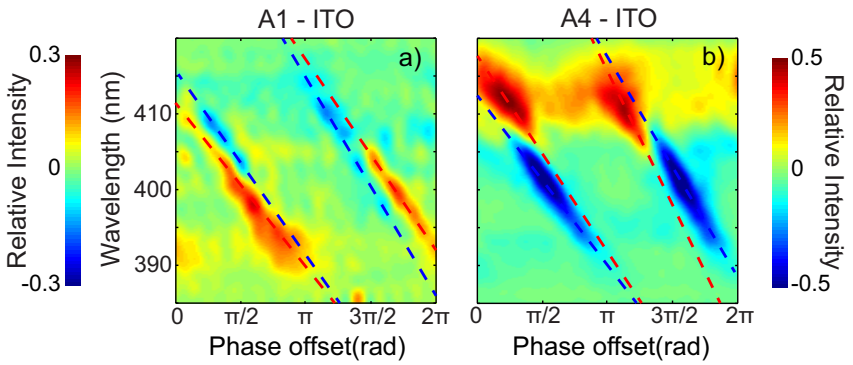

Fig. 3.4: a) Difference of the MIPS trace taken on the A1 nanoantenna and ITO. b) Difference of the MIPS trace taken on the A4 nanoantenna and ITO. The dashed lines are guides to the eye highlighting the difference between the first and second period of the traces, caused by the phase response of the nanoantennas.

traces highlight that the main effect of the nanoantennas with different LSPRs was to produce a wavelength shift on the MIIPS traces, which is an amplitude effect. Recalling the discussion of Sec. 1.4, it is useful to think of a MIIPS trace as being formed by two different periods: the 0 to π and the π to 2π period. In the case of a FL pulse, these periods are completely equivalent and they become different as phase distortions are added to the pulse. The difference between the first and the second period is visible in the spectrograms of Fig. 3.4 as a different tilt of the red features with respect to the blue ones, as the dashed lines highlight. These small but clear differences are the evidence of the phase response associated with the LSPR.

3.3.2 The fitting procedure

Eq. (1.11) describes how the SH spectrum changes as a function of the phase offset δ in a MIIPS trace. Substituting in that formula $E_0(\omega)$ for $E_0(\omega)A(\omega)$ and $\varphi(\omega)$ for $\varphi(\omega)+\varphi_A(\omega)$, one can fit the two-dimensional MIIPS traces obtained on resonant nanoantennas to retrieve the functions $A(\omega)$ and $\varphi_A(\omega)$. The term $S(\omega)=|E_0(\omega)|^2$ is the laser spectrum and is therefore a known quantity, whereas $\varphi(\omega)$, which corresponds to the small deviations from FL pulses (the pulse was always compressed before every nanoantenna measurement), can be obtained from a fit of the ITO traces. The retrieved residual spectral

phase $\varphi(\omega)$ can then be used in the fit of the nanoantenna trace, from which the quantities $A(\omega)$ and $\varphi_{\mathrm{A}}(\omega)$ are determined.

Two different models were used to fit the nanoantenna traces: the first model assumes general sixth order polynomial functions for both the amplitude response $A(\omega)$ and the intrinsic nanoantenna phase $\varphi_{\mathrm{A}}(\omega)$. This model does not require any a priori knowledge of the resonance under study, and hence could be used to fit any unknown resonance. Referring to the discussion of Sec. 1.3, expanding the spectral phase in a Taylor series (as in Eq. (1.4)), the zeroth order phase term corresponds to the phase of the carrier wave with respect to the pulse envelope, which practically does not change the electric field for a many cycle pulse. The linear term in the expansion instead, is responsible for a change of the absolute arrival time of the pulse, which plays no role in the SHG process. In the fit with the polynomial model, both the zeroth and the first order phase terms were fixed to zero. In this sense the polynomial model should be used as a fitting procedure to retrieve the nonlinear part of the spectral phase. The second model assumes that the LSPRs of the silver nanoantennas are Lorenztian functions, where the only free parameters for the fit are the central position ω_0 and the width Δ of the resonance. This model is the simplest one to describe a resonance as it makes the assumption that localized surface plasmons can be considered as damped harmonic oscillators [5, 37, 84, 95]. Given the shape of the extinction curves shown in Fig. 3.1 b, one can expect this model to be a good approximation of the LSPRs. In the case of the Lorentzian model the following functions were used:

$$A(\omega) = L(\omega) = \left[\frac{1}{(\omega - \omega_0)^2 + \Delta^2} \right]^{1/2} \tag{3.3}$$

$$\varphi_{\mathrm{A}}(\omega) = \varphi_{\mathrm{L}}(\omega) = \arctan\left[\frac{(\omega - \omega_0)}{\Delta} \right] \tag{3.4}$$

Fig. 3.5 compares the difference of the measured MIIPS traces A4-ITO (b) already shown in Fig. 3.4 b with the difference of the fitted traces for A4 and ITO using the polynomial model without considering the phase response of the nanoantenna, i.e. assuming $\varphi_{\mathrm{A}}(\omega) = 0$ in the fit procedure (a), and including the phase response (c). A comparison between the three images shows that the main effect of the nanoantenna, i.e. the wavelength shift of the SH

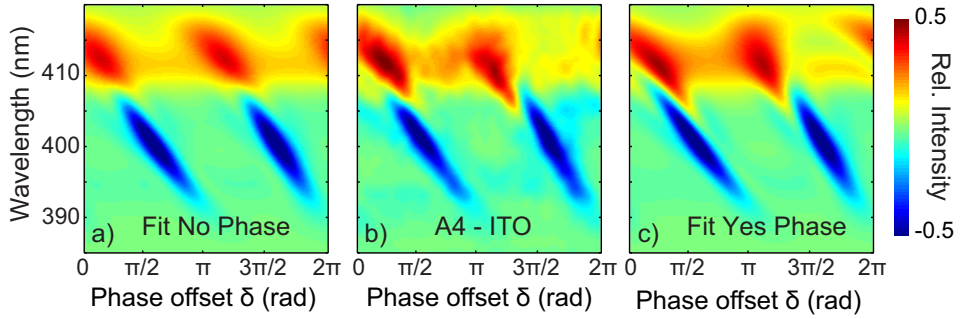

Fig. 3.5: a) Difference of the fitted traces for A4 and ITO using the polynomial model with $\varphi_A(\omega) = 0$. b) Measured MIIPS trace difference A4-ITO. c) Difference of the fitted traces for A4 and ITO using the polynomial model taking into account the phase response of the nanoantenna

spectrum, can be reproduced even when the nanoantenna phase is not considered (Fig. 3.5 a), which strongly suggests that it is an amplitude effect. However, the asymmetry between the first and the second period of the MIIPS trace is a pure phase effect, which cannot be reproduced without considering the phase response of the nanoantennas. The introduction of the nanoantenna phase produces a better fit of the experimental data, and all the major features in the MIIPS trace can be well reproduced. Also in the case of the fit with the Lorentzian model the phase component is necessary to better reproduce the data.

The graphs of Fig. 3.6 present the results of the fits with the polynomial model as well as the Lorentzian model for the case of A4. A comparison between the black dashed curves, which correspond to the original laser spectrum $|E_0(\omega)|^2$, and the grey colored regions, representing the squared of the local field (i.e. the term $|E_0(\omega)A(\omega)|^2$ for the polynomial model and the term $|E_0(\omega)L(\omega)|^2$ for the Lorentzian model), suggests that the effect of A4 indeed was to modify the amplitude of the electric field shifting it to the red, in agreement with the extinction measurements of Fig. 3.1 b. Both the models yielded very similar results for the amplitude component of the resonance. The nonlinear part of the spectral phases (the zeroth order and first order term were fixed at zero in the fits) for ITO and A4, as retrieved from the polynomial fit ($\varphi(\omega)$ and $\varphi_A(\omega)$ in Fig. 3.6 a) are found to differ from each other especially for longer wavelengths, i.e. in the spectral region of the LSPR. This phase response

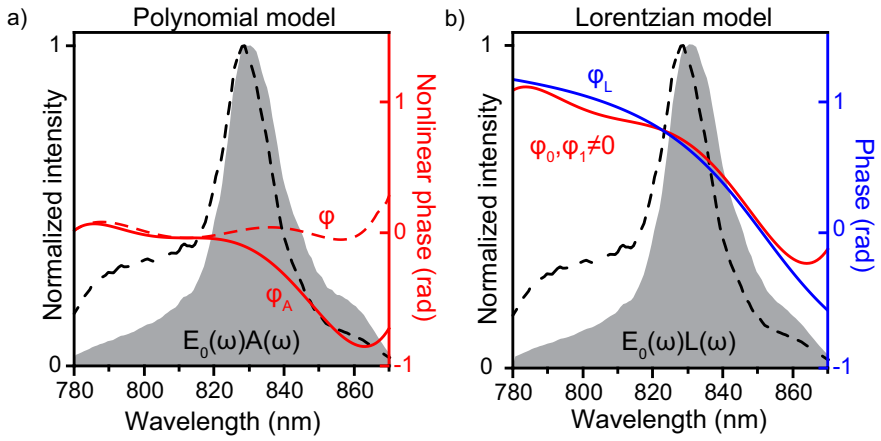

Fig. 3.6: a) Fit results of the MIIPS trace for A4 using the polynomial model. Original laser spectrum $|E_0(\omega)|^2$ (dashed black curve) and reference phase $\varphi(\omega)$ (dashed red curve) resulting from a fit of the ITO MIIPS trace. The gray colored region is the modified spectrum $|E_0(\omega)A(\omega)|^2$ and the red solid curve is the nanoantenna phase $\varphi_A(\omega)$ retrieved from the fit. b) Fit results of the MIIPS trace for A4 using the Lorentzian model. The dashed black curve is the original laser spectrum $|E_0(\omega)|^2$. The gray colored region is the modified spectrum $|E_0(\omega)L(\omega)|^2$ and the blue solid curve is the spectral phase $\varphi_L(\omega)$ retrieved from the fit. The red curve represents the phase obtained from the polynomial fit including the terms φ_0 and φ_1.

has a simple interpretation in the time domain if one takes into account that a phase slope in the frequency domain corresponds to a delay in the time domain. The initial FL pulse ($\varphi(\omega) \sim 0$) was distorted by the interaction with the resonant nanoantenna, and it became longer than the Fourier limit. In particular, the long wavelength side of the incident field experienced a time delay with respect to the short wavelength side, which is due to the presence of the LSPR.

The Lorentzian phase $\varphi_L(\omega)$, plotted as a solid blue line in Fig. 3.6 b, differs from the phase obtained with the polynomial fit. However, a Taylor expansion of the Lorentzian phase function in Eq. (3.4), generally produces nonvanishing zeroth and first order terms, whereas these terms were fixed to zero in the polynomial fit. The difference between $\varphi_A(\omega)$ and $\varphi_L(\omega)$ is mainly due to a difference in these terms, that do not carry relevant information. This can be verified by adding a nonzero φ_0 and φ_1 to the phase previously retrieved using the polynomial fit. The resulting phase is plotted as a red line in Fig. 3.6 b and it

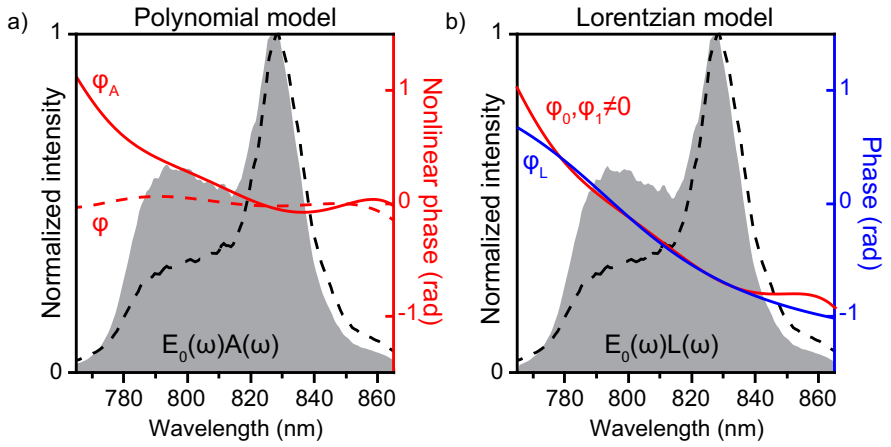

Fig. 3.7: a) Fit results of the MIIPS trace for A1 using the polynomial model. Original laser spectrum $|E_0(\omega)|^2$ (dashed black curve) and reference phase $\varphi(\omega)$ (dashed red curve) resulting from a fit of the ITO MIIPS trace. The gray colored region is the modified spectrum $|E_0(\omega)A(\omega)|^2$ and the red solid curve is the nanoantenna phase $\varphi_A(\omega)$ retrieved from the fit. b) Fit results of the MIIPS trace for A1 using the Lorentzian model. The dashed black curve is the original laser spectrum $|E_0(\omega)|^2$. The gray colored region is the modified spectrum $|E_0(\omega)L(\omega)|^2$ and the blue solid curve is the spectral phase $\varphi_L(\omega)$ retrieved from the fit. The red curve represents the phase obtained from the polynomial fit including the terms φ_0 and φ_1.

is found to overlap well with the Lorentzian phase. This strongly suggests that the two models are equally good in describing the response of nanoantennas and further justifies the use of the polynomial model as a general fit model that could be used to analyze any unknown response from arbitrary resonant nano-structures. In Fig. 3.7 the fit results for A1 are presented, for which the same concepts discussed for A4 apply.

In summary, plasmonic nanoantennas interact with the incoming electromagnetic field, creating a local field in the proximity of the nanoantennas that depends both on the incident field and on the LSPRs. The SH generated at the nanoantennas is directly related to the local field and can thus be used to obtain information about the LSPRs. A great advantage of detecting SH is that the measurement is background free, i.e. only photons that interacted with the nanoantennas generate SH. In contrast, in a measurement where the fundamental field scattered by the nanoantennas is detected, great care should

be taken in eliminating the contribution from those photons that did not interact with the nanoantennas. In order to measure the complete, wavelength dependent resonant response of different nanoantennas, laser pulses with a frequency bandwidth larger than the width of the LSPRs have to be used. Applying the same pulse shaping technique described in Chap. 2, we successfully measured both the amplitude and the very small phase response associated to the LSPRs.

3.4 Nanoantennas for multicolor second harmonic imaging

Not only can the SH from plasmonic nanoantennas be used to measure their respective LSPRs, but it also has possible implications in the field of multiphoton microscopy. SH nanoparticles may be used as an alternative to common fluorescent markers, owing to their superior photo-stability and the possibility of using two-photon excitation [63, 67, 69]. However, the SH spectrum of non-resonant NPs is mainly determined by the laser field (both in its phase and amplitude component) and does not change for different NPs. This is in contrast to other widely used fluorescent markers, like quantum dots, which emit at different wavelengths according to their sizes and materials, even when excited with the same laser source. This allows researchers to label different targets using different QDs, excite them all at once, and distinguish them with spectrally resolved detection, which is called multicolor fluorescence imaging [126, 127]. Multicolor imaging has so far been limited to fluorescent markers and not studied for SH NPs.

In the previous Section I showed that, because the SH spectrum from plasmonic nanoantennas depend on their LSPR, different nanoantennas produce different SH spectra (Fig. 3.2). The phase shaping capability gives an additional degree of freedom to create customized SH spectra on the nanoscale (see Chap. 2). Combining these two features, I demonstrate here that by using two nanoantennas characterized by detuned LSPRs and precise phase shaping, it is possible to obtain contrast in the SH between the two nanoantennas, and to produce different colors in their SH spectra, which is at the basis of multicolor SH imaging. The biocompatibility of metallic NPs [81] together with the versatility in the fabrication processes, make the results presented

here relevant for biological applications.

3.4.1 Intensity contrast

I first discuss the possibility of achieving contrast in the total SH intensity by using phase shaping. These results might provide a useful tool to distinguish two different nanoantennas when spectrally resolved detection is not available. It was shown previously [69] that contrast in the SH intensity can be obtained between different materials ($BaTiO_3$ and SiC) by changing the wavelength of a relatively narrowband laser from 800 to 880 nm, as a consequence of different conversion efficiencies of the materials at the two wavelengths. However, such contrast mechanism requires two different lasers to be aligned in exactly the same way in an optical microscope, which is a difficult operation. A change in the spectral phase of a broadband laser pulse is a simpler way to obtain contrast in the SH intensity.

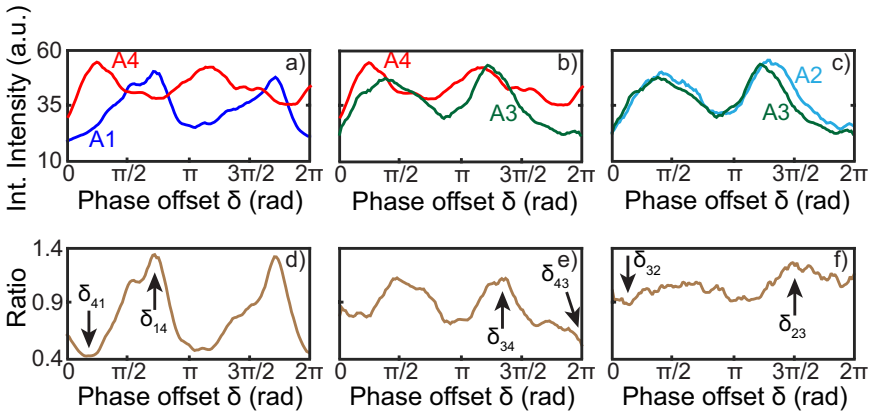

Fig. 3.8: a,b,c) Spectrally integrated MIIPS traces of the indicated nanoantenna pairs. The vertical axis is the same for the three graphs. d,e,f) Ratio of the spectrally integrated SH intensity between A1/A4, A3/A4 and A2/A3 respectively as a function of the phase offset δ. The vertical axis is the same for the three graphs. The arrows represent for each graph the points at which maximum and minimum ratio occur. The corresponding δ values generate maximum contrast between the two nanoantennas.

Fig. 3.8 a-c show spectrally integrated MIIPS traces for four different nanoantennas, which were obtained from MIIPS traces similar to those shown in Fig. 3.3 upon integration over the wavelength axis. In every graph a pair of

traces measured on nanoantennas of different lengths is plotted to highlight their differences. SH maxima and minima, for different nanoantennas, were obtained at different δ values in a MIIPS scan, i.e. upon application of different spectral phases by the SLM. Because A1 and A4 were resonant on the opposite side of the laser spectrum (see extinction curves in Fig. 3.1), the corresponding integrated MIIPS traces in Fig. 3.8 a are maximally shifted. The relative shift is reduced for the traces corresponding to A3 and A4 (Fig. 3.8 b) and is almost zero for the traces of A2 and A3 (Fig. 3.8 c), which, according to the extinction measurements, had almost overlapping LSPRs.

In Fig. 3.8 d-f the ratio of the spectrally integrated MIIPS traces between A1/A4, A3/A4 and A2/A3 is plotted. From these graphs it is possible to deduce that the ratio between the SH signals in the experiment oscillated between ~ 0.4 and ~ 1.3 for A1-A4, between ~ 0.6 and ~ 1.1 for A3-A4 and was almost constant for A2-A3 as a function of δ. As indicated in Fig. 3.8 d-f, δ_{14} and δ_{41} respectively represent the δ values at which the ratio A1/A4 was the largest (so that A1 was brighter than A4) or the smallest (A4 was brighter than A1). The same rule applies for the other pairs; for instance, at the value δ_{34}, A3 was brighter than A4 and at δ_{23} A2 was brighter than A3. The application of the spectral phases corresponding to δ_{14} and δ_{41}, or the analogous δ values for different nanoantenna pairs, generated the highest SH contrast in the nanoantennas. The available contrast was larger for more spectrally separated LSPRs. Calling A1(δ_{14}) the total SH intensity from A1 for the phase δ_{14}, the contrast between A1 and A4 for the phases δ_{14} and δ_{41} is defined as:

$$\frac{\mathrm{A1}(\delta_{14})}{\mathrm{A4}(\delta_{14})}\frac{\mathrm{A4}(\delta_{41})}{\mathrm{A1}(\delta_{41})} \tag{3.5}$$

The contrast for other nanoantennas is defined analogously. In the case of the A1-A4 pair the maximum contrast reached a factor of ~ 3; a factor of ~ 2 for the A3-A4 pair and negligible contrast could be obtained for A2-A3. These results demonstrate that plasmonic nanoantennas of different lengths can be used to obtain contrast in the SH by applying different spectral phases. As only the phase of the laser field (and not the amplitude) was changed, this result can be ascribed to a coherent effect, stemming from the relatively narrow (narrower than the laser spectrum) LSPRs in these systems. However, to exploit this contrast for imaging purposes, two actions are still required, namely the acquisition of two different images of the sample, one for each spectral phase.

The rest of the chapter shows that, once having two nanoantennas that differ enough in their LSPRs, the best way of obtaining contrast is to exploit the different SH spectra generated by the nanoantennas together with spectrally resolved detection.

3.4.2 Spectral contrast

The graphs in Fig. 3.9 a-c show SH spectra recorded during the MIIPS experiments on different pairs of nanoantennas for the indicated δ values. The dashed black line separates the spectral range in a blue ($\lambda < 408\,\text{nm}$) and a red ($\lambda > 413\,\text{nm}$) spectral region. The chosen δ values correspond to the phases that maximized the spectral contrast between the nanoantenna pairs in the two spectral regions. The SH spectra in the graph corresponding to the pair A1-A4, peak on the opposite sides of the SH range and the spectral difference is lower in the graphs corresponding to A3-A4 and A2-A3 pairs. By spectrally splitting the detection and sending the blue region of the SH to one detector (called blue detector) and the red region to a second detector (red detector), multicolor SH imaging should becomes possible. To demonstrate this concept, in Fig. 3.9 d-f calculations of the hypothetical spatial images that one would obtain on the two detectors are reported. The red and blue spots in the images represent the SH from the nanoantennas as the red and the blue detectors would measure. The spatially integrated intensity of the spots are equal to to the spectrally integrated SH spectra of Fig. 3.9 a-c in the corresponding spectral window. In the case of the A1-A4 pair, using spectrally resolved detection, the blue detector would mainly be sensitive to the SH from A1 whereas the red one would mainly detect the SH from A4. Calling A1_{blue} and A1_{red} the total SH intensity from A1 in the blue and red spectral windows respectively, it is possible to define the spectral contrast between A1 and A4 (and for the other pairs) in the two different detectors as:

$$\frac{\text{A1}_{\text{blue}}}{\text{A4}_{\text{blue}}}\frac{\text{A4}_{\text{red}}}{\text{A1}_{\text{red}}} \tag{3.6}$$

Based on the SH spectra of Fig. 3.9, the pair A1-A4 produced a spectrally resolved contrast of a factor of ~ 50, the pair A2-A4 a factor of ~ 6, and almost no contrast was generated by the pair A2-A3.

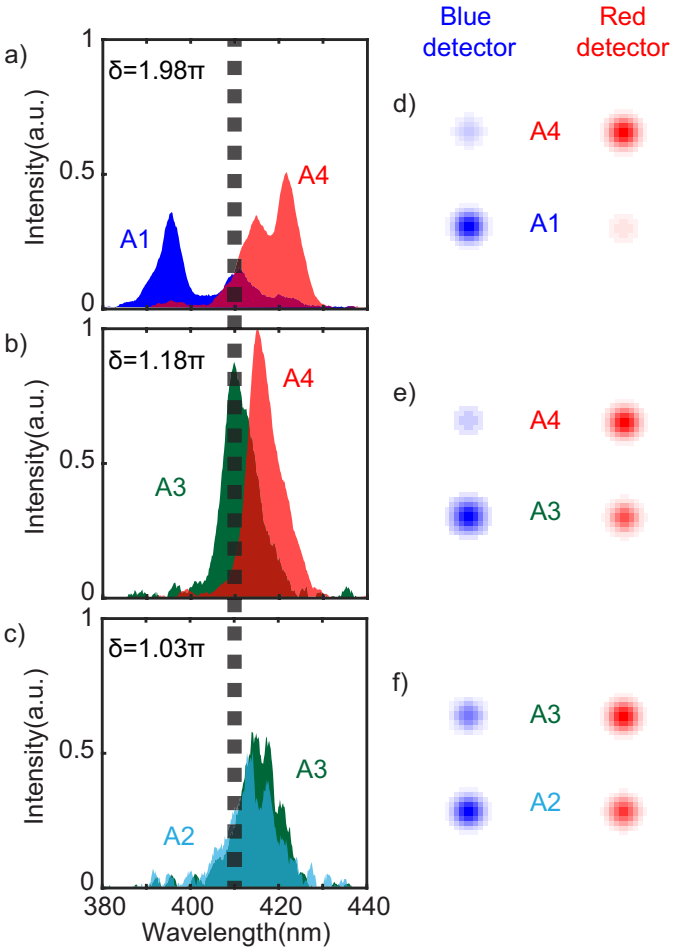

Fig. 3.9: Multicolor second harmonic spectra. The SH detection is split at 410 nm (black dashed line). a,b,c) SH spectra for the indicated nanoantennas that maximize the contrast between the blue ($\lambda < 408$ nm) and red ($\lambda > 413$ nm) side of the SH range. d,e,f) The blue and red dots are illustrations of how the different nanoantennas would appear on spectrally selective two-dimensional images.

3.4.3 Demonstration of multicolor imaging

The above analysis suggests that by using suitable nanoantennas in combination with the appropriate laser spectral phase, different colors in the SH spectra can be obtained. The possibility of multicolor second harmonic imag-

ing is thus demonstrated. However, the nanoantennas considered so far, i.e. ~ 400 nm silver nanoantennas (Fig. 3.1), were too large to be used as real biological labels. In order to prove the usefulness of this proposal, smaller NPs, closer to real experimental conditions in biological imaging, should be investigated. We therefore prepared a different sample of plasmonic nanoantennas and repeated the experiment.

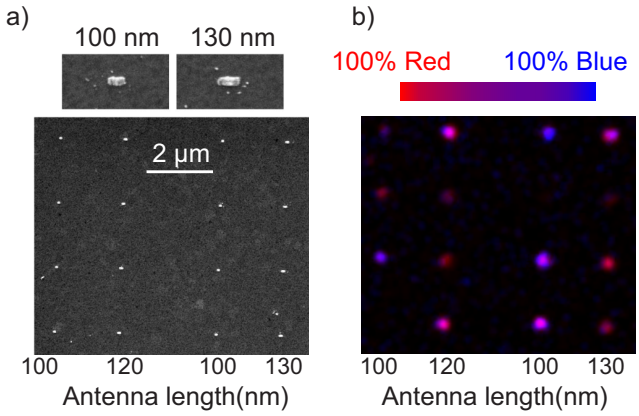

Fig. 3.10: Multicolor second harmonic imaging. a) SEM images of an array of gold nanoantennas of different lengths and higher resolution SEM images of the individual 100 nm and 130 nm nanoantennas. d) Two-color SH image of the same array acquired in one scan, showing contrast between different species, with longer nanoantennas more red. The blue ($\lambda < 400$ nm) and red ($400 < \lambda < 420$ nm) side of the SH-spectrum are pseudo-colored blue and red.

The sample consisted of gold nano-rods of length varying between 90 nm and 130 nm. Even though silver is generally considered to be a good plasmonic material at optical wavelengths, its propensity to oxidize, compared to gold, makes it a difficult material to work with. For multicolor SH imaging gold nanoantennas seem a more suitable solution. In order to have smaller nanoantennas but still in resonance with the laser field, the gold nano-rods were fabricated to be resonant with the $\lambda_{\text{eff}}/2$ mode. As shown in the SEM images of Fig. 3.10 a, in the same array, columns of 100 nm alternated with columns of 120 nm and 130 nm gold nanoantennas. The 100 nm ones were resonant with the blue side of the laser spectrum and the resonance shifted to the red for longer nanoantennas. In this way nanoantennas with different LSPRs were close to each other and could be readily imaged in a single scan.

For the multicolor imaging purpose, the array shown in Fig. 3.10 a was imaged with two different APDs simultaneously. With a dichroic mirror and additional spectral filters, the blue part of the SH light ($\lambda < 400$ nm) was sent to one APD and the red part to the other ($400 < \lambda < 420$ nm). Representing the image collected by the blue (red) APD with a blue (red) pseudo color-scale and overlaying the two images, the false color image of Fig. 3.10 b was obtained. In this image good contrast is apparent between the 100 nm nanoantenna and the 120 nm and 130 nm, due to the difference in the LSPRs. The 100 nm NPs appear blue to violet in the image, while the 120 and 130 nm NPs are purple to red.

Fig. 3.10 is a strong indication that the multicolor SH imaging technique proposed in this section is possible, even by using smaller (~ 100 nm) nanoantennas. However, there are also several limitations that need to be discussed. (i) The sample used was not fully optimized for the experiment. The shape and size of the silver nanoantennas used in the first part of this chapter were designed to produce the narrowest resonances at the laser wavelength and generate high SH signal. In contrast, the LSPRs associated to the gold nanorods (see simulations in Chap. 5) were spectrally broader and the contrast was therefore smaller than the one shown in Fig. 3.9 a. By exploiting the flexibility in the fabrication together with the understanding of plasmonic effects, better suited samples will be designed in the future. (ii) In Fig. 3.10 b it is also apparent that some nanoantennas did not completely follow the trend of the others or produced lower SH intensity. This differences can be attributed to variations in the fabrication of the nanoantennas. (iii) The APDs used for acquiring the images had very low efficiency ($< 6\%$) for $\lambda < 400$ nm. Long integration times (20 ms) for each pixel in the image ($4 \cdot 10^4$ pixels) were needed. The scan of Fig. 3.10 b thus took around 13 minutes. Despite this long integration times, the images acquired by the blue APD were still quite noisy, which causes the higher blue than red background in Fig. 3.10 b. The use of detectors with higher efficiency at the SH wavelength would be very beneficial.

There are therefore several ways of improving the multicolor SH imaging technique. However, despite all these difficulties, different colors in the image of Fig. 3.10 b are already visible. If correctly improved, this technique might become a useful alternative to standard multicolor imaging based on fluorescent markers.

3.5 Conclusions

In this chapter I have shown that resonant plasmonic nanoantennas affect an incident laser field, according to the spectral position of their LSPRs. By using an ultrafast phase-controlled laser pulse, calibrated in accordance to the findings of Chap. 2, the LSPRs can be captured and actively used. I have demonstrated that both the amplitude and the very small phase component of the resonance can be accurately measured using MIIPS. This method was used in simple silver nano-rods, but can easily be generalized to arbitrary nanostructures. I have then shown that the properties of nanoantennas to produce different SH spectra, in combination with the phase shaping ability, can be used to obtain different colors in the SH spectra from different nanoantennas. This has the potential to be applied for real multicolor SH imaging. I have shown in this chapter the realization of a first experiment demonstrating this concept. Importantly, this kind of spectral contrast can only be obtained by using broadband laser pulses, with a bandwidth larger than the LSPRs, while the use of narrowband pulses of different wavelengths would not generate spectral contrast between different nanoantennas. In order to push this contrast further, even broader laser spectra, or narrower LSPRs would be beneficial.

CHAPTER 4

Closed loop control of single emitters

In this chapter I discuss our achievements in the active control of nonlinear processes in single nanoparticles. The goal is to develop a reliable closed loop coherent control scheme capable of addressing single quantum emitters at the nanoscale. To demonstrate this we used single semiconductor quantum dots as nanoscale quantum emitters and a novel optimization algorithm that is robust to noise and converges in a reduced amount of steps, even when operating at the few photon level. For the QDs used, precise theoretical predictions regarding their nonlinear absorption can be made, and the outcome of the closed loop control experiment can be verified against a theoretical model. By considering the signal generated by a single quantum dot and taking into account the speed of the optimization loop, the results described here suggest that this closed loop scheme could be extended to the study of single molecules at room temperature.

This chapter is based on:

- **Accanto N**, de Roque P, Galvan-Sosa M, Christodoulou S, Moreels I, & van Hulst NF. *Rapid and robust optimal control of single quantum dots.* Submitted (2016)

In the previous chapters I demonstrated our ability to observe single nano-systems with ultrafast time resolution and high phase sensitivity. This ability made it possible to visualize coherent responses in plasmonic nanoantennas. The ultimate goal of this thesis is, however, not only to observe but to actively manipulate the evolution of a single nano-system using precisely tailored optical fields. Starting from the 1980s, researchers in the field of coherent control have developed numerous control schemes to manipulate light-matter interactions [24, 25, 27, 128, 129]. Here the objective is to extend the closed loop control scheme [130], so far limited to the study of ensembles, to individual nano-emitters.

The method to study phase effects in nanoantennas used in Chap. 3 was first tested in Chap. 2 with a proof of principle experiment on systems with no intrinsic resonant responses. Analogously, here I introduce our closed loop coherent control scheme and describe a test experiment on single semiconductor QDs characterized by high TPA cross sections and broadband absorption. Using a novel maximization algorithm, closed loop optimization of the TPPL from a single QD was achieved, which constitutes an example of a simple coherent control experiment. Because the nonlinear interaction in these systems is well theoretically understood, the experimental solution can be compared to theoretical expectations. Based on the amount of signal generated by the QDs and the number of iterations needed for convergence, the analysis presented in this chapter suggests that this method is suitable for more experimentally challenging closed loop coherent control experiments in single nano-systems, as the one described in the next chapter on plasmonic nanoantennas.

4.1 Control of single emitters, a great experimental challenge

Coherent control can be defined as the process of steering the quantum evolution of a system to the desired outcome by applying tailored electromagnetic fields that exploit the coherence properties of the excitation fields and/or the system under study [24–27, 128, 129]. Since its introduction, different control schemes have been proposed and experiments have demonstrated control of different processes [4, 21–23, 86, 130–148]. A common experimental imple-

mentation of coherent control makes use of broadband phase-controlled laser pulses to induce interference in the system under study. By inducing constructive interference between the pathways that connect the initial state to the desired final state and destructive interference among the pathways leading to unwanted final states, the system is actively steered towards the desired target [24–26, 129].

The main conceptual difficulty in a coherent control experiment is to determine the ideal laser field for the specific system under study. Two main paradigms can be adopted to solve this problem. In the first one researchers assume a certain Hamiltonian for the system and calculate the laser field that leads to the desired final state [21, 140], which is then synthesized and experimentally applied to test the validity of the Hamiltonian used. The main advantage of this method is that ideally, once the laser field has been calculated and properly synthesized, only few measurements are needed to demonstrate the control. On the other hand the applicability of this approach is hampered by the complexity of real systems for which the Hamiltonian is only approximately known and complete calculations are unrealistic. For this reason often simpler and more intuitive electric fields are applied, which might still lead to some level of control but are not necessarily the best suited ones to solve the targeted problem [19]. The alternative approach is the closed loop control scheme, first introduced by Judson and Rabitz [130] in 1992. In a closed loop experiment, a specific observable (e.g. fluorescence from molecules or SHG from crystals) is used as feedback variable and guides a learning algorithm that progressively adjusts the laser field (normally its spectral phase) in order to maximize the feedback variable. The advantage of this approach is that no a priori knowledge of the system under study is needed. A disadvantage of closed loop coherent control is that often long time (several minutes or even hours) is needed for the learning algorithm to converge. The investigated systems must therefore provide sufficient, stable and long lasting signals for the experiment to be possible.

In the case of individual nano-emitters and large molecules at room temperature, the implementation of both the coherent control approaches outlined above is very demanding. For these complex systems the complete theoretical solution that maximizes the desired effect cannot be easily calculated. At the same time the stability requirements for a closed loop control experiment are generally in conflict with the specific nature of single emitters. As

one moves from ensemble measurements to the investigation of individual systems, the observable signal reduces to the single photon level, the shot-noise can be of the order of several percent [149] and photoinduced processes such as blinking and photobleaching, that quantum emitters like molecules and QDs undergo at room temperature [150], practically limit the observation time to few minutes. These difficulties explain why only few examples of coherent control in single emitters at room temperature exist so far. In previous works from this group [16–18] the coherence properties of single molecules and light harvesting complexes were investigated with a two-pulse delay experiment with pre-designed spectral phases. The choice of the laser fields was based on the ensemble absorption spectrum of the molecules, but did not assure the maximization (or minimization) of the targeted signal (the fluorescence from single molecules). A recent experiment [12] demonstrated enough sensitivity to attempt a closed loop control experiment on single molecules in the linear weak-excitation limit. In that case, no optimization could be obtained and the fluorescence signal from the molecules remained unchanged.

I describe here the closed loop control scheme we developed, which, by acting on the spectral phase of the laser field, is capable of optimizing the fluorescence signal from individual quantum emitters. The first step towards this achievement is the understanding that learning algorithms that work well for ensembles are not necessarily ideal for the investigation of single nano-systems. To overcome the problems associated with noise, instability and photobleaching of single emitters, a learning algorithm must fulfill two requirements.

- The trial phases used need to produce an effect larger than the stochastic noise of the signal, which allows the algorithm to determine the spectral phase within a certain subset that optimizes the signal from the single emitter. If the variation produced by the application of different phases is smaller than the intrinsic noise then phase induced changes are not detectable and the optimization of the control signal does not converge.

- The optimal solution has to be found in a limited amount of time, to reduce the effects of: experimental drifts (that become relevant when looking at single nano-systems) and photobleaching of the emitters.

In order to demonstrate the feasibility of the experiment, we used a novel, noise robust and fast converging learning algorithm [151], and studied the nonlinear response in single QDs characterized by high TPA cross section.

4.2 Principles of two photon coherent control

Coherent control of multiphoton transitions has been theoretically studied and experimentally demonstrated in ensemble of atoms, molecules and QDs [24, 32, 58, 86–88, 147, 152–160].

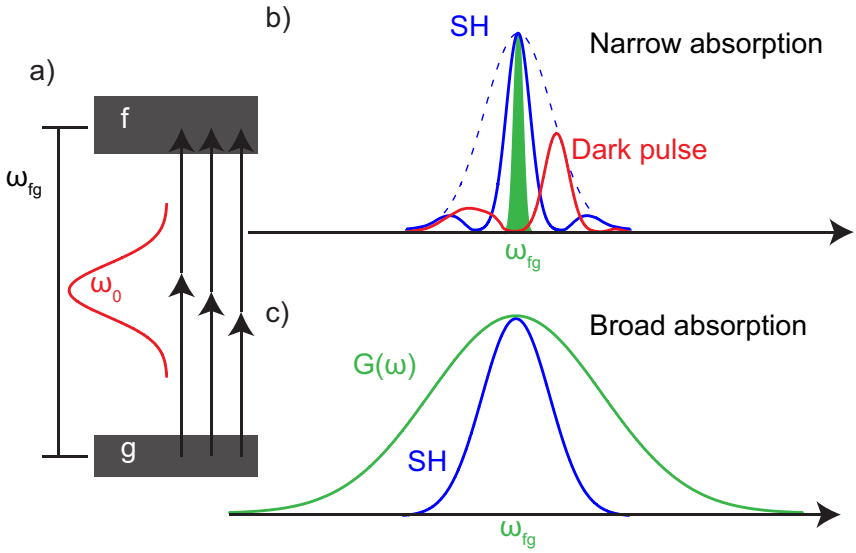

Fig. 4.1: a) Sketch of a two photon excitation process not mediated by any real intermediate state. b) Case of absorption line (green colored curve) narrower than the SH spectrum. Both the dashed and the solid blue curve maximally excite the TPA, whereas the red curve does not excite the system at all. c) Case of absorption lines broader than the SH spectrum. Only the FL pulse maximizes the TPA.

Consider a two level system as the one depicted in Fig. 4.1 a, formed by a ground state g and a final state f, and let $\hbar\omega_{fg}$ be the energy difference between the two levels. For quantum emitters in the solid state (like QDs) and at room temperature, the quantum states are energetically broad. Suppose that a laser pulse with a central frequency $\omega_0 \simeq \omega_{fg}/2$ and spectral width $\Delta\omega < \omega_{fg}/2$

excites such a system. Because there are no other states but g and f, no single photon transitions are available and the only possible excitation mechanism is the pure TPA. The total TPA probability can be written as [57, 58, 87, 153]:

$$P_{fg} = \int G(\omega_a) \left| \int E(\omega) E(\omega_a - \omega) d\omega \right|^2 d\omega_a \tag{4.1}$$

Where $G(\omega_a)$ represents the absorption cross section at the two-photon energy. The term $\left|\int E(\omega)E(\omega_a-\omega)d\omega\right|^2$ is the SH spectrum at the frequency ω_a (see Chap. 1). The excitation probability is essentially the product of the SH spectrum and the absorption cross section integrated over the two-photon frequency. Since the absorption cross section in Eq. (4.1) is a property intrinsic to the system, the only quantity one can act on to control the TPA is the term $\left|\int E(\omega)E(\omega_a-\omega)d\omega\right|^2$, which can be controlled by changing the spectral phase of the laser pulse. As illustrated in Fig. 4.1 a, and discussed already for the SHG case in Sec. 1.4.1, because the laser pulse is broadband in frequency, multiple pathways in the TPA can lead to the same final state, and interference establishes that can lead to coherent control [26, 57, 58].

From Eq. (4.1), the TPA is maximal for laser fields that maximize the SH at every frequency ω_a for which $G(\omega_a) \neq 0$. As illustrated in Fig. 4.1 two cases may exist: Fig. 4.1 b, $G(\omega_a)$ is spectrally narrower than the SH spectrum, which happens for instance for atomic transitions [86, 153]; or Fig. 4.1 c, $G(\omega_a)$ is broader than the SH spectrum, which is the case for many solid state quantum systems at room temperature [57, 58, 87, 147].

In the case of narrow absorption lines, the TPA can be greatly influenced by phase shaping the incident laser field [86, 153]. This can be understood from Fig. 4.1 b: the red SH spectrum, which can be obtained by imposing a certain spectral phase, has zero intensity in the range $G(\omega_a) \neq 0$ and thus does not excite at all the two level system. The corresponding laser pulse is a dark pulse for the system under study. In contrast, the dashed and the solid blue curves represent SH spectra both producing maximal TPA in the system, even if the first one corresponds to a FL pulse and the second one results from a non-flat spectral phase, and therefore a longer pulse.

The possibility of controlling TPA in systems with broad transitions by ultrafast phase shaping was first demonstrated in [57, 58, 147]. In this case, as shown in Fig. 4.1 c, since $G(\omega_a) \neq 0$ for every ω_a in the SH range, the only solu-

tion to the TPA maximization is the FL pulse, which maximizes the SH for every frequency. Nevertheless, by using tailored spectral phases and exploiting interference among the multiple pathways that are available for multiphoton excitation, it is possible to finely adjust the SH spectrum to the subtle differences in absorption of different species of molecules [57, 147, 161], or to enhance a certain nonlinear process with respect to another (for example two- versus three-photon absorption) [58].

In the case of the experiment described here, as shown later in this chapter (see Fig. 4.2), the QDs could only be excited through a pure TPA process, as the laser spectrum was chosen not to overlap with any available single photon transition in the QDs. Moreover, the absorption spectrum of the QDs was very broad at the SH range and all the SH frequencies could be absorbed with similar efficiency. The case of Fig. 4.1 c and the considerations made in this section for broad absorption lines therefore apply. In particular, in the experiment, we exploited the fact that FL pulses are the only solution to the maximization of the TPA (and therefore of the TPPL), to compare the result of the closed loop optimization against a theoretical prediction.

4.3 The quantum dots studied

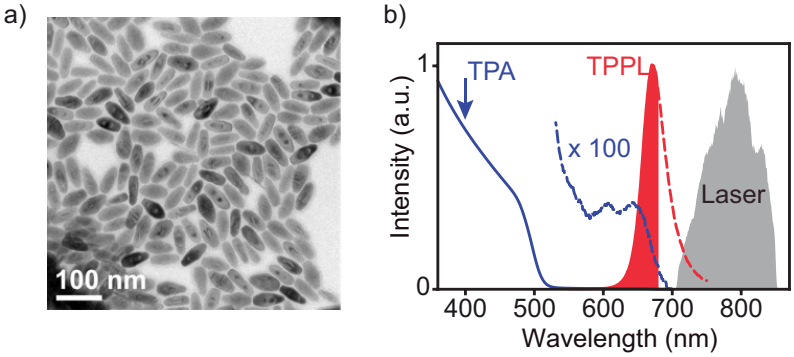

Fig. 4.2: a) Typical SEM image of a sample of QDs, taken from [162] b) Absorption and photoluminescence spectrum of the QDs, together with the laser spectrum used in the experiment. The colored region of the PL spectrum corresponds to the amount of PL detected in the experiment, considering that a 680 nm short-pass filter was used.

The QDs studied were made in the group of Iwan Moreels at the Italian Institute of Technology in Genova. They were colloidal QDs consisting of a core of cadmium selenide (CdSe) and a shell of cadmium sulphide (CdS). For fabrication details I refer to the recent work by Christodoulou et al. [162]. For the experiment, the QDs were dispersed in toluene and spin coated in a PMMA matrix on a microscope coverlsip.

Fig. 4.2 shows SEM images as well as optical characterization of the QDs. The QDs were composed of a 4.8x15 nm CdSe core rod embedded in a CdS shell that yielded an overall QD size of 9.8 nm by 44 nm. The relatively large (compared to other QDs or single molecules) volume of the CdS shell made them efficient two-photon absorbers [163–165], which in turns resulted in high TPPL emission. In general, in CdSe/CdS core/shell QDs the total volume determines the cross section for TPA and is given mostly by the CdS shell volume; whereas the exciton confinement, and thus the emission spectrum, can be tuned independently by changing the dimensions of the CdSe core. At the same time, the shell surrounding the core makes CdSe/CdS QDs very stable against photo-bleaching and blinking [166] and therefore suitable for single QD experiments. As one can see from Fig. 4.2 b, the investigated QDs had an absorption spectrum dominated by the CdS shell absorption with an onset at 515 nm, and a Stokes shifted photoluminescence (PL) emission centered at 670 nm. Fig. 4.2 b also shows that the laser spectrum did not overlap with the absorption of the QDs, meaning that only pure TPA (and not single photon absorption) was possible in this configuration. The colored region of the PL spectrum corresponds to the amount of PL we actually detected in the experiment, considering that a 680 nm short-pass filter was used to cut the laser light reflected from the sample.

4.4 The optimization algorithm

Fig. 4.3 is a sketch of a closed loop control experiment on a single QD. As in the previous chapters, the pulse shaper controlled the spectral phase $\varphi(\omega)$ of the laser field. The shaped pulse excited single QDs in the confocal microscope with two-photon excitation. The TPPL emitted by the desired QD was detected by an APD and constituted the feedback variable for the learning algorithm. The objective of the algorithm was to optimize the TPPL signal by

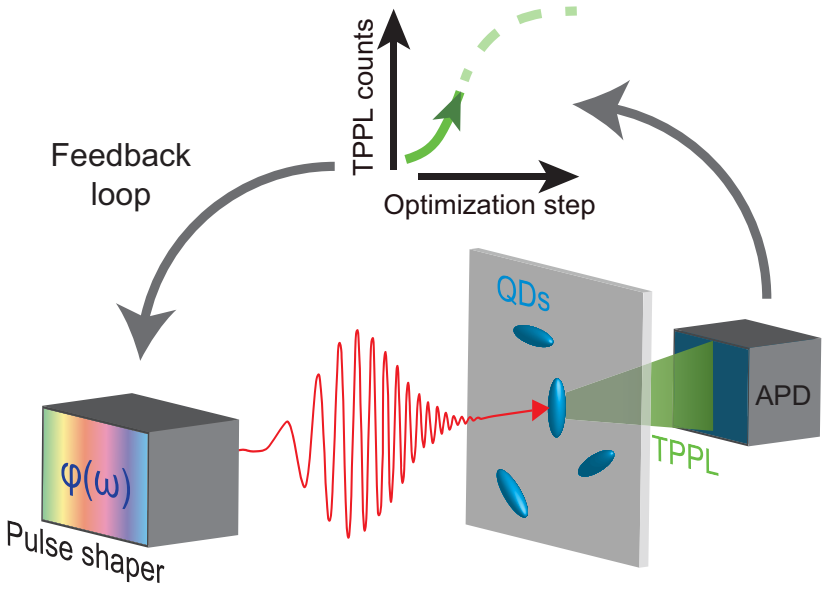

Fig. 4.3: Schematics of the closed loop control experiment on single QDs. The TPPL emitted by single QDs constitutes the feedback signal for the learning algorithm that changes the spectral phase applied by the SLM until the phase producing maximal TPPL is found.

changing the spectral phase of the laser pulse, i.e. by applying a phase mask on the SLM.

In the following, I describe the basic principles of the optimization algorithm. Further detail can be found in [151]. The algorithm divides the TPPL maximization problem in a series of simpler one-dimensional problems in the frequency domain, and it is therefore called multiple one-dimensional search (MODS) algorithm [151]. The electric field, for the Fourier theorem, can be decomposed in a linear combination of its frequency components, which is effectively what happens inside the pulse shaper (see Chap. 1), where the laser beam is dispersed by a diffraction grating and different parts of the SLM act on different frequency intervals. In the MODS optimization, the frequency intervals, also called nodes, are obtained by grouping together several pixels of the SLM. The optimization addresses one node at a time, changing its phase, while the other nodes are kept constant. Labeling every node with the index $j = 1,...n$, where n is the total number of nodes, the solution the algorithm

searches for is of the form:

$$E(t) \simeq \sum_j E_j e^{i\varphi_j} e^{i\omega_j t} \tag{4.2}$$

The MODS algorithm changes the quantities φ_j one at a time to maximize the desired feedback variable. For every node, the phase is varied a finite number of times, usually between 2 and 5 times, in the 0 to 2π range. φ_j is then fixed to the value that maximizes the TPPL and the algorithm proceeds to solve the problem for the $j+1$ case. Practically, in a complete iteration, n simpler optimizations are performed, in which the best φ_j is searched between 2 to 5 different possibilities. This process is illustrated in Fig. 4.4 in the case of $n = 40$ and 5 different searches for every node. In this case a complete iterations would require 200 different measurements.

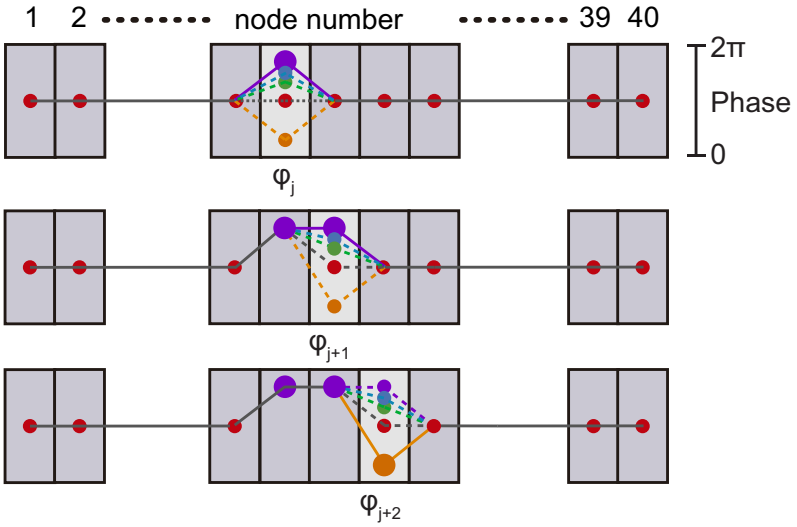

Fig. 4.4: Working principles of the MODS algorithm. The problem is divided in 40 nodes in the frequency domain. All the nodes are set to zero (red points) at the beginning. As the algorithm proceeds, the phase φ_j of individual nodes is changed separately (5 times) and fixed to the value that maximizes the feedback variable. Interpolation between adjacent nodes is performed to produce a smooth phase mask.

The choice of the number of nodes to use is critical for two main reasons. On the one hand it determines the sampling rate of the algorithm. The solutions that the algorithm can produce are limited to those functions that can

be sampled in the form of Eq. (4.2). If the best solution to a problem corresponds to a spectral phase $\varphi(\omega)$ that varies more rapidly than the sampling rate, the best solution cannot be well reproduced. Choosing a small number of nodes therefore limits the capability of the algorithm to find the best solution. On the other hand, the frequency band of a node also determines how large will the total change in the feedback variable (in this case in the TPPL from a single QD) be when varying φ_j from a value to a different one in the search for the maximum. As discussed above, an important criterion for the optimization success is that the variation of the feedback signal produced by the application of different phases, is larger than the intrinsic noise of the system. A too large amount of nodes, i.e. a too small frequency band associated to every node, would result in only small variations of the feedback signal, which might hamper the optimization. A careful choice of the number of nodes is therefore crucial in order to make the optimization possible and, at the same time, assure that the best solution can be reproduced to a sufficient level of approximation. The second requirement that the algorithm must fulfill in order to address single emitter problems, is to be fast, reaching the best solution to a given problem within the temporal limits imposed by signal drifts and photobleaching of the sample. As shown in the following, a total of 300 or fewer acquisitions is typically sufficient for the MODS algorithm to find the best solution, which is a reduction of one to two orders of magnitude compared to standard evolutionary strategies [12, 159].

4.5 Two photon absorption maximization in single quantum dots

Fig. 4.5 presents the main result of this experimental chapter, namely the realization of a phase-only closed loop optimization of the TPPL emitted by individual QDs at room temperature. Fig. 4.5 a and b show two dimensional confocal images of a sample containing CdSe/CdS QDs before and after the optimization procedure. After optimization overall higher signals were observed from the QDs. The bright spots in the images correspond to the TPPL emitted by single or small clusters of QDs. We choose QDs presenting low TPPL signal (circled QDs) as candidates for the optimization experiment on single emitters and performed photon correlation measurements to discrimi-

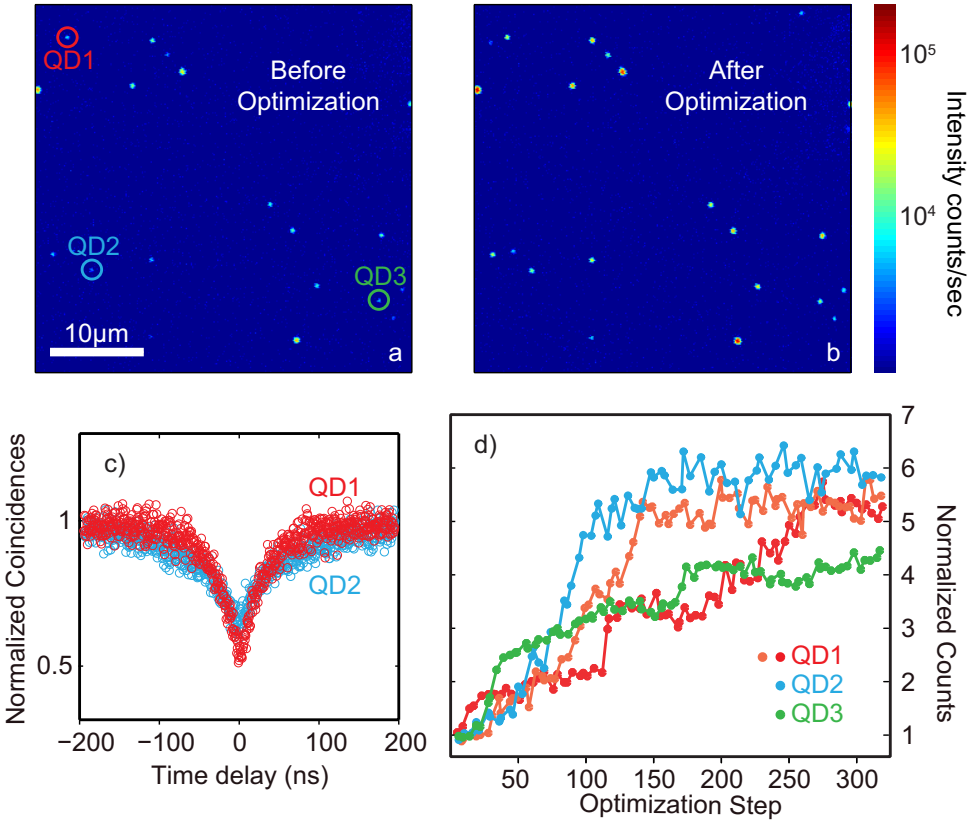

Fig. 4.5: a,b) TPPL image of the sample before and after the maximization. The TPPL signal from the QDs increases upon maximization. c) Photon correlation measurements for the indicated QDs. A pronounced antibunching dip at zero time delay is visible. As explained in the text, the measurement was not corrected for detector dark counts, or for the presence of biexcitons. d) Maximization traces taken on different QDs. The TPPL increases of a factor between 4 and 6. Parameters for the optimization: 40 nodes, 4 different searches for every node, 2 total iterations.

nate between single QDs and aggregates. For these measurements we used a helium neon laser that excited the QDs with one photon excitation, we subsequently divided the collected PL from the QDs with a beam splitter and sent it to two different APDs arranged in a Hanbury-Brown and Twiss intensity interferometer configuration. The results are shown in Fig. 4.5 c, which confirm that the QDs indeed behaved like non-classical quantum emitters, as can be

deduced from the photon antibunching dip at time zero. Second order photon correlation traces were not corrected for accidental coincidences arising from detector dark counts, neither for the presence of biexcitons in QDs. Thick-shell QDs, like the ones used here, present high biexciton photoluminescence quantum yields [167]. This has the effect of increasing the normalized coincidences at zero-time delay up to $\frac{1}{2}$ for high excitation powers [168] (a relatively high power was necessary in these experiments in order to characterize many different QDs in a reduced amount of time).

After selecting the suitable QDs behaving as single emitters, the MODS algorithm was used to perform TPPL optimization on the chosen QDs. Different optimization traces are presented in Fig. 4.5 d, where the TPPL for three different QDs is plotted for every step of the optimization algorithm. As different phases were applied by the SLM, the TPPL signal increased until reaching a maximum value. For all the investigated QDs the TPPL was found to increase by a factor of approximately 4 - 6. In the case of QD3, a lower TPPL increase was found, which might have several explanations. For this specific QDs the maximization process might have followed a different path with respect to the other QDs. As a consequence, additional iterations might have been necessary in order to reach full maximization. Another possible explanation is the drift in the TPPL signal during the experiment. For some QDs upon continuous illumination for several seconds, a slight TPPL decrease was noticed, probably as a consequence of small photo damage of the QD surface.

Even if slightly different amounts of TPPL increase were measured for different QDs, the results of Fig. 4.5 show that our closed loop control scheme was capable of optimizing the TPPL even from a single QD. To make a comparison with previous single molecule investigations from this group [16, 18] it must be noted that: (i) this experiment was carried out in low signal conditions. For these QDs the typical TPPL intensity was in the range 2000 to 7500 photons per second with an average excitation power of $20-50\,\mu$W, which is comparable to the power and signal levels used in [16]. (ii) With a total number of 300 acquisitions, the algorithm was able to find the optimal solution. In order to have sufficient signal to noise ratio, typical integration times of 100 to 800 ms were used for every acquisition. This means that the full maximization was carried out in about a minute, which is in stark contrast to other evolutionary optimization strategies in which hundreds of generations with a pool of hundreds of measurements per generation are necessary. Under

such conditions, closed loop control experiments become possible even in single molecules, where the typical signals are low and the times before photobleaching in the few minutes range.

4.6 Characterization of the optimal solution

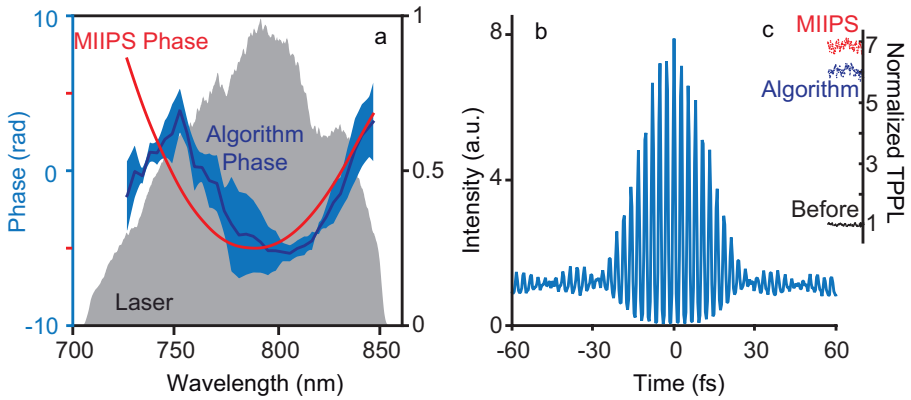

Fig. 4.6: a) Laser spectrum (shaded grey curve), initial spectral phase measured with MIIPS (red curve) and the inverse phase mask obtained with the closed loop optimization on QDs (blue curve). The light blue shaded region represents the uncertainty on the determination of the phase mask, corresponding to the standard deviation calculated repeating the maximization process several times. b) Autocorrelation of the final laser pulse, corresponding to a pulse duration of 20fs. c) Comparison of the normalized TPPL counts from a single QDs before optimization (black points), applying the algorithm phase (blue points) and the MIIPS phase (red points).

To conclude that the closed loop control scheme described in this chapter is indeed applicable to single molecule investigations, it is necessary to verify the quality of the solution found by the algorithm. As discussed in Sec. 4.2, for the QDs studied here, the only solution that maximizes the TPA, and hence the TPPL, is the FL pulse. The closed loop control experiment started with a pre-defined initial phase mask applied by the SLM, which was progressively changed until a final phase mask that maximized the TPPL from the QDs was reached. Assuming that the algorithm essentially compensated for the phase distortions and compressed the pulse in time, then the difference between the initial and the final phase mask should correspond to the phase distortions

initially present in the pulse.

The phase difference between the initial and the final phase applied by the SLM, called the algorithm phase, is shown in Fig. 4.6 a. We then separately measured the initial phase distortions of the laser pulse using MIIPS on SH nanoparticles, as described in Chap. 2, which is shown in red in Fig. 4.6 a. Because the algorithm phase and the MIIPS phase look similar, it is possible to conclude that the MODS algorithm indeed compressed the pulse in time, in agreement with theoretical predictions. This is confirmed by the pulse autocorrelation (Fig. 4.6 b) measured with the final phase mask applied on the SLM, which corresponds to a pulse as short as 20fs, close to the FL. An additional confirmation, which also gives a good comparison with the MIIPS results is given in Fig. 4.6 c, which shows the normalized TPPL counts from a single QD before any optimization, i.e. with the initial phase, with the algorithm phase and the MIIPS phase applied respectively. The signal increase obtained with the MODS algorithm was close to 90% of what MIIPS could obtain. This practically means that the MODS algorithm found a solution that was close to the FL pulse, without retrieving the perfect pulse compression. However, one has to take into account that MIIPS is an optimized method for compressing pulses and takes advantage of the good theoretical knowledge of nonlinear optical processes to obtain FL pulses. In contrast, the MODS algorithm does not need any pre-knowledge and can optimize on arbitrary signals. It is thus remarkable that, without any assumption, using very small signals and in very little time, the MODS algorithm manages to retrieve the 90% of the available signal. In the frequency domain this means that the algorithm rearranged the different frequency intervals (the nodes) such that they constructively interfered at the sample position (see also Sec. 1.4.1), thereby creating maximal TPA, and hence TPPL, in the QDs, which constitutes the simplest coherent control experiment on single quantum systems.

These results, together with those shown in the previous section, demonstrate that the closed loop control scheme presented here is able to optimize a signal generated by individual quantum emitters, finding a solution that is close to the one predicted by theory in a reduced amount of time. Closed loop coherent control experiments on single molecules at room temperature become possible. At the same time, the rapid optimization of the TPPL in QDs constitutes a new pulse compression method on a deeply subwavelength spatial scale. Compared to the results presented in Chap. 2, this method presents

few advantages: (i) it does not require detection of the full SHG spectrum, which is hard to acquire for laser wavelengths shorter than 700 nm (SHG wavelengths < 350 nm) due to absorption from the refractive optical components; (ii) the QDs used here were 100 times smaller in volume than the SHG nanoparticles previously used, which makes them the smallest particles ever-used for pulse compression by far; (iii) the excitation power needed for generating enough TPPL for the algorithm to converge was 20 to 300 times less than the one used for single SHG nanoparticles, which might make this method suitable for pulse compression and TPPL maximization in living tissues.

4.7 Conclusions

In this chapter I have demonstrated a closed loop control experiment capable of addressing a single quantum emitter in the solid state at room temperature. By optimizing the TPPL in single QDs characterized by broadband absorption at the SH frequency, and using a novel MODS algorithm, the experiment satisfied at the same time all the requirements for its applicability to the closed loop coherent control of single molecules and other nano-systems. The signal levels in the measurements were as low as the ones found in real single molecule experiments; the TPPL maximization was performed in less than 4 min, which is well below typical phtobleaching times; the solution found by the algorithm well reproduced the theoretical expectations for the systems studied.

With this result at hand, we are finally able to perform real closed loop control experiments, where the coherent responses of individual nano-systems are actively manipulated to reach the desired outcome. In the next chapter I describe such an experiment carried out on resonant nanoantennas.

CHAPTER 5

Controlling the two-photon absorption in nanoantennas

In this chapter I present a study of the two-photon absorption in gold nanoantennas, which was demonstrated to occur through two successive single photon absorption events. For resonant structures, the surface plasmon resonance acts as the intermediate state. Here, I argue that, because the localized surface plasmon resonance has a finite coherence time on the order of 15 fs, a very fast coherent regime in the nanoantennas develops in which the two-photon absorption process is sensitive to the phase of the incoming field. In this regime coherent control based on active phase shaping of the laser field becomes possible. In the first part of the chapter I show evidences of this coherent regime in single resonant nanoantennas. By studying two different nanoantennas at the same time and using the closed loop coherent control scheme described in the previous chapter, I then demonstrate that they can be separately controlled using ultrashort (shorter than 50 fs) phase tailored laser pulses.

This chapter is based on:

- **Accanto N**, de Roque P, Galvan-Sosa M, Hancu IM, & van Hulst NF. *Closed loop phase control of the coherent two-photon absorption in resonant optical nanoantennas.* In preparation (2016)

In this chapter I describe the design and experimental realization of a closed loop coherent control scheme in resonant gold nanoantennas. In Chap. 3 I showed that ultrafast phase-controlled pulses can excite, and resolve, a coherent response in such systems. In Chap. 4 I presented a method for closed loop optimization experiments even at the level of single quantum emitters. It appears natural to combine these abilities together in order to obtain active control of the plasmonic response in nanoantennas.

Stockman and collaborators first linked the field of coherent control to the study of optical nanoantennas with the objective of simultaneously achieving nanometer as well as femtosecond control of optical fields [115, 169]. In their theoretical proposal, they suggested that, in a plasmonic system where different LSPRs exist at different spatial positions, an electric field with a tailored spectral phase could excite different LSPRs at different times. This could allow the localized energy to be actively shifted from certain spatial locations of the nanostructures to others on an ultrafast timescale. The feasibility of such control principles was subsequently demonstrated experimentally [4, 37, 170]. In these works, however, the role of the coherence of the surface plasmons was not fully exploited. In particular, non-resonant structures were studied in [4, 170] and the laser pulses were too long to probe any plasmonic coherence. In [37] the coherent response of the nanoantennas was mainly used to measure their LSPRs, whereas the relation between the temporal evolution of the electric field demonstrated there and the coherence in the systems was not obvious.

In this chapter I present a comprehensive study of the TPA process in gold nanoantenans. The chapter is divided into two main experimental sections. In the former I show that, in resonant structures, for ultrashort laser pulses (pulse duration shorter than 50 fs), a coherent regime develops in which the TPA (and therefore the TPPL) is sensitive to the spectral phase of the laser pulse and can therefore be actively controlled solely by phase shaping. I then describe a closed loop coherent control experiment, based on the use of the MODS algorithm (see Sec. 4.4), that separately controls the TPA in two different nanoantennas by working in such a coherent regime and exploiting the subtle differences in their resonant response.

5.1 The nanoantennas studied

The sample studied in this chapter was similar to the one described in Sec. 3.4. It consisted of gold nano-rods of length varying between 90 nm and 190 nm, fabricated using electron beam lithography on a glass coverslip coated with a 10 nm thin layer of indium tin oxide (ITO). SEM images of the nanoantennas are shown in Fig. 3.10. The width and height of the nanoantennas were both fixed at 50 nm and they were fabricated to be resonant with the basic $\lambda_{\text{eff}}/2$ mode (where λ_{eff} is the effective wavelength of the guided mode along the nano-rod axis) excited by the laser field. In order to study two nanoantennas characterized by different LSPRs at the same time, they were arranged in pairs of different lengths separated by 2 μm.

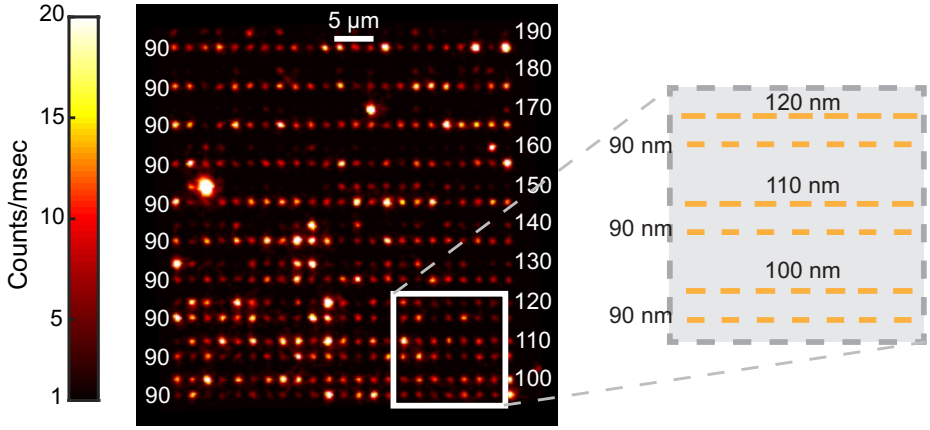

Fig. 5.1: TPPL image of an array of nanoantennas together with a schematic of the arrangement of the sample. Ten different rows of nanoantenna pairs are present in the array. The lower nanoantennas in the pair has a length of 90 nm and the upper length ranges from 100 nm to 190 nm. Higher TPPL signal is detected in correspondence to nanoantennas of length from 90 nm to 120 nm, which are in resonance with the excitation field. The schematic on the right side is a zoom in the region of resonant nanoantennas.

Fig. 5.1 shows a confocal TPPL image of an array of the investigated nanostructures. Ten different rows of nanoantenna pairs are visible, in which the length of the lower nanoantennas in the pairs was kept at the constant value of 90 nm, whereas that of the upper ones was swept from 100 to 190 nm. As Fig. 5.1 demonstrates, nanoantennas of lengths ranging from 90 nm to 120 nm

produced higher TPPL than the others, suggesting that they were in resonance with the excitation field. Because for nano-rods of constant width, increasing the length shifts the spectral position of the LSPR to the red [92], 90 nm (120 nm) long nanoantennas should be resonant with the blue (red) part of the laser spectrum respectively (as confirmed by simulations shown in Fig. 5.9).

5.2 The role of the intermediate state

The TPPL has extensively been used to investigate plasmonic nanoantennas [37, 89–93, 171–173]. The nature of the TPA process in gold was studied by different groups [89, 91, 119, 171, 174] and demonstrated to involve two successive single photon absorption processes, mediated by a real transition. In the case of nanoantennas resonant with the laser pulse, the LSPR acts as the intermediate state, enhancing the TPA process [91, 119]. In other words, the excitation laser induces the absorption of a first photon at the LSPR frequency after which a second photon is absorbed to complete the TPA process. This is in contrast with, for example, the case of the QDs described in Chap. 4, where the TPA occurs through a virtual state (see Fig. 4.2).

Biagioni and collaborators [89] studied the dependence of the TPPL intensity in gold nano-structures on the pulse duration, for pulses longer than the plasmon dephasing time. Decreasing the pulse duration from 10 ps to $\sim$ 1 ps resulted in an increase of the TPPL, followed by a saturation behavior for pulses in the range 1 ps to 50 fs, where the TPPL no longer varied as a function of the pulse duration. For a pure two-photon excitation process with no intermediate transition (as the TPA in QDs or the SHG in crystals) instead, one would expect that the two-photon excitation probability scales as the inverse of the pulse duration, therefore continuously increasing as the pulse gets shorter in time [58]. The behavior of the TPPL in gold can be explained on the basis of a resonant mediated TPA, where the intermediate state has a finite lifetime [89, 91, 119, 171]. In such a scenario, the second photon impinging on the sample at a different time than the first one but within the lifetime of the intermediate state, still interacts with the intermediate state population excited by the first photon, and thus can lead to TPA. As a consequence, for resonant mediated TPA, changing the pulse duration below the intermediate state lifetime, but still above the plasmon dephasing time, does not produce

appreciable changes in the total TPA and therefore in the TPPL [89]. For pulses longer than the lifetime instead, a dependence on the pulse duration is observed. In this case, making a pulse shorter increases the probability that a second photon absorption occurs before the intermediate state population has decayed and therefore increases the probability for TPA. The lifetime of the intermediate state was previously measured for different nano-structures and determined to be in the few hundreds to thousands of femtosecond range [89, 91, 174].

However, as shown in Chap. 3 and recently measured by different groups [7, 8, 13, 37, 116–121], the plasmon dephasing time in plasmonic nanoantennas is on the order of ~ 15 fs, and therefore within the time resolution of our laser system. By decreasing the pulse duration below 50 fs, one should be able to induce and detect coherent effects in the TPA. To explore this regime we therefore investigated the dependence of the TPPL in gold nanoantennas on the pulse duration, for pulses shorter than 50 fs.

5.2.1 Dependence of the TPA on the pulse duration

The results of this experiment are shown in Fig. 5.2. The length τ of the pulse was varied in the range 20 fs to ~ 1 ps by applying different amounts of linear chirp with the SLM. We performed two different experiments: first, we recorded the variation of the SH intensity from a single $BaTiO_3$ NP, which we used as reference; second, the TPPL as a function of the pulse length from a resonant 90 nm nanoantenna in the sample of Fig. 5.1 was measured.

It is important to specify here that, even if the nanoantennas themselves produce SH, as demonstrated in Chap. 3, in general the ratio between the SH and TPPL intensities is quite low, meaning that they mainly produce TPPL and only little SH. Moreover, because the SH signal is expected to decrease for long pulse duration, measuring SH from single nanoantennas for pulses longer than 100 fs would be very challenging. We therefore decided to use $BaTiO_3$ NPs as SH references because the measurements could be performed more easily. At the same time, when measuring the TPPL from nanoantennas we made sure that the contribution from SHG was negligible. For TPPL measurements we used 680 nm short-pass filters to cut the laser spectrum. We carefully checked that, at the power used, no SH spectrum could be mea-

sured even for the shortest pulse duration. Repeating the TPPL experiments presented in Fig. 5.2 adding a 500 nm long-pass filter to cut the SHG produced the same results, confirming that no spurious SH component was present.

As expected from theory [58], the SH intensity varies as τ^{-1} and the experimental points in the graph of Fig. 5.2 a are well reproduced by the calculations based on the excitation laser spectrum and the applied spectral phase. The small difference between the data and theory might be attributed to the error in the measurement of the laser spectrum (a possible difference in the detection efficiency of the spectrometer between the blue and red side of the broadband laser results in an error in the SH prediction), or in a discrepancy between the phase we sent to the SLM and the real spectral phase applied on the laser pulse, especially for large values of the applied chirp. In the case of the TPPL instead, for $\tau > 100$ fs the experimental results are compatible with a description of the TPA process given by equation [89, 174] :

$$\underset{\tau>100}{\text{TPA}} \propto \int E_\tau(t)dt \int E_\tau(t-t_1)e^{-t_1/T_{\text{LT}}}dt_1 \tag{5.1}$$

Where $E_\tau(t)$ represents the time varying electric field as a function of the pulse duration τ that is controlled with the pulse shaper and T_{LT} is the lifetime of the intermediate state. A fit of the experimental TPPL data in Fig. 5.2 a using Eq. (5.1) produced the cyan dashed curve in Fig. 5.2 a, which well describes the behavior of the TPPL for pulses longer than 100 fs, yielding a lifetime $T_{\text{LT}} \simeq 350$ fs. This value is in partial agreement with that found in [174] where the measured lifetime was $\simeq 600$ fs for similar resonant nanostructures. Considering that there is an uncertainty in the quantities $E_\tau(t)$, as already mentioned for the small discrepancy between the SH data and simulations, the value of $T_{\text{LT}} \simeq 350$ fs is also affected by an error and should not be regarded as an absolute number. As the main outcome of this section is not the perfect measurement of the intermediate state lifetime, the conclusion can be drawn that the data presented in Fig. 5.2 a for pulses longer than 100 fs are in general agreement with previous findings.

However, Eq. (5.1) fails to describe the experimental points for pulse durations below 100 fs. This region can be assigned to the appearance of a coherent regime in which the interaction of the two successive single photons with the nanoantenna depends on the relative phase of the two photons. In the limit

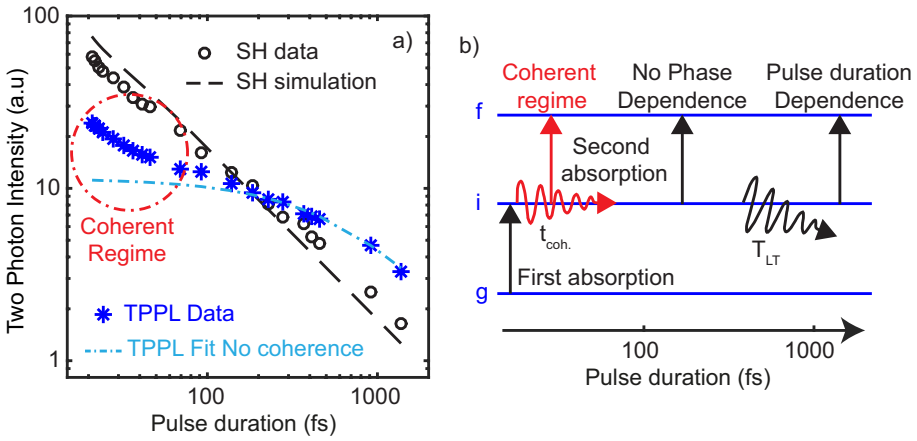

Fig. 5.2: a) Experimental dependence of the SH (black circles) and the TPPL from a resonant 90 nm long gold nanoantenna (blue stars) on the total pulse duration τ, changed by chirping a broadband laser pulse. The black dashed curve is the predicted behavior of the SH, which agrees well with the experiment. The cyan dash-dotted curve corresponds to a fit to the TPPL for $\tau > 100$ fs using the model described in the text from which we inferred a lifetime of the intermediate state $T_{LF} \simeq 350$ fs. For pulses shorter than 100 fs a coherent regime develops. b) A sketch of the three different regimes involved in TPA as a function of the pulse length. g, i, f are the ground, intermediate and final states involved in the TPA respectively.

of $\tau < T_{\mathrm{LT}}$, Eq. (5.1) predicts that the TPA is proportional to the time integral of the pulse autocorrelation, a value that is independent of the spectral phase of the laser pulse and therefore of the pulse duration. For very short laser pulses, Eq. (5.1) needs to be modified to account for the spectral phase of the laser field.

5.2.2 The very short pulse limit

Previous coherent control experiments in systems where the TPA is mediated by a real transition, were mainly performed with pulse durations being much shorter than the dephasing time of the intermediate state. Very narrow absorption lines in atoms [175, 176] or relatively broader absorptions (but still narrower than the laser spectra) in rare earth systems [88] were studied. In the experiment described here, the LSPR had a bandwidth comparable to that of the laser field and a dephasing time of the order of the pulse duration. None of

the previous cases is therefore directly applicable, even if the approximations given in [88] might provide some basic understanding of the processes involved in the case of very short laser pulses. Under the approximation that no other plasmonic resonances exist at the two-photon energy, which is reasonable for nanoantennas fabricated to be resonant with the fundamental laser field, the TPA probability can be written as [88]:

$$\underset{\tau<100}{\mathrm{TPA}} \propto \left| \int d\omega \int d\Omega A(\omega) E_A(\omega) E_A(\Omega-\omega) \right|^2 \tag{5.2}$$

Recalling the discussion of Chap. 3, the local field $E_A(\omega)$ is the incident electric field multiplied by the local response of the nanoantenna, i.e. $E_{\mathrm{A}}(\omega) = E_0(\omega)A(\omega)e^{-i[\varphi(\omega)+\varphi_{\mathrm{A}}(\omega)]}$. Because the response of the nanoantenna is dominated by the amplitude contribution, in this approximation the phase component $\varphi_{\mathrm{A}}(\omega)$ can be neglected.

In the limit of pulses shorter than the dephasing time of the intermediate transition, Eq. (5.2) implies that the TPA does indeed depend on the phase of the incoming electric field. Moreover, considering that $A(\omega)$ is a real function, the dependence of the TPA on the spectral phase of the laser field is similar to that of the SHG (see Eq. (1.9)). This means that in these limits, in the case of the pulse duration experiment, the TPA probability recovers the τ^{-1} dependence. In the graph of Fig. 5.2 indeed, for very small τ values, the behavior of the TPPL in a resonant gold nanoantenna becomes similar to that of the SH intensity. This finding supports the existence of a coherent regime in the limit of very short pulses.

5.2.3 Coherent control of a single nanoantenna

Taken together, the two equations presented above (Eq. (5.2) and Eq. (5.1)) show that, for $\tau < T_{\mathrm{LT}}$, two different regimes may exist in the nonlinear absorption in resonant nanoantennas: (i) the coherent regime that develops for ultrashort pulses, comparable to the plasmon dephasing time, for which the TPA is sensitive to the spectral phase of the laser pulse; (ii) the incoherent regime, for pulses longer than the plasmon dephasing time, but still shorter than the intermediate state lifetime. In this regime no dependence on the spectral phase of the laser pulse is expected. A simple sketch of the different regimes involved

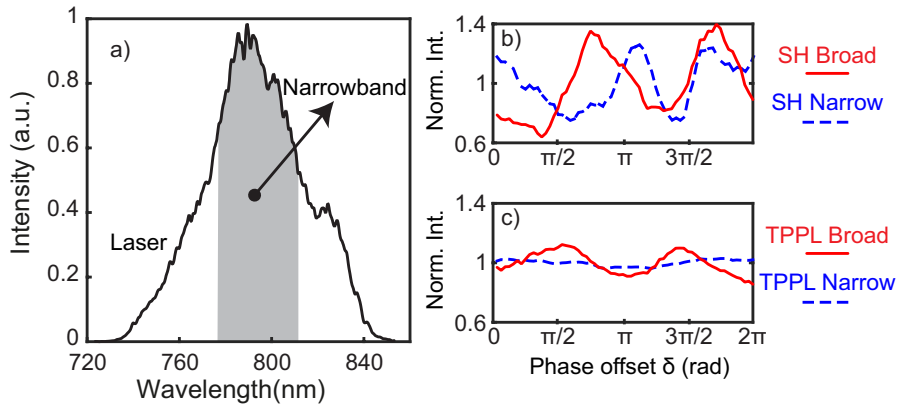

Fig. 5.3: a) Broadband and narrowband excitation spectra used in the experiment. b) Integrated SH MIIPS trace taken on a SH NP under broadband (red solid curve) or narrowband excitation (blue dashed curve). c) Integrated TPPL MIIPS trace taken on a resonant nanoantenna under broadband (red solid curve) or narrowband excitation (blue dashed curve).

is reported in Fig. 5.2 b.

To confirm the existence of these regimes, we performed preliminary MIIPS experiments detecting the TPPL from a resonant nanoantenna, subject to broadband (100 nm) or narrowband (30 nm) excitation respectively. The narrowband excitation was obtained by selecting a portion of the laser spectrum in the Fourier plane of the SLM, i.e. a 30 nm band centered around 790 nm. The two excitation spectra are reported in Fig. 5.3 a. The pulses were compressed to the FL, which yielded 17 fs and 63 fs for the broad and the narrowband excitation conditions respectively. The results of one spectrally integrated MIIPS scan in the two different cases for a SH NP (detecting the SH) and for a resonant nanoantenna (detecting the TPPL) are plotted in Fig. 5.3 b and c respectively. The MIIPS parameter γ (see Sec. 1.4) was set to 16 fs for the broadband pulse and to 63 fs for the narrowband pulse. As shown in Fig. 5.3 b, this choice ensured similar modulation depths in the integrated SH MIIPS trace for the two cases. In other words, the signal variation (from the minimum to the maximum) obtained in the SH case was comparable in the two experiments and no net loss in the shaping capability was suffered. The integrated TPPL MIIPS traces in the case of a resonant nanoantenna are reported in Fig. 5.3 c. This graph demonstrates that the modulation depth obtainable

by phase shaping the laser pulse was much smaller than for a SH NP, even for the broadest spectral excitation. Moreover, changing from broadband to narrowband excitation, almost completely eliminated the dependence of the TPPL signal on the spectral phase of the laser pulse.

Although these results are still preliminary and more experiments are necessary to shed further light on this phenomenon, they support the interpretation given here as to the nature of the mechanisms governing the TPA process in gold nanoantennas. For very short pulses (comparable to the plasmon dephasing time), the TPA probability depends on the relative phase of the photons involved in the absorption process. However, the TPPL modulation one can induce with phase shaping is much smaller than for a pure (not resonance mediated) two-photon excitation process. Importantly, the phase shaping capability is completely lost for pulses that are longer than the plasmon dephasing time but still shorter than T_{LT}.

Furthermore, in contrast to SHG in NPs and TPA in QDs, the TPA in gold nanoantennas presents a direct and intimate relation to coherence. Because of the presence of the intermediate state, the TPA, despite being a nonlinear process, is only sensitive to the spectral phase of the laser field for pulses that are shorter than the plasmon dephasing time. By changing the bandwidth of the excitation it is possible to switch from a coherent to an incoherent regime. This unique property makes resonant gold nanoantennas perfect systems for performing nanoscale nonlinear coherent control as it makes it possible to differentiate between coherent and incoherent interactions. A coherent control experiment must make use of ultrashort (below 50 fs) laser pulses.

5.3 Closed loop coherent control of nanoantenna pairs

Based on the above discussion, this section extends the closed loop control scheme developed in Chap. 4 to the coherent control of resonant nanoantennas. The objective of a control experiment is often to change the relative importance of different light-matter interactions. One of the the main applications of coherent control is indeed the steering of chemical reactions towards a desired outcome, thus eliminating undesired reaction pathways [21–23, 26, 142].

Here, the goal is to design, and perform, a closed loop coherent control experiment capable of separately addressing different nanoantennas. Eq. (5.2), however, suggests that a blind closed loop optimization on the TPPL from a single resonant nanoantenna would not accomplish this objective. In the coherent regime, the TPA probability is maximized for FL pulses (as in the case of the SHG). Therefore, a MODS optimization would essentially temporally compress the pulse, as already seen in Chap. 4 for QDs. However, the strong dependence of the TPA on the LSPR (the term $A(\omega)$) gives the possibility of controlling the relative TPA in two different systems with amplitude responses $A_1(\omega)$ and $A_2(\omega)$, by shaping the phase of the laser pulse. Tailored spectral phases could enhance the TPA in certain nanoantennas, while inducing destructive interference and therefore removing TPA probability from undesired ones.

A correctly designed coherent control experiment should therefore optimize on the ratio between the TPPL emitted by two different nanoantennas with different LSPRs. This TPA maximization strategy is similar to the one used in [147] on ensembles of different molecules.

5.3.1 Experimental details

In order to simultaneously excite, and detect, the TPPL from two different nanoantennas, the optical setup described in Chap. 1 was slightly modified, as illustrated in Fig. 5.4. In practice, the laser beam was focused from the top of the microscope onto the sample using a low numerical aperture (NA=0.15) objective, resulting in a $\sim 8\,\mu$m excitation spot and therefore allowing two separated nanoantennas in one array to be excited at the same time. The TPPL was collected from the bottom of the sample through a 1.4 NA objective with field of view of $\sim 100\,\mu$m that could therefore collect the emission from both the structures at the same time. The TPPL was consecutively sent to two different APDs after being separated by a beam-splitter. To reject the laser light for both the APDs we used 680 nm short-pulse filters. The combination of the collection objective, the system of lenses that focused the light onto the APDs and the physical size of the active area of the APDs was such that the APDs received light form a much smaller area than the excitation spot, roughly $1\,\mu$m in diameter. By slightly moving the two APDs in different directions it was thus possible to align them on the TPPL emitted by different nanoantennas.

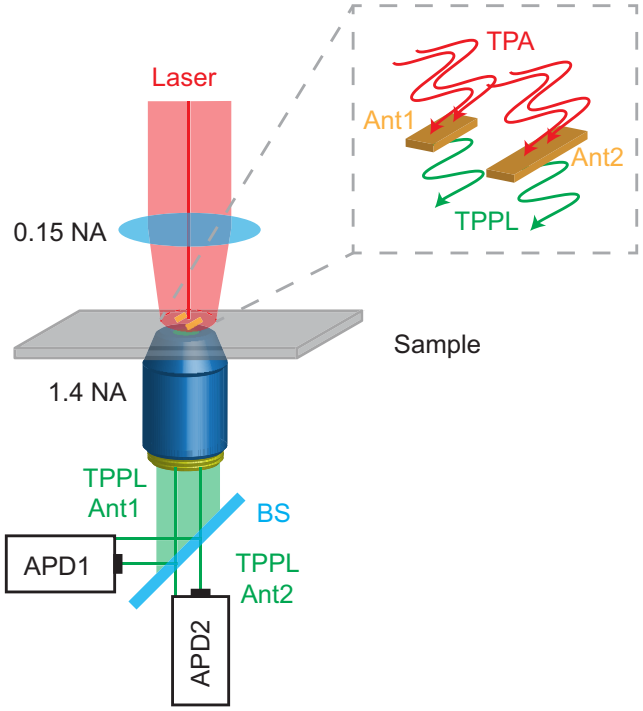

Fig. 5.4: a) Sketch of the setup used for the coherent control on pairs of nanoantennas. Two different nanoantennas are excited at the same time from the top of the microscope using a 0.15 NA objective, their TPPL is collected from the bottom through a 1.4 NA objective, separated by a beam-splitter and detected by two different APDs. By moving the APDs in opposite direction it is possible to align each of them on a different nanoantenna.

Importantly, by operating the system in this configuration, the spatial resolution at the sample position was still high enough to produce high quality two-dimensional images of the sample, as will be shown in the rest of the chapter.

As sketched in Fig. 5.5, the ratio between the signals from the two APDs, i.e. the ratio between the TPPL from two different nanoantennas, was used as feedback variable for the MODS algorithm, with the goal of optimizing the nonlinear excitation of one nanoantenna with respect to the other, by changing the laser spectral phase and taking advantage of the subtle differences in their coherent responses. The maximal control capability should be associated with systems that mostly differ in their relative resonance position.

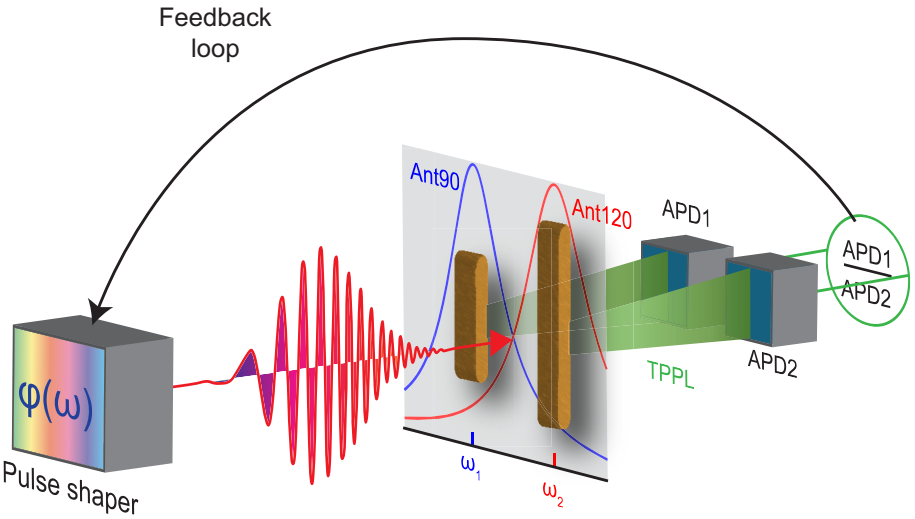

Fig. 5.5: Schematics of the experiment. Two different nanoantennas, with spectrally detuned LSPRs are excited by a phase shaped laser pulse. The ratio of the emitted TPPL is used as feedback variable for the MODS algorithm.

We therefore selected 90 nm and 120 nm nanoantennas to perform the closed loop coherent control experiment on pairs of nanoantennas.

5.3.2 Control of the relative emission from two nanoantennas

The main result of this chapter, namely the closed loop coherent control of a pair of 90 nm and 120 nm nanoantennas is presented in Fig. 5.6. Let the quantities I_{90} and I_{120} be the TPPL emitted by the two nanoantennas. The goal of the closed loop coherent control experiment was to find two spectral phases, $\varphi(\omega)_{\max}$ and $\varphi(\omega)_{\min}$, that maximized or minimized the ratio I_{120}/I_{90}, respectively. As discussed in Sec. 5.2, this is only possible for ultrashort excitation pulses. For this reason we started with FL pulses and allowed the MODS algorithm to optimize the relative TPPL of the nanoantennas.

In the graph of Fig. 5.6 a, the ratio I_{120}/I_{90} as a function of the algorithm step for both the maximization and minimization experiments is shown. The experimental data were normalized such that the initial I_{120}/I_{90} value (corresponding to FL pulses) was equal to one. In both the maximization and

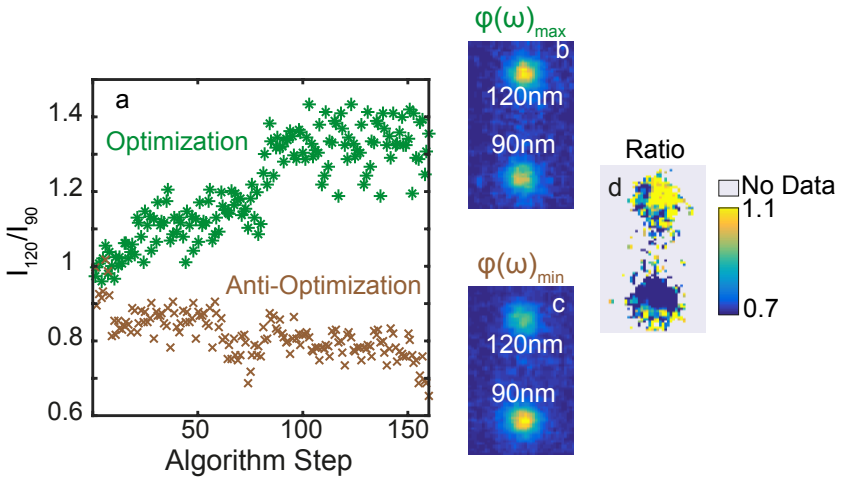

Fig. 5.6: a) Ratio between the signal from a 120 nm and a 90 nm nanoantenna as a function of the optimization steps made by the algorithm. The green points correspond to the maximization of I_{120}/I_{90} whereas the brown ones refer to its minimization. b,c) Two dimensional TPPL images of the two nanoantennas taken with $\varphi(\omega)_{\max}$ and $\varphi(\omega)_{\min}$ respectively. Note that the TPPL maximum switches from the 120 nm to the 90 nm nanoantenna. d) The ratio between images b and d emphasizes the contrast between the two nanoantennas

minimization experiments the ratio between the TPPL signals changed as the spectral phase applied by the SLM varied. The spectral phases $\varphi(\omega)_{\max}$ and $\varphi(\omega)_{\min}$ that maximized and minimized the ratio I_{120}/I_{90} were determined in only 160 steps, integrating 500 ms per step. Let the quantity $I_{120}^{\max}$ and $I_{120}^{\min}$ represent the TPPL intensity from the 120 nm nanoantenna generated by the application of the spectral phases $\varphi(\omega)_{\max}$ and $\varphi(\omega)_{\min}$ respectively (and analogous quantities for the 90 nm one). The absolute contrast between the two nanoantennas is defined as:

$$\frac{I_{120}^{\max}}{I_{120}^{\min}}\frac{I_{90}^{\min}}{I_{90}^{\max}} \tag{5.3}$$

As one can see from Fig. 5.6 a, the total contrast achieved in the experiment was approximately 2.

Fig. 5.6 b and c show TPPL images of the two nanoantennas acquired with

the spectral phases $\varphi(\omega)_{\max}$ and $\varphi(\omega)_{\min}$, respectively. The TPPL maximum switched from one nanoantenna to the other upon application of the correct spectral phase. The contrast can be further enhanced by computing the ratio between the images Fig. 5.6 b and c, which is presented in Fig. 5.6 d. To produce this image, pixels in which the signal is lower than 200 counts s^{-1} were discarded as they correspond to areas in which no nanoantenna was present, and they were thus dominated by dark counts in the APDs.

The results of Fig. 5.6 demonstrate that closed loop phase control of the TPA in pairs of plasmonic nanoantennas is possible. To emphasize the role of coherence, it must be noted that the algorithm acted purely on the spectral phase of the laser field, while the laser spectrum was kept constant. Therefore, during an optimization, the laser was always resonantly driving both the LSPRs of the two nanoantennas. Only in the coherent regime could the spectral phase of the laser field selectively excite one or the other system. This findings further support the hypothesis of: (i) the existence of a coherent regime in which the spectral phase of the laser field can influence the TPA process; (ii) the possibility of discriminating between different nanoantennas based on their LSPRs, which allows a tailored laser field to maximize their relative TPA.

5.3.3 Coherent two photon microscopy

One of the applications of multiphoton coherent control is the selective excitation of ensembles of different species of molecules and quantum dots [147, 160, 161, 177]. Based on the results of the previous section, the same concept can be applied to the selective imaging of nanoantennas, with single structure spatial resolution.

From Fig. 5.1, it can be noticed that the TPPL signal from nanoantennas with the same nominal length fluctuated due to fabrication imperfections. It is therefore important to establish if the coherent properties of the individual nanoantennas were also equally affected, or if the phases $\varphi(\omega)_{\max}$ and $\varphi(\omega)_{\min}$ generated reproducible contrast in different 120 and 90 nm pairs. The upper image in Fig. 5.7 shows a ratio image (obtained with the same procedure as for Fig. 5.6 d) of several different nanoantennas in a line pair. As can be seen, switching from $\varphi(\omega)_{\max}$ to $\varphi(\omega)_{\min}$ produced a similar effect in most of the 90-120 nm structures. In order to give a quantitative analysis, we calculated

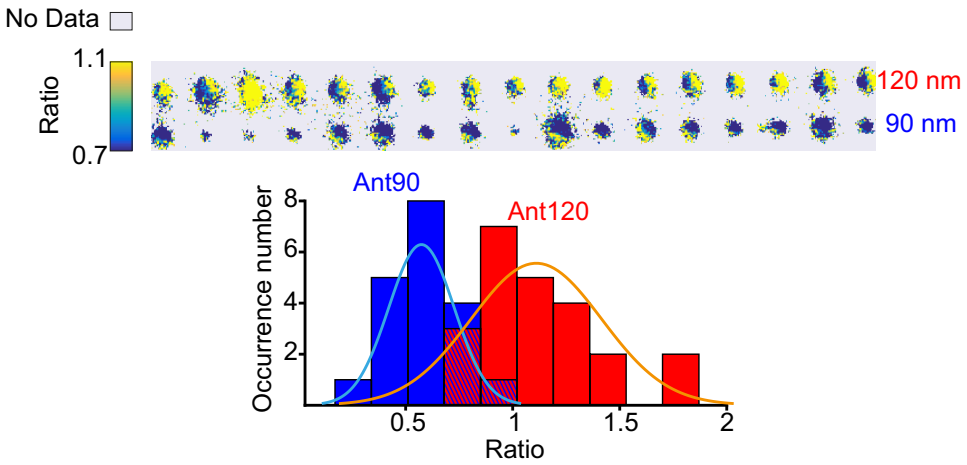

Fig. 5.7: The upper image is the ratio between the two-photon induced photoluminescence images obtained with $\varphi(\omega)_{\max}$ and $\varphi(\omega)_{\min}$ respectively. 120 nm nanoantennas are brighter when using $\varphi(\omega)_{\max}$, whereas 90 nm ones are brighter when excited with $\varphi(\omega)_{\min}$. The histogram on the bottom quantitatively analyses the ratio of the TPPL of all the nanoantennas with the two different phases. The cyan and orange curves superimposed on the histogram are fits to the data assuming a normal distribution. Note that in the histogram a full array of nanoantennas is considered for the statistics (23 pairs, as one can see from Fig. 5.1 a), whereas in the upper image a zoom on 17 pairs of nanoantennas is shown. Moreover, for some of the 90 nm nanoantennas the TPPL intensity emitted with $\varphi(\omega)_{\min}$ was so low that it is not taken into account in the histogram graph.

the ratios between the total TPPL intensities produced by each nanoantenna with the phases $\varphi(\omega)_{\max}$ and $\varphi(\omega)_{\min}$ respectively and reported them in the histogram of Fig. 5.7. From two-dimensional TPPL images the total intensity for each nanoantenna was calculated by summing up all the pixels in the corresponding diffraction limited spot. The histogram confirms the shift of the distribution of the ratios for the different species, which can be better visualized based on the fits to the data assuming a normal distribution function. It should be noted that a higher level of control could be obtained for the 90 nm nanoantennas. By changing the spectral phase from $\varphi(\omega)_{\min}$ to $\varphi(\omega)_{\max}$, the TPPL from the 120 nm nanoantennas increased by ~ 1.12 whereas that from 90 nm ones decreased by ~ 1.76, and the total contrast was about 2. Despite the inhomogeneity in the sample under study, the same contrast achieved in

the single pair optimization was maintained over many nanoantennas, which underlines that the LSPRs were only slightly affected by fabrication imperfections, in agreement with previous reports [119].

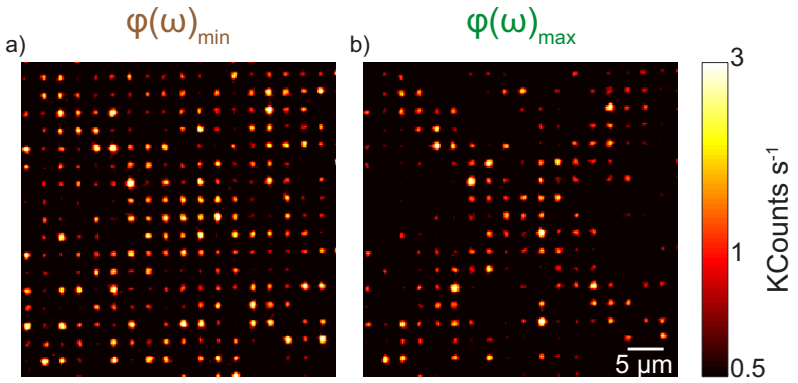

Fig. 5.8: Two-photon induced photoluminescence images of an array of mixed 120 nm and 90 nm nanoantennas using $\varphi(\omega)_{\min}$ (a) and $\varphi(\omega)_{\max}$ (b). $\varphi(\omega)_{\min}$ hides the message encoded in the array whereas $\varphi(\omega)_{\max}$ reveals the letter X.

To rule out improbable systematic errors in the image of Fig. 5.7, which could be due to the specific arrangement of the nanoantennas in which the 120 nm always appeared above the 90 nm ones, we designed, and fabricated, a different array where the two species of nanoantennas were mixed together. In this array, 120 nm nanoantennas were arranged such to form a X letter on a background of 90 nm ones. Fig. 5.8 shows TPPL images of such an array recorded with $\varphi(\omega)_{\max}$ and $\varphi(\omega)_{\min}$ respectively. The application of $\varphi(\omega)_{\max}$ by the SLM revealed the X, whereas $\varphi(\omega)_{\min}$ completely hid the message encoded in the array as all the nanoantennas emitted, within fabrication errors, comparable amounts of TPPL. Multiphoton coherent control can thus be used to extract sensitive microscopic information about different resonant species.

On the basis of Fig. 5.6, one could expect that the 90 nm nanoantennas should emit higher TPPL than the 120 nm when using $\varphi(\omega)_{\min}$, and therefore to see a negative X image in Fig. 5.7 a. However, the complete switch of the TPPL maximum did not occur for each nanoantenna pair in the sample. The values reported in the histogram of Fig. 5.7 are the ratios $I_A^{\max}/I_A^{\min}$ for different nanoantennas in the investigated array and thus do not contain the information of the relative TPPL intensity of the 120 nm and the 90 nm species.

The shift in the distribution should be interpreted as follows: 120 nm nanoantennas emitted higher TPPL when using $\varphi(\omega)_{\max}$; 90 nm ones emitted higher TPPL when using $\varphi(\omega)_{\min}$. This does not necessarily imply that the TPPL maximum switched form the 120 nm to the 90 nm nanoantennas by changing from $\varphi(\omega)_{\max}$ to $\varphi(\omega)_{\min}$. In the case of the pair shown in Fig. 5.6 this was indeed the case and such pair was used to better represent the experimental concept. In general however, in Fig. 5.8, the 120 nm nanoantennas always emitted more or the same TPPL with respect to the 90 nm species. Thus, even if the contrast of about 2 was maintained on average in all the pairs, complete switch of the TPPL maximum did not occur in the case of the sample of Fig. 5.8.

5.3.4 Interpretation of coherent control

This section analyzes the outcome of the coherent control experiment, starting from the discussion of Sec. 5.2. The excitation laser spectrum used, together with the spectral phases $\varphi(\omega)_{\max}$ and $\varphi(\omega)_{\min}$ obtained after maximization and minimization are shown in Fig. 5.9 a. The spectral phases were independently measured using the method developed in Chap. 2, i.e. performing MIIPS on SH NPs. In the same plot the blue and red dashed curves correspond to the LSPR absorption profiles for the 90 nm and 120 nm nanoantennas, as obtained from finite difference time domain (FDTD) simulations, which confirm that the two species were indeed resonant with different sides of the laser spectrum. These curves represent the intermediate states in the TPA process, i.e. the terms $A(\omega)$ in Eq. (5.2). From this plot it is apparent that the two spectral phases $\varphi(\omega)_{\max}$ and $\varphi(\omega)_{\min}$ have symmetric behaviors with respect to the positions of the LSPRs. Fig. 5.9 b gives a schematics of the level diagram and the TPA process in the two nanoantennas. The TPA involves different possible pathways, as already discussed for the SH process (Sec. 1.4.1). If the laser spectrum partially overlaps with a LSPR (as in the graph of Fig. 5.9 a), the absorption events that proceed through the LSPR are enhanced (solid arrows in the sketch) with respect to the ones that are not fully resonant with the LSPR (dashed arrows). This intuitive model captures the underlying coherent control process of the experiment described here.

To further understand the experimental results, Fig. 5.9 c and d show the time-frequency representation, or Wigner representations [178] for the two electric fields corresponding to the maximization and minimization case re-

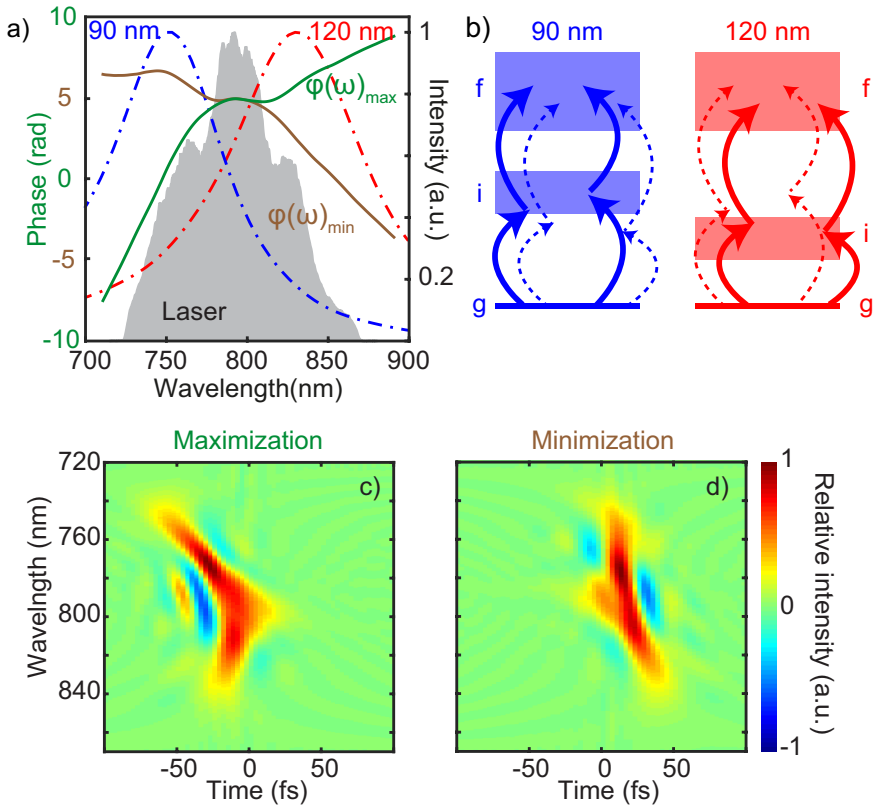

Fig. 5.9: a) Laser spectrum (shaded region), $\varphi(\omega)_{\max}$ (green curve) and $\varphi(\omega)_{\min}$ (brown curve) as measured by MIIPS. The red and blue dashed curves are the resonance response of the 90 nm and the 120 nm nanoantennas as obtained by simulations. b) Sketch of the level scheme and possible transition pathways for the TPA in the nanoantennas. g, i, f are the ground, intermediate and final states respectively. c,d) Time-frequency representation of the pulses corresponding to the maximization and minimization case respectively.

spectively. From such representation, it is possible to visualize how the different wavelength components of the electric field move in time. By summing on the time axis of Fig. 5.9 c and d, one obtains the spectrum of the laser field, whereas integration over the wavelength coordinate generates the time dependent envelope of the laser pulse. The information included in this representation however, is the same as that of the spectral phase and the laser spectrum of Fig. 5.9 a together.

In the spectral domain (vertical axis of the plots) one can see that in the maximization case (Fig. 5.9 c), the red part of the laser spectrum is only slightly distorted, as all the red wavelength components arrive simultaneously, while the blue part is chirped, as can be deduced from the time shift between different wavelength components for wavelengths $\lambda < 800\,\mathrm{nm}$. The opposite situation is true for the minimization pulse. The effect of coherent control in the experiment was thus to distort the pulse in the spectral region of the unwanted LSPR and make TPA through the desired plasmon resonance more favorable. In terms of the level diagram of Fig. 5.9 b, this spectral argument essentially means that, in the maximization case, constructive interference was induced among the most relevant absorption events for the 120 nm nanoantenna (represented by the red solid arrows). Destructive interference instead, occurred among the less important processes for the 120 nm nanoantenna (the dashed red arrows), which correspond to the most relevant ones for the 90 nm nanoantenna (blue solid arrows), leading to inefficient excitation of the 90 nm nanoantenna. This is consistent with our findings that $\varphi(\omega)_{\mathrm{max}}$ maximized the ratio I_{120}/I_{90} and $\varphi(\omega)_{\mathrm{min}}$ minimized it.

However, also the temporal characteristics of the pulses have to be taken into account. As explained previously, phase control can only be achieved in the limit of short pulses (within the coherent regime of Fig. 5.2), whereas for longer pulses the spectral phase of the laser field has no effect on the TPA process. Indeed, the pulses represented in Fig. 5.9 c and d are still very short, with a total duration of less than 50 fs and the phase distortions are not very large. Under these conditions the two laser pulses produced by the optimization experiment could coherently interact with the nanoantennas, actively controlling their relative TPA.

As a final check that the interpretation given throughout this chapter is consistent with the experimental results, it is possible to calculate the TPA probability in the two different nanoantennas under excitation with the spectral phases $\varphi(\omega)_{\mathrm{max}}$ and $\varphi(\omega)_{\mathrm{min}}$ by using Eq. (5.2), which describes the TPA in the limit of short laser pulses. For doing so we used the simulated curves for the LSPRs of the two nanoantennas shown in Fig. 5.9 a as the $A(\omega)$ terms in the equation. The calculated TPA probabilities were in good agreement with the experiment, yielding $I_{90}^{\mathrm{min}}/I_{90}^{\mathrm{max}} = 2.0$ for the 90 nm nanoantenna and $I_{120}^{\mathrm{max}}/I_{120}^{\mathrm{min}} = 1.3$ for the 120 nm one, with a total simulated contrast of ~ 2.6. Using Eq. (5.2) one therefore consistently finds that a higher level of control

can be obtained for the 90 nm nanoantenna than for the 120 nm and the total contrast is in good agreement with the experiment.

5.4 Conclusions

In summary, in this chapter I have addressed the two-photon absorption process in resonant gold nanoantennas. The results shown here suggest that TPA in these systems proceeds through a two-step process in which two successive single photon absorption events excite the system to its final state, in agreement with previous reports. For laser pulses shorter than the lifetime of the intermediate state (~ 350 fs in this case), the TPA dynamics can be divided into a coherent and an incoherent regime. In the former, which is only measurable for pulses shorter than 50 fs, the TPA is sensitive to the spectral phase of the laser pulse and coherent control becomes possible. For pulses longer than 50 fs instead, the fast decoherence associated to surface plasmons completely cancels the dependence of the TPA on the spectral phase of the incident field. In the second part of the chapter I have demonstrated the realization of a closed loop coherent control experiment capable of working in the coherent regime and of maximizing the ratio between the TPPL from two different nanoantennas solely by shaping the laser spectral phase. This is a conclusive demonstration of highly sensitive closed loop coherent control on the nanoscale.

Conclusion

Ultrafast nanophotonics deals with the study and control of light-matter interactions at the femtosecond and nanometer scales. Simultaneously accessing these regimes gives the opportunity to unveil the ultrafast dynamical processes, such as electronic coherence, energy transfer and vibrational motion, governing the evolution of individual nanoparticles immediately after interaction with photons. Controlling such evolution at will is the current challenge in ultrafast nanophotonics and requires control over both the design and fabrication of nanoparticles and the electric fields used to excite them.

In this thesis I have described our efforts towards the active control of light-matter interactions in different nanoparticles by using ultrashort laser pulses. The results I have presented can be divided into two categories: (i) the development ant test of experimental approaches capable of accessing the desired phenomena; (ii) the application of such schemes to the investigation and active control of coherent processes especially in plasmonic nanoantennas.

The practical realization of experiments that simultaneously achieve high spatial and temporal resolution is particularly challenging. Our experimental choice, not the only possible one, was to use ultrashort phase-controlled laser pulses in a high-resolution confocal microscope. By using non-resonant second harmonic nanoparticles I have shown that this approach is suitable to obtain full phase control of ultrashort pulses with sub-wavelength spatial resolution in the focus of the optical microscope. The subsequent demonstration of an effective closed loop optimization scheme capable of addressing even single quantum emitters at room temperature, is the second experimental advance presented in the thesis. These findings constitute essential and powerful tools for the control of light-matter interactions at the nanoscale.

In terms of new physical insights, the main results of the thesis were obtained by applying our experimental schemes to resonant plasmonic nanoantennas, whose unique properties make them very promising for nonlinear

and coherent studies. Throughout the thesis I have shown that new phenomena, rarely explored so far, become visible when exciting these systems with ultrashort phase-controlled pulses. Plasmonic nanoantennas are often viewed as tools to connect propagating and very localized optical fields. At the same time however, their nonlinear response to ultrashort pulses is interesting by itself. I have shown that different colors at the second harmonic wavelength can be produced by the nanoantennas depending on their specific resonance. This special property, combined with precise phase shaping, gives the possibility of mapping the localized surface plasmon resonances and at the same time can be applied to a novel multicolor second harmonic imaging technique. I have then demonstrated that the two-photon absorption process in resonant gold nanoantennas is intrinsically suitable for ultrafast coherent control. Very short pulses have the potential to access the fast decaying coherence of the surface plasmons and to actively control the relative excitation between different nanoantennas.

Ultrafast nanophotonics is a field in action. Several research groups are currently focusing on the investigation of ultrafast light-matter interaction at the nanoscale, with the ultimate objective of actively controlling them. In parallel, great advances in nanotechnology are continuously made all over the world on a daily basis. In this context, the results presented here are relevant in multiple ways. On the one hand a complete toolbox to investigate nanoobjects with ultrashort pulses and to perform highly sensitive coherent control experiment has been demonstrated. On the other hand plasmonic nanoantennas have been shown to be particularly suitable for nanoscale coherent control with applications in the field of multiphoton and selective imaging. New exciting routes might open in the field of nanophotonics led by the progress in nanotechnology and the growing ability of researchers to manipulate ultrafast nanoscale dynamics using light. This thesis has given a contribution to this fascinating field

Publications

Publications covered in this thesis:

- **Accanto N**, Nieder JB, Piatkowski L, Castro-Lopez M, Pastorelli F, Brinks D, & van Hulst NF. *Phase control of femtosecond pulses on the nanoscale using second harmonic nanoparticles.* Light Sci. Appl. 3, e143 (2014)
- **Accanto N**, Piatkowski L, Renger J, & van Hulst NF. *Capturing the optical phase response of nanoantennas by coherent second-harmonic microscopy.* Nano Lett. 14, 4078 (2014)
- **Accanto N**, Piatkowski L, Hancu IM, Renger J, & van Hulst NF. *Resonant plasmonic nanoparticles for multicolor second harmonic imaging.* Appl. Phys. Lett. 108, 083115 (2016)
- Piatkowski L, **Accanto N**, & van Hulst NF. *Ultrafast meets Ultrasmall: Controlling Nanoantennas and Molecules.* ACS Photon. Review (2016)
- **Accanto N**, de Roque P, Galvan-Sosa M, Christodoulou S, Moreels I, & van Hulst NF. *Rapid and robust optimal control of single quantum dots.* Submitted (2016)
- **Accanto N**, de Roque P, Galvan-Sosa M, Hancu IM & van Hulst NF. *Closed loop phase control of the coherent two-photon absorption in resonant optical nanoantennas.* In preparation (2016)

Other publications by the author:

- Piatkowski L, **Accanto N**, Christodoulou S, Calbris G, Moreels I, & van Hulst NF. *Time-resolved stimulated emission microscopy of individual quantum emitters.* In preparation (2016)
- Pastorelli F, **Accanto N**, Jorgensen M, van Hulst NF, & Krebs FC. *Thermal and non-linear optical characterizations for printed electronics, a view on morphology.* In preparation (2016)

Bibliography

[1] T. Brixner, F. G. de Abajo, J. Schneider, and W. Pfeiffer. 'Nanoscopic ultrafast space-time-resolved spectroscopy'. *Phys. Rev. Lett.*, **95**, 093901 (2005).

[2] J. M. Gunn, M. Ewald, and M. Dantus. 'Polarization and Phase Control of Remote Surface-Plasmon-Mediated Two-Photon-Induced Emission and Waveguiding'. *Nano Lett.*, **6**, 2804 (2006).

[3] T. Brixner, F. J. García de Abajo, C. Spindler, and W. Pfeiffer. 'Adaptive ultrafast nano-optics in a tight focus'. *Appl. Phys. B*, **84**, 89 (2006).

[4] M. Aeschlimann, M. Bauer, D. Bayer, T. Brixner, F. J. García de Abajo, W. Pfeiffer, M. Rohmer, C. Spindler, and F. Steeb. 'Adaptive subwavelength control of nano-optical fields'. *Nature*, **446**, 301 (2007).

[5] J.-S. Huang, D. V. Voronine, P. Tuchscherer, T. Brixner, and B. Hecht. 'Deterministic spatiotemporal control of optical fields in nanoantennas and plasmonic circuits'. *Phys. Rev. B*, **79**, 195441 (2009).

[6] J. M. Gunn, S. H. High, V. V. Lozovoy, and M. Dantus. 'Measurement and Control of Ultrashort Optical Pulse Propagation in Metal Nanoparticle-Covered Dielectric Surfaces'. *J. Phys. Chem. C*, **114**, 12375 (2010).

[7] M. Aeschlimann, T. Brixner, A. Fischer, C. Kramer, P. Melchior, W. Pfeiffer, C. Schneider, C. Strüber, P. Tuchscherer, and D. V. Voronine. 'Coherent Two-Dimensional Nanoscopy'. *Science*, **333**, 1723 (2011).

[8] T. Hanke, J. Cesar, V. Knittel, A. Trügler, U. Hohenester, A. Leitenstorfer, and R. Bratschitsch. 'Tailoring Spatiotemporal Light Confinement in Single Plasmonic Nanoantennas'. *Nano Lett.*, **12**, 992 (2012).

[9] S. Schmidt, B. Piglosiewicz, D. Sadiq, J. Shirdel, J. S. Lee, P. Vasa, N. Park, D.-S. Kim, and C. Lienau. 'Adiabatic Nanofocusing on Ultrasmooth

Single-Crystalline Gold Tapers Creates a 10-nm-Sized Light Source with Few-Cycle Time Resolution'. *ACS Nano*, **6**, 6040 (2012).

[10] J. Lee, S. M. Perdue, A. R. Perez, and V. A. Apkarian. 'Vibronic Motion with Joint Angstrom–Femtosecond Resolution Observed through Fano Progressions Recorded within One Molecule'. *ACS Nano*, **8**, 54 (2013).

[11] H. Okamoto, T. Narushima, Y. Nishiyama, and K. Imura. 'Local optical responses of plasmon resonances visualised by near-field optical imaging'. *Phys. Chem. Chem. Phys.*, **17**, 6192 (2015).

[12] A. Weigel, A. Sebesta, and P. Kukura. 'Shaped and Feedback-Controlled Excitation of Single Molecules in the Weak-Field Limit'. *J. Phys. Chem. Lett.*, **6**, 4032 (2015).

[13] R. Mittal, R. Glenn, I. Saytashev, V. V. Lozovoy, and M. Dantus. 'Femtosecond Nanoplasmonic Dephasing of Individual Silver Nanoparticles and Small Clusters'. *J. Phys. Chem. Lett.*, **6**, 1638 (2015).

[14] V. Kravtsov, R. Ulbricht, J. M. Atkin, and M. B. Raschke. 'Plasmonic nanofocused four-wave mixing for femtosecond near-field imaging'. *Nat. Nanotechnol.* (2016).

[15] E. M. H. P. van Dijk, J. Hernando, J.-J. García-López, M. Crego-Calama, D. N. Reinhoudt, L. Kuipers, M. F. García-Parajó, and N. F. van Hulst. 'Single-Molecule Pump-Probe Detection Resolves Ultrafast Pathways in Individual and Coupled Quantum Systems'. *Phys. Rev. Lett.*, **94**, 078302 (2005).

[16] D. Brinks, F. D. Stefani, F. Kulzer, R. Hildner, T. H. Taminiau, Y. Avlasevich, K. Müllen, and N. F. van Hulst. 'Visualizing and controlling vibrational wave packets of single molecules'. *Nature*, **465**, 905 (2010).

[17] R. Hildner, D. Brinks, and N. F. van Hulst. 'Femtosecond coherence and quantum control of single molecules at room temperature'. *Nat. Phys.*, **7**, 172 (2010).

[18] R. Hildner, D. Brinks, J. B. Nieder, R. J. Cogdell, and N. F. van Hulst. 'Quantum Coherent Energy Transfer over Varying Pathways in Single Light-Harvesting Complexes'. *Science*, **340**, 1448 (2013).

[19] D. Brinks, R. Hildner, E. M. H. P. van Dijk, F. D. Stefani, J. B. Nieder, J. Hernando, and N. F. van Hulst. 'Ultrafast dynamics of single molecules'. *Chem. Soc. Rev.*, **43**, 2476 (2014).

[20] M. Shapiro and P. Brumer. Principles of the Quantum Control of Molecular Processes. A John Wiley & Sons (2003).

[21] D. J. Tannor, R. Kosloff, and S. A. Rice. 'Coherent pulse sequence induced control of selectivity of reactions: Exact quantum mechanical calculations'. *J. Chem. Phys.*, **85**, 5805 (1986).

[22] D. J. Tannor and S. A. Rice. 'Control of selectivity of chemical reaction via control of wave packet evolution'. *J. Chem. Phys.*, **83**, 5013 (1985).

[23] P. Brumer and M. Shapiro. 'Coherence chemistry: controlling chemical reactions with lasers'. *Acc. Chem. Res.* (1989).

[24] Y. Silberberg. 'Quantum coherent control for nonlinear spectroscopy and microscopy'. *Annu. Rev. Phys. Chem*, **60**, 277 (2009).

[25] C. Brif, R. Chakrabarti, and H. Rabitz. 'Control of quantum phenomena: past, present and future'. *New J. Phys.*, **12**, 075008 (2010).

[26] M. Dantus and V. V. Lozovoy. 'Experimental Coherent Laser Control of Physicochemical Processes'. *Chem. Rev.*, **104**, 1813 (2004).

[27] P. Nuernberger, G. Vogt, T. Brixner, and G. Gerber. 'Femtosecond quantum control of molecular dynamics in the condensed phase'. *Phys. Chem. Chem. Phys.*, **9**, 2470 (2007).

[28] A. M. Weiner, D. E. Leaird, J. S. Patel, and J. R. Wullert. 'Programmable femtosecond pulse shaping by use of a multielement liquid-crystal phase modulator'. *Opt. Lett.*, **15**, 326 (1990).

[29] A. M. Weiner. 'Femtosecond pulse shaping using spatial light modulators'. *Rev. Sci. Instrum.*, **71**, 1929 (2000).

[30] A. M. Weiner, D. E. Leaird, J. S. Patel, and J. R. I. Wullert. 'Programmable shaping of femtosecond optical pulses by use of 128-element liquid crystal phase modulator'. *IEEE J. Quantum Electron.*, **28**, 908 (1992).

[31] D. H. Reitze, A. M. Weiner, and D. E. Leaird. 'Shaping of wide bandwidth 20 femtosecond optical pulses'. *Appl. Phys. Lett.*, **61**, 1260 (1992).

[32] D. Meshulach, D. Yelin, and Y. Silberberg. 'Adaptive ultrashort pulse compression and shaping'. *Opt. Commun.*, **138**, 345 (1997).

[33] T. Feurer, J. C. Vaughan, R. M. Koehl, and K. A. Nelson. 'Multidimensional control of femtosecond pulses by use of a programmable liquid-crystal matrix'. *Opt. Lett.*, **27**, 652 (2002).

[34] A. Monmayrant, S. Weber, and B. Chatel. 'A newcomer's guide to ultrashort pulse shaping and characterization'. *J. Phys. B: At. Mol. Opt. Phys.*, **43**, 103001 (2010).

[35] V. V. Lozovoy, I. Pastirk, and M. Dantus. 'Multiphoton intrapulse interference. IV. Ultrashort laser pulse spectral phase characterization and compensation'. *Opt. Lett.* (2004).

[36] V. V. Lozovoy and M. Dantus. 'Laser control of physicochemical processes; experiments and applications'. *Annu. Rep. Prog. Chem., Sect. C: Phys. Chem.*, **102**, 227 (2006).

[37] D. Brinks, M. Castro-Lopez, R. Hildner, and N. F. van Hulst. 'Plasmonic antennas as design elements for coherent ultrafast nanophotonics'. *Proc. Natl. Acad. Sci. U.S.A.*, **110**, 18386 (2013).

[38] M. Minsky. 'US Patent Number 3013467: Microscopy apparatus' (1961).

[39] J. D. Jackson. Classical Electrodynamics. John Wiley & Sons (2007).

[40] R. Trebino. Frequency-Resolved Optical Gating: The Measurement of Ultrashort Laser Pulses. Springer Science & Business Media, Boston, MA (2012).

[41] S. J. Orfanidis. Electromagnetic Waves and Antennas. Rutgers University (2008).

[42] P. Devi, V. V. Lozovoy, and M. Dantus. 'Measurement of group velocity dispersion of solvents using 2-cycle femtosecond pulses: Experiment and theory'. *AIP Advances*, **1**, 032166 (2011).

[43] Y. Coello, V. V. Lozovoy, T. C. Gunaratne, B. Xu, I. Borukhovich, C.-h. Tseng, T. Weinacht, and M. Dantus. 'Interference without an interferometer: a different approach to measuring, compressing, and shaping ultrashort laser pulses'. *J. Opt. Soc. Am B*, **25**, A140 (2008).

[44] U. Fuchs, U. Zeitner, and A. T. u. nnermann. 'Ultra-short pulse propagation in complex optical systems'. *Opt. Express*, **13**, 3852 (2005).

[45] Z. Bor. 'Distortion of Femtosecond Laser-Pulses in Lenses'. *Opt. Lett.*, **14**, 119 (1989).

[46] M. Kempe and W. Rudolph. 'Femtosecond pulses in the focal region of lenses'. *Phys. Rev. A*, **48**, 4721 (1993).

[47] P. Bowlan, U. Fuchs, R. Trebino, and U. D. Zeitner. 'Measuring the spatiotemporal electric field of tightly focused ultrashort pulses with submicron spatial resolution.' *Opt. Express*, **16**, 13663 (2008).

[48] M. M. Wefers and K. A. Nelson. 'Space-time profiles of shaped ultrafast optical waveforms'. *IEEE J. Quantum Electron.*, **32**, 161 (1996).

[49] X. Gu, S. Akturk, and R. Trebino. 'Spatial chirp in ultrafast optics'. *Opt. Commun.*, **242**, 599 (2004).

[50] D. Brinks, R. Hildner, F. D. Stefani, and N. F. van Hulst. 'Beating spatiotemporal coupling: implications for pulse shaping and coherent control experiments'. *Opt. Express*, **19**, 26486 (2011).

[51] D. J. McCabe, D. R. Austin, A. Tajalli, S. Weber, I. A. Walmsley, and B. Chatel. 'Space–time coupling of shaped ultrafast ultraviolet pulses from an acousto-optic programmable dispersive filter'. *J. Opt. Soc. Am. B*, **28**, 58 (2011).

[52] F. Frei, A. Galler, and T. Feurer. 'Space-time coupling in femtosecond pulse shaping and its effects on coherent control'. *J. Chem. Phys.*, **130**, 034302 (2009).

[53] B. J. Sussman, R. Lausten, and A. Stolow. 'Focusing of light following a 4- fpulse shaper: Considerations for quantum control'. *Phys. Rev. A*, **77**, 043416 (2008).

[54] R. Trebino. 'Measuring the seemingly immeasurable'. *Nat. Photon.*, **5**, 189 (2011).

[55] C. Iaconis and I. A. Walmsley. 'Spectral phase interferometry for direct electric-field reconstruction of ultrashort optical pulses'. *Opt. Lett.*, **23**, 792 (1998).

[56] T.-w. Wu, J. Tang, B. Hajj, and M. Cui. 'Phase resolved interferometric spectral modulation (PRISM) for ultrafast pulse measurement and compression'. *Opt. Express*, **19**, 12961 (2011).

[57] K. A. Walowicz, I. Pastirk, V. V. Lozovoy, and M. Dantus. 'Multiphoton Intrapulse Interference. 1. Control of Multiphoton Processes in Condensed Phases'. *J. Phys. Chem. A*, **106**, 9369 (2002).

[58] V. V. Lozovoy, I. Pastirk, K. A. Walowicz, and M. Dantus. 'Multiphoton intrapulse interference. II. Control of two- and three-photon laser induced fluorescence with shaped pulses'. *J. Chem. Phys.*, **118**, 3187 (2003).

[59] B. Xu, J. M. Gunn, J. M. Dela Cruz, V. V. Lozovoy, and M. Dantus. 'Quantitative investigation of the multiphoton intrapulse interference phase scan method for simultaneous phase measurement and compensation of femtosecond laser pulses'. *J. Opt. Soc. Am B*, **23**, 750 (2006).

[60] V. V. Lozovoy, B. Xu, Y. Coello, and M. Dantus. 'Direct measurement of spectral phase for ultrashort laser pulses'. *Opt. Express*, **16**, 592 (2008).

[61] P. Wnuk, L. L. Xuan, A. Slablab, C. e. d. Tard, S. Perruchas, T. Gacoin, J.-F. c. c. o. Roch, D. Chauvat, and C. Radzewicz. 'Coherent nonlinear emission from a single KTP nanoparticle with broadband femtosecond pulses'. *Opt. Express*, **17**, 4652 (2009).

[62] N. Sandeau, L. Le Xuan, D. Chauvat, C. Zhou, J. F. Roch, and S. Brasselet. 'Defocused imaging of second harmonic generation from a single nanocrystal'. *Opt. Express*, **15**, 16051 (2007).

[63] L. Le Xuan, C. Zhou, A. Slablab, D. Chauvat, C. Tard, S. Perruchas, T. Gacoin, P. Villeval, and J.-F. Roch. 'Photostable Second-Harmonic

Generation from a Single KTiOPO 4Nanocrystal for Nonlinear Microscopy'. *Small*, **4**, 1332 (2008).

[64] L. Bonacina, Y. Mugnier, F. Courvoisier, R. Le Dantec, J. Extermann, Y. Lambert, V. Boutou, C. Galez, and J. P. Wolf. 'Polar Fe(IO3)3 nanocrystals as local probes for nonlinear microscopy'. *Appl. Phys. B*, **87**, 399 (2007).

[65] J. Extermann, P. Béjot, L. Bonacina, Y. Mugnier, R. Le Dantec, T. Mazingue, C. Galez, and J. P. Wolf. 'An inexpensive nonlinear medium for intense ultrabroadband pulse characterization'. *Appl. Phys. B*, **97**, 537 (2009).

[66] R. Bäumner, L. Bonacina, J. Enderlein, J. Extermann, T. Fricke-Begemann, G. Marowsky, and J.-P. Wolf. 'Evanescent-field-induced second harmonic generation by noncentrosymmetric nanoparticles'. *Opt. Express*, **18**, 23218 (2010).

[67] D. Staedler, T. Magouroux, R. Hadji, C. Joulaud, J. Extermann, S. Schwung, S. Passemard, C. Kasparian, G. Clarke, M. Gerrmann, R. L. Dantec, Y. Mugnier, D. Rytz, D. Ciepielewski, C. Galez, S. Gerber-Lemaire, L. Juillerat-Jeanneret, L. Bonacina, and J.-P. Wolf. 'Harmonic Nanocrystals for Biolabeling: A Survey of Optical Properties and Biocompatibility'. *ACS Nano*, **6**, 2542 (2012).

[68] J. Extermann, L. Bonacina, F. Courvoisier, D. Kiselev, Y. Mugnier, R. Le Dantec, C. Galez, and J.-P. Wolf. 'Nano-FROG: Frequency resolved optical gating by a nanometric object'. *Opt. Express*, **16**, 10405 (2008).

[69] P. Pantazis, J. Maloney, D. Wu, and S. E. Fraser. 'Second harmonic generating (SHG) nanoprobes for in vivo imaging'. *Proc. Natl. Acad. Sci. U.S.A.*, **107**, 14535 (2010).

[70] A. Rogov, Y. Mugnier, and L. Bonacina. 'Harmonic nanoparticles: noncentrosymmetric metal oxides for nonlinear optics'. *Journal of Optics* (2015).

[71] F. Helmchen and W. Denk. 'Deep tissue two-photon microscopy'. *Nat Meth*, **2**, 932 (2005).

[72] M. Kauranen and A. V. Zayats. 'Nonlinear plasmonics'. *Nat. Photon.*, **6**, 737 (2012).

[73] G. Bachelier, J. Butet, I. Russier-Antoine, C. Jonin, E. Benichou, and P. F. Brevet. 'Origin of optical second-harmonic generation in spherical gold nanoparticles: Local surface and nonlocal bulk contributions'. *Phys. Rev. B*, **82**, 235403 (2010).

[74] A. Benedetti, M. Centini, M. Bertolotti, and C. Sibilia. 'Second harmonic generation from 3D nanoantennas: on the surface and bulk contributions by far-field pattern analysis'. *Opt. Express*, **19**, 26752 (2011).

[75] J. Butet, J. Duboisset, G. Bachelier, I. Russier-Antoine, E. Benichou, C. Jonin, and P.-F. Brevet. 'Optical Second Harmonic Generation of Single Metallic Nanoparticles Embedded in a Homogeneous Medium'. *Nano Lett.*, **10**, 1717 (2010).

[76] A. Slablab, L. Le Xuan, M. Zielinski, Y. de Wilde, V. Jacques, D. Chauvat, and J. F. Roch. 'Second-harmonic generation from coupled plasmon modes in a single dimer of gold nanospheres'. *Opt. Express*, **20**, 220 (2012).

[77] B. Metzger, L. Gui, J. Fuchs, D. Floess, and M. Hentschel. 'Strong enhancement of second harmonic emission by plasmonic resonances at the second harmonic wavelength'. *Nano . . .*, **15**, 3917 (2015).

[78] K. Thyagarajan, S. Rivier, A. Lovera, and O. J. Martin. 'Enhanced second-harmonic generation from double resonant plasmonic antennae'. *Opt. Express*, **20**, 12860 (2012).

[79] H. Aouani, M. Navarro-Cia, M. Rahmani, T. P. H. Sidiropoulos, M. Hong, R. F. Oulton, and S. A. Maier. 'Multiresonant Broadband Optical Antennas As Efficient Tunable Nanosources of Second Harmonic Light'. *Nano Lett.*, **12**, 4997 (2012).

[80] J. Butet, I. Russier-Antoine, C. Jonin, N. Lascoux, E. Benichou, and P.-F. Brevet. 'Sensing with Multipolar Second Harmonic Generation from Spherical Metallic Nanoparticles'. *Nano Lett.*, **12**, 1697 (2012).

[81] E. Hutter and D. Maysinger. 'Gold nanoparticles and quantum dots for bioimaging'. *Microscopy research and technique*, **74**, 592 (2011).

[82] H. Li, Z. Zhang, Q. Xu, K. Shi, Y. Jia, B. Zhang, Y. Xu, and Z. Liu. 'Characterizing ultrashort optical pulses using second-order nonlinear nanoprobes'. *Appl. Phys. Lett.*, **97**, 261108 (2010).

[83] L. Novotny and N. van Hulst. 'Antennas for light'. *Nat. Photon.*, **5**, 83 (2011).

[84] S. A. Maier. Plasmonics: Fundamentals and Applications. Springer Science & Business Media (2007).

[85] D. Pestov, V. V. Lozovoy, and M. Dantus. 'Multiple Independent Comb Shaping (MICS): phase-only generation of optical pulse sequences'. *Opt. Express*, **17**, 14351 (2009).

[86] D. Meshulach and Y. Silberberg. 'Coherent quantum control of two-photon transitions by a femtosecond laser pulse'. *Nature* (1998).

[87] S. Zhang, H. Zhang, T. Jia, Z. Wang, and Z. Sun. 'Coherent control of two-photon transitions in a two-level system with broadband absorption'. *Phys. Rev. A*, **80**, 043402 (2009).

[88] S. Zhang, C. Lu, T. Jia, J. Qiu, and Z. Sun. 'Coherent phase control of resonance-mediated two-photon absorption in rare-earth ions'. *Appl. Phys. Lett.*, **103**, 194104 (2013).

[89] P. Biagioni, M. Celebrano, M. Savoini, G. Grancini, D. Brida, S. Mátéfi-Tempfli, M. Mátéfi-Tempfli, L. Duò, B. Hecht, G. Cerullo, and M. Finazzi. 'Dependence of the two-photon photoluminescence yield of gold nanostructures on the laser pulse duration'. *Phys. Rev. B*, **80**, 045411 (2009).

[90] H.-D. Deng, G.-C. Li, Q.-F. Dai, M. Ouyang, S. Lan, V. A. Trofimov, and T. M. Lysak. 'Size dependent competition between second harmonic generation and two-photon luminescence observed in gold nanoparticles'. *Nanotechnology*, **24**, 075201 (2013).

[91] X.-F. Jiang, Y. Pan, C. Jiang, T. Zhao, P. Yuan, T. Venkatesan, and Q.-H. Xu. 'Excitation Nature of Two-Photon Photoluminescence of Gold Nanorods and Coupled Gold Nanoparticles Studied by Two-Pulse Emission Modulation Spectroscopy'. *J. Phys. Chem. Lett.*, **4**, 1634 (2013).

[92] M. Castro-Lopez, D. Brinks, R. Sapienza, and N. F. van Hulst. 'Aluminum for Nonlinear Plasmonics: Resonance-Driven Polarized Luminescence of Al, Ag, and Au Nanoantennas'. *Nano Lett.*, **11**, 4674 (2011).

[93] P. Ghenuche, S. Cherukulappurath, T. H. Taminiau, N. F. van Hulst, and R. Quidant. 'Spectroscopic Mode Mapping of Resonant Plasmon Nanoantennas'. *Phys. Rev. Lett.*, **101**, 116805 (2008).

[94] K. L. Kelly, E. Coronado, L. L. Zhao, and G. C. Schatz. 'The Optical Properties of Metal Nanoparticles: The Influence of Size, Shape, and Dielectric Environment'. *J. Phys. Chem. B*, **107**, 668 (2003).

[95] P. Biagioni, J.-S. Huang, and B. Hecht. 'Nanoantennas for visible and infrared radiation'. *Rep. Prog. Phys.*, **75**, 024402 (2012).

[96] P. Bharadwaj, B. Deutsch, and L. Novotny. 'Optical Antennas'. *Adv. Opt. Photonics*, **1**, 438 (2009).

[97] T. H. Taminiau, F. D. Stefani, F. B. Segerink, and N. F. van Hulst. 'Optical antennas direct single-molecule emission'. *Nat. Photon.*, **2**, 234 (2008).

[98] P. Mühlschlegel, H. J. Eisler, O. J. F. Martin, B. Hecht, and D. W. Pohl. 'Resonant Optical Antennas'. *Science*, **308**, 1607 (2005).

[99] K. A. Willets and R. P. Van Duyne. 'Localized surface plasmon resonance spectroscopy and sensing'. *Annu. Rev. Phys. Chem* (2007).

[100] T. H. Taminiau, F. D. Stefani, and N. F. van Hulst. 'Optical Nanorod Antennas Modeled as Cavities for Dipolar Emitters: Evolution of Sub- and Super-Radiant Modes'. *Nano Lett.*, **11**, 1020 (2011).

[101] J. N. Farahani, H.-J. Eisler, D. W. Pohl, M. Pavius, P. Flückiger, P. Gasser, and B. Hecht. 'Bow-tie optical antenna probes for single-emitter scanning near-field optical microscopy'. *Nanotechnology*, **18**, 125506 (2007).

[102] A. Singh, G. Calbris, and N. F. van Hulst. 'Vectorial Nanoscale Mapping of Optical Antenna Fields by Single Molecule Dipoles'. *Nano Lett.*, **14**, 4715 (2014).

[103] L. Neumann, Y. Pang, A. Houyou, M. L. Juan, R. Gordon, and N. F. van Hulst. 'Extraordinary Optical Transmission Brightens Near-Field Fiber Probe'. *Nano Lett.*, **11**, 355 (2011).

[104] A. G. Curto, G. Volpe, T. H. Taminiau, M. P. Kreuzer, R. Quidant, and N. F. van Hulst. 'Unidirectional Emission of a Quantum Dot Coupled to a Nanoantenna'. *Science*, **329**, 930 (2010).

[105] I. M. Hancu, A. G. Curto, M. Castro-Lopez, M. Kuttge, and N. F. van Hulst. 'Multipolar Interference for Directed Light Emission'. *Nano Lett.*, **14**, 166 (2014).

[106] G. Zengin, M. Wersäll, S. Nilsson, T. J. Antosiewicz, M. Käll, and T. Shegai. 'Realizing Strong Light-Matter Interactions between Single-Nanoparticle Plasmons and Molecular Excitons at Ambient Conditions'. *Phys. Rev. Lett.*, **114**, 157401 (2015).

[107] A. Kinkhabwala, Z. Yu, S. Fan, Y. Avlasevich, K. Müllen, and W. E. Moerner. 'Large single-molecule fluorescence enhancements produced by a bowtie nanoantenna'. *Nat. Photon.*, **3**, 654 (2009).

[108] E. Wientjes, J. Renger, A. G. Curto, R. Cogdell, and N. F. van Hulst. 'Strong antenna-enhanced fluorescence of a single light-harvesting complex shows photon antibunching'. *Nat. Commun.*, **5** (2014).

[109] F. Pastorelli, S. Bidault, J. Martorell, and N. Bonod. 'Self-Assembled Plasmonic Oligomers for Organic Photovoltaics'. *Adv. Opt. Mater.* (2013).

[110] J. N. Anker, W. P. Hall, O. Lyandres, N. C. Shah, J. Zhao, and R. P. Van Duyne. 'Biosensing with plasmonic nanosensors'. *Nat. Mater.*, **7**, 442 (2008).

[111] S. S. Aćimović, M. A. Ortega, V. Sanz, J. Berthelot, J. L. Garcia-Cordero, J. Renger, S. J. Maerkl, M. P. Kreuzer, and R. Quidant. 'LSPR Chip for Parallel, Rapid, and Sensitive Detection of Cancer Markers in Serum'. *Nano Lett.*, **14**, 2636 (2014).

[112] K. M. Mayer and J. H. Hafner. 'Localized Surface Plasmon Resonance Sensors'. *Chem. Rev.*, **111**, 3828 (2011).

[113] P. Zijlstra, P. M. R. Paulo, and M. Orrit. 'Optical detection of single non-absorbing molecules using the surface plasmon resonance of a gold nanorod'. *Nat. Nanotechnol.*, **7**, 379 (2012).

[114] T. Schumacher, K. Kratzer, D. Molnar, M. Hentschel, H. Giessen, and M. Lippitz. 'Nanoantenna-enhanced ultrafast nonlinear spectroscopy of a single gold nanoparticle'. *Nat. Commun.*, **2**, 333 (2011).

[115] M. I. Stockman. 'Ultrafast nanoplasmonics under coherent control'. *New J. Phys.*, **10**, 025031 (2008).

[116] K. Imaeda and K. Imura. 'Optical control of plasmonic fields by phase-modulated pulse excitations'. *Opt. Express*, **21**, 27481 (2013).

[117] A. Anderson, K. S. Deryckx, X. G. Xu, G. Steinmeyer, and M. B. Raschke. 'Few-Femtosecond Plasmon Dephasing of a Single Metallic Nanostructure from Optical Response Function Reconstruction by Interferometric Frequency Resolved Optical Gating'. *Nano Lett.*, **10**, 2519 (2010).

[118] Y. Nishiyama, K. Imura, and H. Okamoto. 'Observation of Plasmon Wave Packet Motions via Femtosecond Time-Resolved Near-Field Imaging Techniques'. *Nano Lett.*, **15**, 7657 (2015).

[119] Y. Nishiyama, K. Imaeda, K. Imura, and H. Okamoto. 'Plasmon Dephasing in Single Gold Nanorods Observed By Ultrafast Time-Resolved Near-Field Optical Microscopy'. *J. Phys. Chem. C*, **119**, 16215 (2015).

[120] Q. Sun, K. Ueno, H. Yu, A. Kubo, Y. Matsuo, and H. Misawa. 'Direct imaging of the near field and dynamics of surface plasmon resonance on gold nanostructures using photoemission electron microscopy'. *Light Sci. Appl.*, **2**, e118 (2013).

[121] E. Mårsell, A. Losquin, R. Svärd, M. Miranda, C. Guo, A. Harth, E. Lorek, J. Mauritsson, C. L. Arnold, H. Xu, A. L'Huillier, and A. Mikkelsen. 'Nanoscale Imaging of Local Few-Femtosecond Near-Field Dynamics within a Single Plasmonic Nanoantenna'. *Nano Lett.*, **15**, 6601 (2015).

[122] L. Novotny. 'Effective Wavelength Scaling for Optical Antennas'. *Phys. Rev. Lett.*, **98**, 266802 (2007).

[123] A. A. Maradudin, J. R. Sambles, and W. L. Barnes. Modern Plasmonics. Elsevier (2014).

[124] P. M. de Roque, J. Renger, and Niek F van Hulst. 'Bottlenecked-nano antennas enhance bulk contributions to second harmonic generation' (Submitted).

[125] H. Kim, C. M. Gilmore, A. Piqué, J. S. Horwitz, H. Mattoussi, H. Murata, Z. H. Kafafi, and D. B. Chrisey. 'Electrical, optical, and structural properties of indium–tin–oxide thin films for organic light-emitting devices'. *J. Appl. Phys.*, **86**, 6451 (1999).

[126] W. C. W. Chan, D. J. Maxwell, X. Gao, R. E. Bailey, M. Han, and S. Nie. 'Luminescent quantum dots for multiplexed biological detection and imaging'. *Curr. Opin. Biotechnol.*, **13**, 40 (2002).

[127] B. A. Kairdolf, A. M. Smith, T. H. Stokes, M. D. Wang, A. N. Young, and S. Nie. 'Semiconductor Quantum Dots for Bioimaging and Biodiagnostic Applications'. *Annu. Rev. Anal. Chem.*, **6**, 143 (2013).

[128] H. Rabitz, R. de Vivie-Riedle, M. Motzkus, and K. Kompa. 'Whither the Future of Controlling Quantum Phenomena?' *Science*, **288**, 824 (2000).

[129] V. V. Lozovoy and M. Dantus. 'Systematic Control of Nonlinear Optical Processes Using Optimally Shaped Femtosecond Pulses'. *ChemPhysChem*, **6**, 1970 (2005).

[130] R. S. Judson and H. Rabitz. 'Teaching Lasers to Control Molecules'. *Phys. Rev. Lett.*, **68**, 1500 (1992).

[131] P. Brumer and M. Shapiro. 'Control of unimolecular reactions using coherent light'. *Chem. Phys. Lett.*, **126**, 541 (1986).

[132] C. Chen, Y.-Y. Yin, and D. S. Elliott. 'Interference between optical transitions'. *Phys. Rev. Lett.*, **64**, 507 (1990).

[133] T. Baumert, M. Grosser, R. Thalweiser, and G. Gerber. 'Femtosecond time-resolved molecular multiphoton ionization: The Na2system'. *Phys. Rev. Lett.*, **67**, 3753 (1991).

[134] T. Baumert, B. Buehler, M. Grosser, R. Thalweiser, V. Weiss, E. Wiedenmann, and G. Gerber. 'Femtosecond time-resolved wave packet motion in molecular multiphoton ionization and fragmentation'. *J. Phys. Chem.*, **95**, 8103 (1991).

[135] E. D. Potter, J. L. Herek, S. Pedersen, Q. Liu, and A. H. Zewail. 'Femtosecond laser control of a chemical reaction'. *Nature*, **355**, 66 (1992).

[136] K. Bergmann, H. Theuer, and B. W. Shore. 'Coherent population transfer among quantum states of atoms and molecules'. *Rev. Mod. Phys.*, **70**, 1003 (1998).

[137] J. S. Melinger, S. R. Gandhi, A. Hariharan, J. X. Tull, and W. S. Warren. 'Generation of narrowband inversion with broadband laser pulses'. *Phys. Rev. Lett.*, **68**, 2000 (1992).

[138] B. Broers, H. B. van Linden van den Heuvell, and L. D. Noordam. 'Efficient population transfer in a three-level ladder system by frequency-swept ultrashort laser pulses'. *Phys. Rev. Lett.*, **69**, 2062 (1992).

[139] K. Ohmori. 'Wave-Packet and Coherent Control Dynamics'. *Annu. Rev. Phys. Chem*, **60**, 487 (2009).

[140] A. P. Peirce, M. A. Dahleh, and H. Rabitz. 'Optimal-Control of Quantum-Mechanical Systems - Existence, Numerical Approximation, and Applications'. *Phys. Rev. A*, **37**, 4950 (1988).

[141] H. A. Rabitz, M. M. Hsieh, and C. M. Rosenthal. 'Quantum optimally controlled transition landscapes'. *Science*, **303**, 1998 (2004).

[142] C. J. Bardeen, V. V. Yakovlev, K. R. Wilson, S. D. Carpenter, P. M. Weber, and W. S. Warren. 'Feedback quantum control of molecular electronic population transfer'. *Chem. Phys. Lett.*, **280**, 151 (1997).

[143] N. H. Bonadeo, J. Erland, D. Gammon, D. Park, D. S. Katzer, and D. G. Steel. 'Coherent Optical Control of the Quantum State of a Single Quantum Dot'. *Science*, **282**, 1473 (1998).

[144] J. L. Herek, W. Wohlleben, R. J. Cogdell, D. Zeidler, and M. Motzkus. 'Quantum control of energy flow in light harvesting'. *Nature*, **417**, 533 (2002).

[145] A. Assion. 'Control of Chemical Reactions by Feedback-Optimized Phase-Shaped Femtosecond Laser Pulses'. *Science*, **282**, 919 (1998).

[146] N. Dudovich, D. Oron, and Y. Silberberg. 'Single-pulse coherently controlled nonlinear Raman spectroscopy and microscopy'. *Nature*, **418**, 512 (2002).

[147] T. Brixner, N. H. Damrauer, P. Niklaus, and G. Gerber. 'Photoselective adaptive femtosecond quantum control in the liquid phase'. *Nature*, **414**, 57 (2001).

[148] D. G. Kuroda, C. P. Singh, Z. Peng, and V. D. Kleiman. 'Mapping Excited-State Dynamics by Coherent Control of a Dendrimer's Photoemission Efficiency'. *Science*, **326**, 263 (2009).

[149] L. Mandel and E. Wolf. Optical Coherence and Quantum Optics. Cambridge University Press (1995).

[150] W. van Sark, P. Frederix, A. A. Bol, H. C. Gerritsen, and A. Meijerink. 'Blueing, bleaching, and blinking of single CdSe/ZnS quantum dots'. *ChemPhysChem*, **3**, 871 (2002).

[151] M. Galvan-Sosa, J. Portilla, J. Hernandez-Rueda, J. Siegel, L. Moreno, A. R. de la Cruz, and J. Solis. 'Optimization of ultra-fast interactions using laser pulse temporal shaping controlled by a deterministic algorithm'. *Appl. Phys. A*, **114**, 477 (2014).

[152] J. M. Dela Cruz, I. Pastirk, M. Comstock, and M. Dantus. 'Multiphoton Intrapulse Interference 8. Coherent control through scattering tissue'. *Opt. Express*, **12**, 4144 (2004).

[153] D. Meshulach and Y. Silberberg. 'Coherent quantum control of multiphoton transitions by shaped ultrashort optical pulses'. *Phys. Rev. A*, **60**, 1287 (1999).

[154] D. Yelin, D. Meshulach, and Y. Silberberg. 'Adaptive femtosecond pulse compression'. *Opt. Lett.*, **22**, 1793 (1997).

[155] O. Katz, E. Small, Y. Bromberg, and Y. Silberberg. 'Focusing and compression of ultrashort pulses through scattering media'. *Nat. Photon.*, **5**, 372 (2011).

[156] S. Zhang, H. Zhang, T. Jia, Z. Wang, and Z. Sun. 'Coherent enhancement of resonance-mediated multiphoton absorption'. *J. Phys. B: At. Mol. Opt. Phys.*, **43**, 245502 (2010).

[157] S. Zhang, Z. Sun, X. Zhang, Y. Xu, Z. Wang, Z. Xu, and R. Li. 'Optimal feedback control of two-photon fluorescence in Coumarin 515 based on genetic algorithm'. *Chem. Phys. Lett.*, **415**, 346 (2005).

[158] S. Zhang, S. Xu, J. Ding, C. Lu, T. Jia, and J. Qiu. 'Single and two-photon fluorescence control of Er3+ ions by phase-shaped femtosecond laser pulse'. *Appl. Phys. Lett.* (2014).

[159] T. Baumert, T. Brixner, V. Seyfried, M. Strehle, and G. Gerber. 'Femtosecond pulse shaping by an evolutionary algorithm with feedback'. *Appl. Phys. B*, **65**, 779 (1997).

[160] M. Ruge, R. Wilcken, M. Wollenhaupt, A. Horn, and T. Baumert. 'Coherent Control of Colloidal Semiconductor Nanocrystals'. *J. Phys. Chem. C*, **117**, 11780 (2013).

[161] I. Pastirk, J. Dela Cruz, K. Walowicz, V. Lozovoy, and M. Dantus. 'Selective two-photon microscopy with shaped femtosecond pulses'. *Opt. Express*, **11**, 1695 (2003).

[162] S. Christodoulou, F. Rajadell, A. Casu, G. Vaccaro, J. Q. Grim, A. Genovese, L. Manna, J. I. Climente, F. Meinardi, G. Rainò, T. Stöferle, R. F. Mahrt, J. Planelles, S. Brovelli, and I. Moreels. 'Band structure engineering via piezoelectric fields in strained anisotropic CdSe/CdS nanocrystals'. *Nat. Commun.*, **6**, 7905 (2015).

[163] M. Allione, A. Ballester, H. Li, A. Comin, J. L. Movilla, J. I. Climente, L. Manna, and I. Moreels. 'Two-Photon-Induced Blue Shift of Core and Shell Optical Transitions in Colloidal CdSe/CdS Quasi-Type II Quantum Rods'. *ACS Nano*, **7**, 2443 (2013).

[164] G. Xing, Y. Liao, X. Wu, S. Chakrabortty, X. Liu, E. K. L. Yeow, Y. Chan, and T. C. Sum. 'Ultralow-Threshold Two-Photon Pumped Amplified Spontaneous Emission and Lasing from Seeded CdSe/CdS Nanorod Heterostructures'. *ACS Nano*, **6**, 10835 (2012).

[165] X. Li, J. van Embden, J. W. Chon, and M. Gu. 'Enhanced two-photon absorption of CdS nanocrystal rods'. *Appl. Phys. Lett.*, **94**, 103117 (2009).

[166] B. Mahler, P. Spinicelli, S. Buil, X. Quelin, and J. P. Hermier. 'Towards non-blinking colloidal quantum dots'. *Nat. Mater.* (2008).

[167] Y. S. Park, A. V. Malko, J. Vela, Y. Chen, and Y. Ghosh. 'Near-unity quantum yields of biexciton emission from CdSe/CdS nanocrystals measured using single-particle spectroscopy'. *Phys. Rev. Lett.*, **106**, 187401 (2011).

[168] G. Nair, J. Zhao, and M. G. Bawendi. 'Biexciton Quantum Yield of Single Semiconductor Nanocrystals from Photon Statistics'. *Nano Lett.*, **11**, 1136 (2011).

[169] M. Stockman, S. Faleev, and D. Bergman. 'Coherent Control of Femtosecond Energy Localization in Nanosystems'. *Phys. Rev. Lett.*, **88**, 067402 (2002).

[170] M. Aeschlimann, M. Bauer, D. Bayer, T. Brixner, S. Cunovic, F. Dimler, A. Fischer, W. Pfeiffer, M. Rohmer, C. Schneider, F. Steeb, C. Struber, and D. V. Voronine. 'Spatiotemporal control of nanooptical excitations'. *Proc. Natl. Acad. Sci. U.S.A.*, **107**, 5329 (2010).

[171] K. Imura, T. Nagahara, and H. Okamoto. 'Near-Field Two-Photon-Induced Photoluminescence from Single Gold Nanorods and Imaging of Plasmon Modes'. *J. Phys. Chem. B*, **109**, 13214 (2005).

[172] M. R. Beversluis, A. Bouhelier, and L. Novotny. 'Continuum generation from single gold nanostructures through near-field mediated intraband transitions'. *Phys. Rev. B*, **68**, 115433 (2003).

[173] V. Knittel, M. P. Fischer, T. de Roo, S. Mecking, A. Leitenstorfer, and D. Brida. 'Nonlinear Photoluminescence Spectrum of Single Gold Nanostructures'. *ACS Nano*, **9**, 894 (2015).

[174] P. Biagioni, D. Brida, J.-S. Huang, J. Kern, L. Duò, B. Hecht, M. Finazzi, and G. Cerullo. 'Dynamics of Four-Photon Photoluminescence in Gold Nanoantennas'. *Nano Lett.*, **12**, 2941 (2012).

[175] N. Dudovich, B. Dayan, S. M. G. Faeder, and Y. Silberberg. 'Transform-limited pulses are not optimal for resonant multiphoton transitions'. *Phys. Rev. Lett.*, **86**, 47 (2001).

[176] B. Chatel, J. Degert, and B. Girard. 'Role of quadratic and cubic spectral phases in ladder climbing with ultrashort pulses'. *Phys. Rev. A*, **70**, 053414 (2004).

[177] J. P. Ogilvie, D. Débarre, X. Solinas, J.-L. Martin, E. Beaurepaire, and M. Joffre. 'Use of coherent control for selective two-photon fluorescence microscopy in live organisms'. *Opt. Express*, **14**, 759 (2006).

[178] J. Paye. 'The chronocyclic representation of ultrashort light pulses'. *IEEE J. Quant. Electron*, **28**, 2262 (1992).